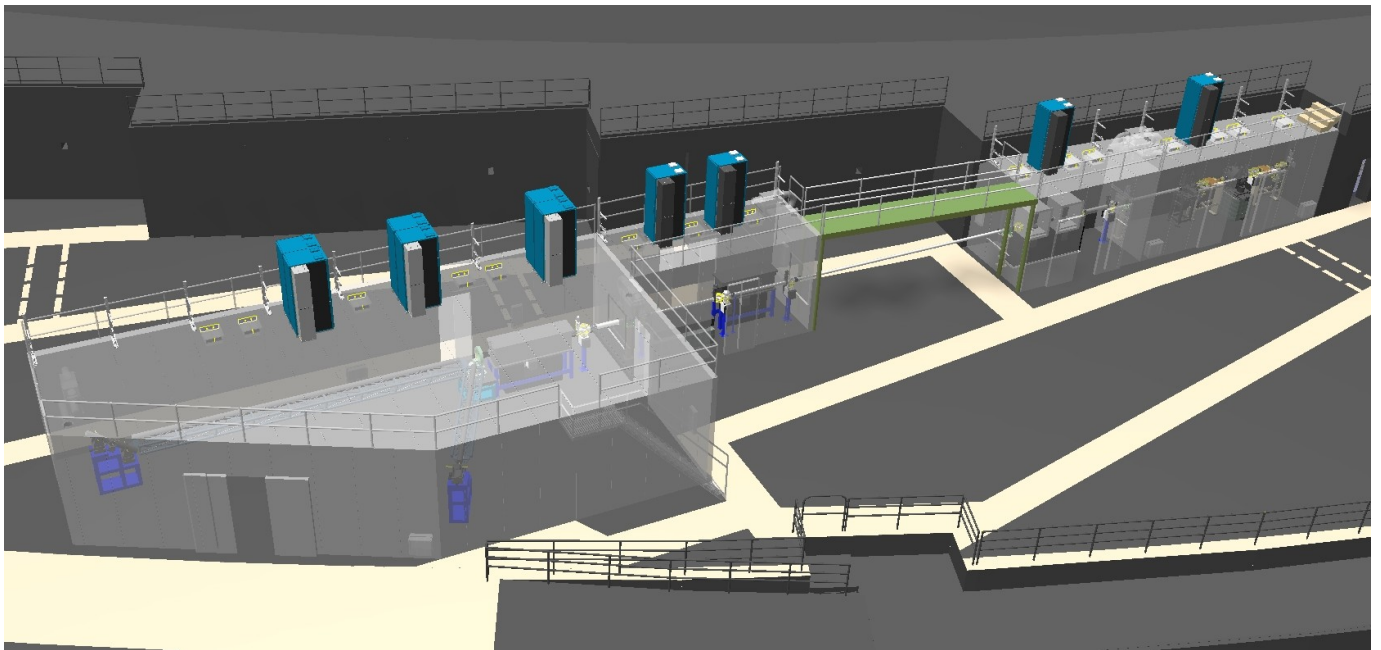


NSLS-II Project

PRELIMINARY DESIGN REPORT for the INELASTIC X-RAY SCATTERING BEAMLINE at NSLS-II



First Draft September 2010

Intentionally blank.

Approvals and Reviewers

Compiled by

Yong Cai, IXS Group Leader

Signature

Date

Approved

Qun Shen, XFD Director, NSLS-II

Reviewers

Dr Clement Burns, BAT Spokesperson, signing on behalf of the BAT

Andy Broadbent, Beamlines Manager

Nicholas Gmür, ESH Coordinator, NSLS-II

Sushil Sharma, Mechanical Engineering Group Leader, NSLS-II

_____	_____
_____	_____
_____	_____
_____	_____
_____	_____
_____	_____
_____	_____

Document Updates

The Preliminary Design Report for the Inelastic X-Ray Scattering (IXS) beamline at NSLS-II is a controlled document, revised under change control.

Version No.	Date	Changes made
A	9/15/2010	Initial draft
	10/10/2010	Submitted to BAT

Intentionally blank.

Contents

1	INTRODUCTION	1
1.1	SCIENTIFIC OBJECTIVE.....	1
1.2	BEAMLINE ADVISORY TEAM (BAT).....	2
1.3	THE IXS PROJECT TEAM.....	3
1.4	ACKNOWLEDGEMENT	3
2	INSERTION DEVICE	4
2.1	BASELINE DEVICE.....	5
2.2	UPGRADE OPTIONS	5
3	FRONT END	7
3.1	GENERAL LAYOUT	7
3.2	BRIEF DESCRIPTION OF MAJOR COMPONENTS AND SPECIFICATIONS.....	7
3.3	SPECIAL REQUIREMENTS (BERYLLIUM COMPOUND REFRACTIVE LENSES).....	10
3.4	RAY TRACINGS	11
3.5	FINITE ELEMENT ANALYSIS.....	11
4	BEAMLINE DESIGN	13
4.1	OVERVIEW	13
4.2	HIGH HEAT LOAD OPTICS.....	15
4.3	HIGH RESOLUTION OPTICS.....	24
4.4	FOCUSING OPTICS.....	31
4.5	BEAM TRANSPORT.....	35
4.6	OTHER MAJOR COMPONENTS	37
5	END STATION DESIGN	39
5.1	OVERVIEW	39
5.2	SAMPLE ENVIRONMENTS.....	39
5.3	COLLIMATING OPTICS	44
5.4	ANALYZER OPTICS.....	46
5.5	DETECTORS	47
6	INFRASTRUCTURE FOR BEAMLINE AND USER SUPPORT	48
6.1	HUTCHES.....	48
6.2	ENVIRONMENTAL REQUIREMENTS	50
6.3	SURVEYING REQUIREMENTS	50
6.4	CONTROLS AND DATA ACQUISITION REQUIREMENTS	50
6.5	UTILITIES REQUIREMENTS.....	51
6.6	USER SPACE.....	52
7	SPECIAL BEAMLINE REQUIREMENTS	54
	APPENDIX 1: SCHEDULE	55
	APPENDIX 2: REFERENCE DRAWINGS	56
	FIGURE A2-1: SECTOR LAYOUT	57
	FIGURE A2-2: FRONT END LAYOUT.....	58
	FIGURE A2-3: FRONT END HORIZONTAL SYNCHROTRON RAY TRACINGS	59
	FIGURE A2-4: FRONT END VERTICAL SYNCHROTRON RAY TRACINGS.....	60
	FIGURE A2-5: FRONT END HORIZONTAL BREMSSTRAHLUNG RAY TRACINGS.....	61
	FIGURE A2-6: FRONT END VERTICAL BREMSSTRAHLUNG RAY TRACINGS	62
	FIGURE A2-7: BEAMLINE LAYOUT (PLAN & ELEVATION VIEW)	63
	FIGURE A2-8: BEAMLINE HORIZONTAL SYNCHROTRON RADIATION OPTICAL APERTURE RAY TRACINGS.....	64
	FIGURE A2-9: BEAMLINE VERTICAL SYNCHROTRON RADIATION OPTICAL APERTURE RAY TRACINGS	65

FIGURE A2-10: BEAMLINE HORIZONTAL BREMSSTRAHLUNG RAY TRACINGS	66
FIGURE A2-11: BEAMLINE VERTICAL BREMSSTRAHLUNG RAY TRACINGS.....	67
FIGURE A2-12: SHIELDING ENCLOSURE LAYOUT	68
FIGURE A2-13: UTILITY LAYOUT	69
FIGURE A2-14: PERSONNEL SAFETY SYSTEM SCHEMATIC LAYOUT	70
FIGURE A2-15: IXS BEAMLINE CONTROLS LAYOUT	71
APPENDIX 3: LIST OF MAJOR COMPONENTS	75
APPENDIX 4: HUTCH SPECIFICATIONS	77
APPENDIX 5: ADDITIONAL PERFORMANCE EVALUATIONS OF BE CRL	81
A4.1 EFFECTS OF MISALIGNMENTS.....	81
A4.2 EFFECTS OF IMPERFECTIONS	83
REFERENCES	85

Acronyms

APD	Avalanche Photodiode
ASD	Accelerator Systems Division of NSLS-II
BAT	Beamline Advisory Team
BPM	Beam Position Monitor
CCM	Channel-Cut Monochromator
CDR	Conceptual Design Report
COR	Center of Rotation
CPMU	Cryogenic Permanent Magnet Undulator
CRL	Compound Refractive Lens
DCM	Double-Crystal pre-Monochromator
EPS	Equipment Protection System
FE	Front End
FOE	First Optics Enclosure
HFM	Horizontal Focusing Mirror
HRM	High-Resolution Monochromator
IXS	Inelastic X-Ray Scattering
IVU	In-Vacuum Undulator
K-B	Kirkpatrick-Baez
PD	Photodiode (current mode)
PIN	P-Intrinsic-N photodiode
PLC	Programmable Logic Controller
PP	Phase Plate
PPS	Personnel Protection System
PS	Photon Shutter
SDD	Silicon Drift Detector
SR	Storage Ring
SS	Safety Shutter
URM	Ultrahigh Resolution Monochromator
VFM	Vertical Focusing Mirror
XFD	Experimental Facility Division of NSLS-II

1 INTRODUCTION

1.1 Scientific Objective

Momentum-resolved Inelastic X-ray Scattering (IXS) with meV energy resolution provides a powerful technique for studying vibrational dynamics and excitations in condensed matter systems. The scientific objective of this beamline is focused on very high-resolution (1 meV \sim 0.1 meV) IXS experiments. The ultimate goal is to achieve an energy resolution of \sim 0.1 meV, which represents an order of magnitude improvement over the best currently operating instruments in the world. As discussed in the Conceptual Design Report (CDR) [1], such an ultrahigh resolution will provide the scientific community the essential experimental capability to study exotic correlated molecular motions and density fluctuations on the meV energy scale in disordered materials, complex fluids and biomolecular systems, important to understand many of their physical properties. Study of relaxation dynamics, sound propagation and transport properties, phonons in single crystals, surfaces, thin films, confined liquids, systems under extreme pressure, as well as phonons in excited states (pump probe), and exotic excitations in strongly correlated materials, for which an energy resolution of \sim 1 meV is expected to be sufficient for most cases, will also make up a large bulk of the scientific research at this beamline.

As designed in this preliminary phase, the beamline includes two spectrometers, one with an energy resolution of \sim 1 meV and the other \sim 0.1 meV. The optical design of the beamline employs the so-called CDDW [2] monochromator implemented at the asymmetric Si(800) back reflection at a medium energy of 9.13 keV, where the NSLS-II undulator sources have superior performance in both the brightness and spectral flux. For the crystal analyzers of the spectrometers, the optical design takes advantage of the unusually large angular acceptance of the CDW [3,4] or CDDW optics by combining a multilayer collimating mirror with an angular acceptance of \sim 5 mrad in both the horizontal and vertical scattering directions, making it comparable to the angular acceptance of the spherical crystal analyzers currently used in existing IXS spectrometers. The CDW/CDDW monochromator offers also a cleaner resolution function with sharper tails compared to the symmetric Bragg back reflection optics, which will help eliminate spurious background and increase contrast. This novel design, albeit yet to be demonstrated in a working instrument, provides a unique opportunity for NSLS-II to build a fundamentally new IXS spectrometer with unprecedented performance for experiments that are not yet feasible on any existing IXS instrument to date.

The ultimate success of the NSLS-II IXS beamline depends on the success of the 0.1 meV optics R&D program. The CDW/CDDW monochromator is being investigated aggressively by the IXS project team as it is the only scheme we know about that has the potential to achieve the 0.1 meV at a medium energy with a sufficiently large angular acceptance. So far, an energy resolution of 3.7 meV has been achieved with the CDW design by the project team [5]. Even though the 1 meV resolution with the CDW design has not been demonstrated, strong R&D effort is ongoing with yet no real show-stoppers. Therefore, this preliminary design of the IXS beamline and spectrometers presented here is based on our current knowledge of this optical scheme. To reduce the risk, the beamline has been designed to be compatible with an alternative inline 4-bounce monochromator design for 1 meV resolution at 9.13 keV. Similar monochromator design has been proven to deliver \sim 1 meV resolution at 9.4 keV with a 36% spectral efficiency [6]. This monochromator has also the advantage of sharp resolution tails through multiple high index Bragg reflections, although the smaller angular acceptance may limit its efficiency for use as a crystal analyzer.

In line with the optics R&D program and budgetary constraints, the beamline development will proceed with a baseline scope which includes all essential components to enable the 1 meV resolution capability of the beamline with the provision for the mature scope to be fully developed. The baseline scope include the enclosure, beam transport, utilities, white beam components, high heatload optics, beam conditioning optics to achieve a fine focus of \sim 10 μ m (H) \times 5 μ m (V) spot size, Personnel Protection System (PPS), Equipment Protection System (EPS), the 1 meV spectrometer with a single analyzer, beamline controls, and project management. The total estimated cost for the baseline scope of the beamline based on the details of the current design stands at \$11.107M. The mature scope is designed to develop the experimental capabilities for the 0.1 meV resolution, which include a channel cut monochromator and the 0.1 meV development instrument, additional focusing optics to improve the momentum resolution, a phase plate optics to improve momentum transfer range, as well as a second IVU22-3m insertion device to double the incident flux. The additional cost for the mature scope is estimated at \$4.8M.

1.2 Beamline Advisory Team (BAT)

The IXS Beamline Advisory Team (BAT) is made up by a group of world-class scientists having a broad range of complementary scientific expertise and experiences in areas relevant for the NSLS-II IXS beamline. Current membership includes:

Clement Burns (spokesperson)	Western Michigan University
Alfred Baron ^(*)	RIKEN/SPring-8
Sow-Hsin Chen	Massachusetts Institute of Technology
John Hill	Brookhaven National Laboratory
Michael Krisch	European Synchrotron Radiation Facility
Ho-Kwang Mao	Carnegie Institution of Washington
Tullio Scopigno	Universita' di Roma "La Sapienza"
Stephen Shapiro	Brookhaven National Laboratory
Yuri Shvyd'ko	Argonne National Laboratory

^(*) Member since March 2010.

A short summary of their expertise and experience is given below:

Clement Burns, Professor at WMU; expert on IXS on highly correlated systems; Principal Scientist (until 2006) for the Medium Resolution IXS Instrument at Sector 30 of APS; PI on DOE Proposal for Inelastic X-Ray Scattering Sector (Sector 30) at APS.

Alfred Baron, Head of the RIKEN Materials Dynamics lab, leader of the Spring-8/JASRI IXS team and an expert in ~ meV resolution IXS studies, both in instrumentation and experiments.

Sow-Hsin Chen, Professor at MIT; distinguished expert in neutron, visible light and inelastic X-Ray scattering of soft condensed matters, and molecular dynamics of these systems; Expert in dynamical properties of water with strong current emphasis on biological systems.

Michael Krisch, Scientist at ESRF; Spokesperson for the high resolution IXS beam line ID28 at the ESRF since 1996; Expert in ~ meV resolution IXS studies, both in instrumentation and experiments.

John Hill, Physicist at BNL; IXS experience at NSLS and APS studying electron dynamics in simple metals and strongly correlated electron systems, using resonant and non-resonant techniques; Director of the IXS-CAT (Sector 30) at APS (2002 – 2008); Director of the Experimental Facilities Division of NSLS-II (2006 – 2008).

Ho-Kwang (David) Mao, Senior Scientist at Geophysical Lab of CIW; Vast experience in high pressure studies of all sorts; Expert in use of numerous spectroscopies (including IXS) to study vibrational excitations under high pressure and extreme temperature conditions; Director of the high pressure beam line (HP-CAT) at the APS.

Tullio Scopigno, Professor at University of Roma "La Sapienza"; Expert in spectroscopy (including time resolved Brillouin and Raman spectroscopy) of glassy, fluid, polymer and soft matter systems, and conceptual methodologies for describing these systems.

Steve Shapiro, Senior Scientist at BNL; Expert in neutron scattering, high resolution studies of phonons and phonon linewidths in single crystals, and studies of phase transitions.

Yuri Shvyd'ko, Senior Scientist at APS, ANL; Expert in X-Ray optics, including work on X-Ray interferometry, Mössbauer, and asymmetric Bragg reflections; Originated and tested the basic idea for the new inelastic X-Ray spectrometer described herein.

1.3 The IXS Project Team

Advised by the BAT, the NSLS-II IXS Project Team is responsible for the R&D of the ultrahigh resolution optics and the design, construction and commissioning of the NSLS-II IXS beamline and spectrometers.

The following is the list of current members (as of September 2010) and their individual responsibilities:

- Yong Cai**, Physicist, NSLS-II IXS Group Leader
- Scott Coburn**, Engineer (matrixed with the Beamline Support Group, XFD)
- Alessandro Cunsolo**, Associate Physicist, NSLS-II IXS Beamline Scientist
- Jeff Keister**, Associate Physicist, NSLS-II R&D Beamline Scientist
- Nalaka Kodituwakku**, Postdoctoral Fellow, crystal optics R&D
- David Levy**, Technician, NSLS-II R&D beamline support (temporary)
- Leo Reffi**, Mechanical Designer (matrixed with the Design Group, ASD)
- Yuriy Stetsko**, Visiting Scientist, X-Ray dynamic diffraction theory
- Bill Struble**, Technician, crystal fabrication and lab support

Furthermore, Scott Coburn, Alessandro Cunsolo, Jeff Keister, Leo Reffi and Yuriy Stetsko contributed to the write-up and drawings presented in this document.

1.4 Acknowledgement

The following BNL staff are acknowledged for their contributions to the materials presented here.

- Andy Broadbent**, Beamlines Manager (XFD, NSLS-II)
- Oleg Chubar**, Beamline Scientific Support, insertion device optimization, wave front propagation (XFD, NSLS-II)
- Lewis Doom**, Engineer, Front-end design (ASD, NSLS-II)
- Viswanath Ravindranath**, Engineer, Heat load analysis (ASD, NSLS-II)
- Kathleen Robinson**, Editor (NSLS-II)

In addition, the following individuals are acknowledged for their contributions to the design effort of the beamline, particularly in connection with the optics R&D:

- Marcelo Honnicke** (past member of the IXS Project Team), Professor, Universidade Federal de Goias, Brazil.
- Xianrong Huang** (past member of the IXS Project Team), Optics and Detector Group, APS, Argonne National Laboratory.

2 INSERTION DEVICE

The optimization of the insertion device for this beamline and the choice of the straight section have been discussed in detail in the Conceptual Design Report (CDR) [1]. The primary goal is to maximize the spectral flux of the device at the operation energy of 9.13 keV within the current lattice design of the NSLS-II storage ring, while meeting the minimum requirement of 10^9 photons/sec/0.1-meV at the sample in order to perform experiments with the ultimate energy resolution of 0.1 meV. This translates to a minimum required spectral flux of 10^{15} photons/sec/0.1%bw at the source assuming an overall 10% optical efficiency of the beamline optics. The conclusion remains essentially the same to date: the best room-temperature device for this beamline is the IVU22-6m in-vacuum undulator installed in a high- β straight section, which delivers a spectral flux of $\sim 1.6 \times 10^{15}$ photons/sec/0.1%bw at 9.13 keV. Further improvements can be achieved using cryogenic permanent magnet undulators (CPMU) with, e.g., the LN2 cooled PrFeB magnet from NEOMAX [7]. Among the possible cryogenic devices considered, the CPMU17-5.7m provides the best performance at 9.13 keV with $\sim 75\%$ gain in flux compared to the IVU22-6m. Table 1-1 lists the basic parameters of the IVU22-6m and CPMU17-5.7m undulators. The expected photon beam size and divergence at 9.13 keV are listed in Table 1-2. Both the IVU22-6m and CPMU17-5.7 m are planned to be hybrid permanent-magnet undulators, with Vanadium Permendur alloy being used as pole material (the saturation magnetization level is ~ 2.5 T). The spectral performance of the IVU22-6m and the CPMU17-5.7m are compared with a few other devices for the high- β straight section in Figure 1-1 [8].

Table 1-1. Basic parameters of the IVU22-6m and CPMU17-5.7m undulators.

Device Name	IVU22-6m	CPMU17-5.7m
Device Type	PMU (NdFeB @ 300 K)	PMU (PrFeB @ 77 K)
Br [T]	1.12	1.4
Period [mm]	22	17
Length [m]	6	5.7
Minimum Gap @ High- β Straight [mm]	6.95	6.79
Maximum Field B_{\max} [T]	0.74	0.73
Maximum Deflection K_{\max} [T]	1.52	1.16
Total Power [kW]	9.4	8.6
On-axis Power Density [kW/mrad ²]	90	104
Horizontal Fan Angle ^(*) [mrad]	0.77/1.34	0.64/1.24
Vertical Fan Angle ^(*) [mrad]	0.79/1.26	0.77/1.22

^(*) The fan angles of the radiation quoted here are for the total power density as seen at 16 m from the source, and take into account the effects of the source length. The two values quoted are for the points where the power density falls to values that are 1% and 0.1% of the central value. These values are used for the design of the XBPM and fixed mask of the front end. Note that the central cone fan angle containing the useful photon flux is much smaller.

Table 1-2. The RMS photon source size and divergence of the IVU22-6m and CPMU17-5.7m at 9.13 keV.

Device	Harmonic	E (keV)	σ_{Tx} (μm)	σ_{Ty} (μm)	σ'_{Tx} (μrad)	σ'_{Ty} (μrad)
IVU22-6m	5 th	9.13	134.7	8.698	9.965	7.759
CPMU17-5.7m	3 rd	9.13	111.8	7.299	8.066	6.240

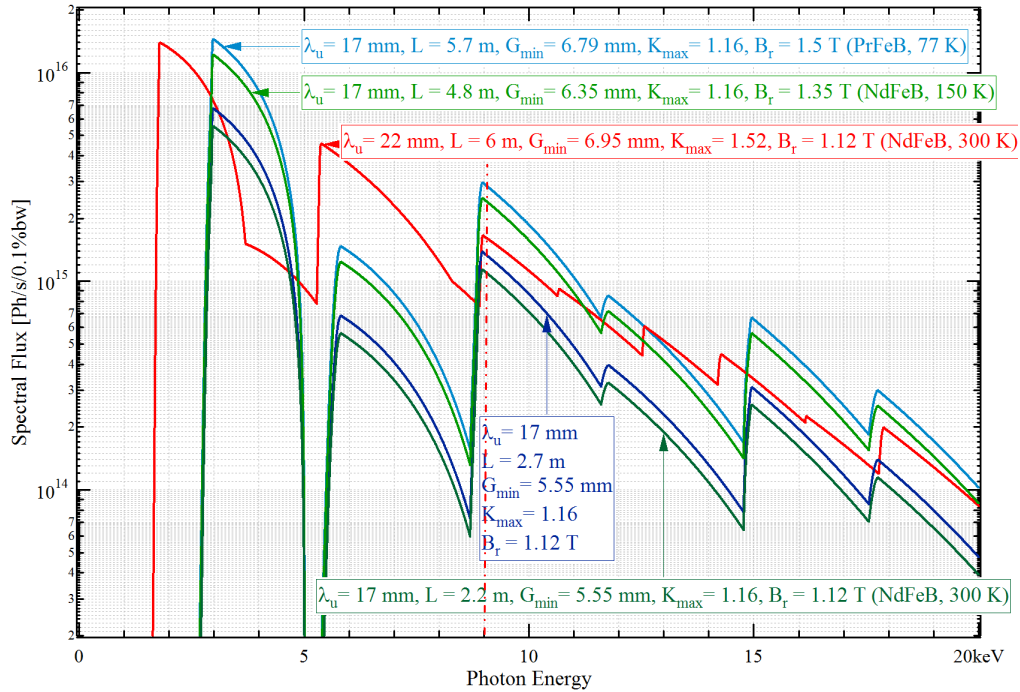


Figure 1-1. Comparison of the spectral performance of several undulators, operating either at room temperature or at cryogenic temperatures, in a high- β straight of the NSLS-II storage ring filled with 500 mA current. The dash-dotted line marks the operation energy of 9.13 keV.

2.1 Baseline Device

Due to budgetary constraints, the baseline scope of the beamline includes only a 3-m long IVU22-3m device for experiments at the 1 meV energy resolution. The IVU22-3m device delivers half of the performance of the full IVU22-6m device, with a peak spectral flux of $\sim 8 \times 10^{14}$ photons/sec/0.1%bw at 9.13 keV. With this device, up to $\sim 8 \times 10^9$ photons/sec/1-meV flux at the sample may be expected. This is to be compared with the $\sim 4 \times 10^9$ photons/sec/1.5-meV intensity currently achievable at existing IXS instruments in the world [9].

2.2 Upgrade Options

Upgrade options include the addition of the second IVU22-3m, and the cryogenic devices. The second IVU22-3m device is a part of the mature scope for the beamline, and will be required to meet the minimum acceptable spectral flux of 10^{15} photons/sec/0.1%bw at the source for experiments with 0.1 meV resolution. The design of the IVU22-3m should allow the integration of the second device with proper phasing, so that the two devices can function as a single one. Phase error of up to 2 degrees (RMS) is acceptable and is expected to cause less than 5% of reduction in spectral flux for the 5th harmonic at ~ 9.13 keV [10].

The cryogenic devices such as the CPMU17-5.7m offer another attractive upgrade option. However, these devices require significant R&D effort to address the technical challenges associated with the cryogenic cooling of the magnets. Furthermore the field strength of PrFeB under cryogenic temperature is still a matter of research and development. So far, no decision has been made to pursue the development of these cryogenic devices within the project phase. Should such devices become available in the future, we will actively pursue the CPMU17-5.7m for the beamline. An even more appealing option would be to extend the high- β long straight section to double the length, in which one could potentially install two of these cryogenic devices and be able to more than triple the spectral flux of the IVU22-6m. This last option, however, does seem unlikely at this point given the potential impact on the neighboring straights and the storage ring.

The use of the cryogenic devices may limit somewhat the tuning range of the insertion device, particularly at energies covered by the 2nd harmonic (5-9 keV) of the CPMU17-5.7m where the spectral intensity drops by as much as an order of magnitude. Since the beamline will be operated primarily at the energy of 9.13 keV, tunability is not a major concern. This operating energy of 9.13 keV is dictated by the design of the CDW/CDDW monochromator. If the alternative 4-bounce monochromator is used, there will be no impact expected on the choice of the insertion device as the 4-bounce monochromator can be designed to operate at the same energy as we will discuss in Section 4.

Finally, another upgrade option which was recently proposed by Oleg Chubar is the use of the so-called adaptive undulators. These are essentially segmented undulators with varied magnetic periods to produce the required field strength for the 9.13 keV photons with each segment at a gap value meeting the “stay-clear” criterion set by the β -function along the straight section (see Figure 1-2). A 15-segment (each 0.5 m long for a total length of 7.5 m) room temperature adaptive undulator could produce more than 60% gain in spectral flux compared to the IVU22-6m device. This performance is comparable to that of the CPMU17-5.7m, but without the complexity associated with the cryogenic cooling of the magnets.

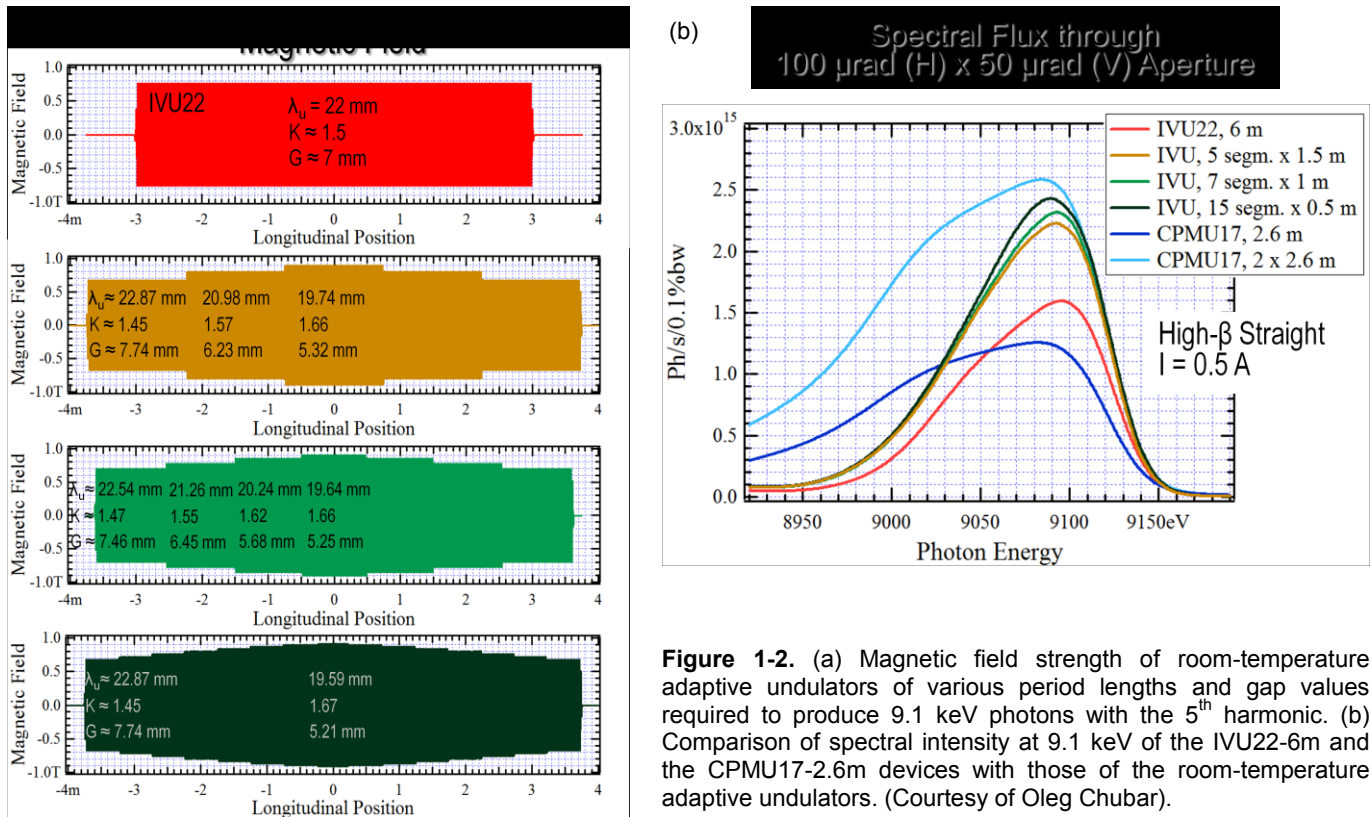


Figure 1-2. (a) Magnetic field strength of room-temperature adaptive undulators of various period lengths and gap values required to produce 9.1 keV photons with the 5th harmonic. (b) Comparison of spectral intensity at 9.1 keV of the IVU22-6m and the CPMU17-2.6m devices with those of the room-temperature adaptive undulators. (Courtesy of Oleg Chubar).

3 FRONT END

3.1 General Layout

The IXS beamline Front End (FE) adopts the standard NSLS-II front end designed by the Front End Group led by Lewis Doom with the exceptions that a set of removable beryllium (Be) compound refractive lenses (CRL) will be installed at ~ 19.2 m from the source to provide pre-focusing of the source for the high-resolution optics, and that it is required to handle the full power load of the IVU22-6m and/or the CPMU17-5.7m device as listed in Table 2-1.

A 3D layout of the IXS front end is shown in Figure 3-1. A component layout drawing showing the location and dimensions of the components is included in Appendix 2. The Front End Conceptual Design Report should be consulted for the design details in consideration of radiation safety, heat load management and functionality of each standard component¹¹. Section 3.2 provides a brief description and functionality of each of these components and specifications. Section 3.3 describes the Be-CRL assembly.

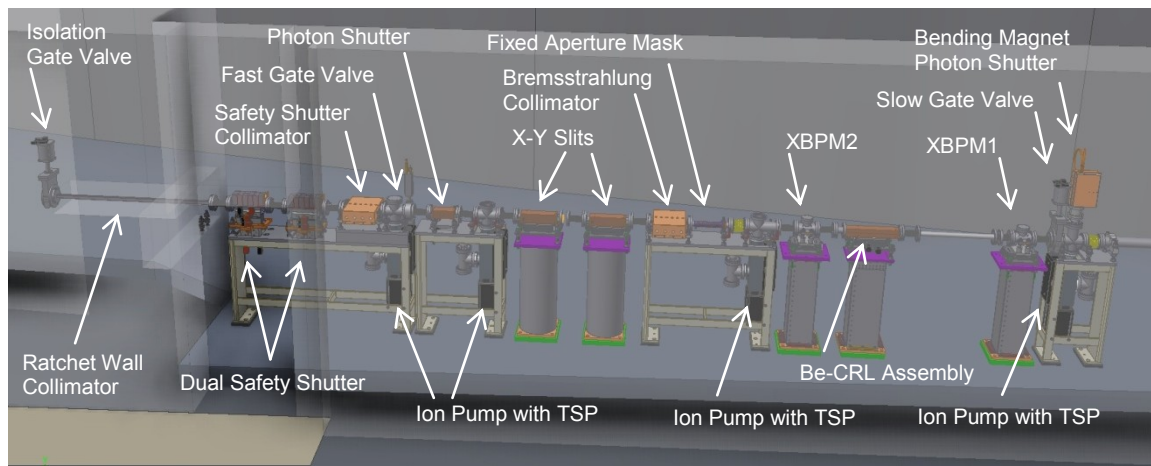


Figure 3-1. 3D model of the Front End layout for the IXS beamline.

3.2 Brief Description of Major Components and Specifications

3.2.1 Bending Magnet Photon Shutter (BMPS)

The BMPS is a part of the storage ring vacuum system and is designed to protect the Slow Gate Valve (SGV) from bending magnet radiation before the upstream straight is fitted with an insertion device and a complete front end. The BMPS will also be used to protect the SGV if the front end needs to be isolated from the machine. If it is required to close the SGV during machine operation, the insertion device power will need to be reduced first followed by closing the BMPS and then the SGV.

3.2.2 Slow Gate Valve (SGV)

The Slow Gate valve is a part of the Storage ring vacuum system and is included to isolate the machine and FE, but will not withstand white beam from IDs or BM radiation. The SGV is controlled and monitored by storage ring vacuum PLC using a voting scheme with inputs from vacuum sensors at both sides of the valves and position of BMPS.

3.2.3 Beam Position Monitor 1 (XBMP1)

The XBPMs are designed to work with the insertion devices specified.

Material	Water-cooled mountings and Tungsten blades
Power protection	A pre-mask may be included if design considerations dictate
Motorized	Yes to allow centering of the device around the beam.

The XBPMs shall be mounted on X/Y stages with the following specifications;

Position stability	Low stability: x, y = 2 μm or better over any 8-hour period
Speed	No particular requirement
Position resolution	x and y = 1 μm (expected value: \ll 1 μm guaranteed).

The X/Y stage for the XBPM and the X/Y slits are expected to be the same design, including the stand, where possible. One Design being considered for the XBPMs is shown below in Figure 3-2.

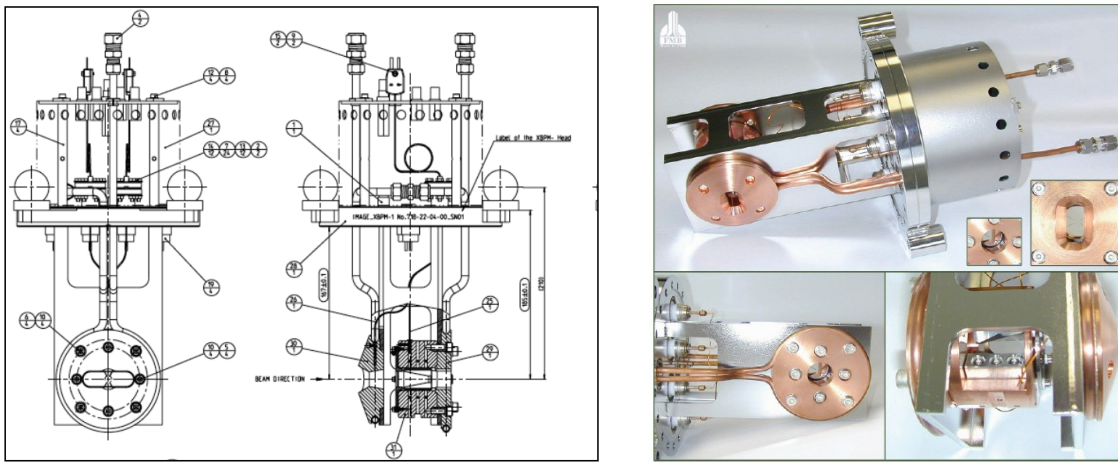


Figure 3-2. Design of the XBPM being considered by the Front End Group.

3.2.4 Beam Position Monitor 2 (XBPM2)

This device and the X/Y stages are identical to XBPM1. However, the blades will be relocated to avoid masking effects.

3.2.5 Fixed Aperture Mask (FAPM)

The fixed aperture mask (see Figure 3-3) defines the radiation fans to the First Optics Enclosure (FOE). The vertical angular opening is 0.3 mrad and the horizontal angular opening is 0.5 mrad. No tolerance will be added to the mask for mis-positioning. However, a manufacturing tolerance of ± 0.2 mm for the aperture (at the downstream end of the mask) will be included in the downstream fan definition.

3.2.6 Bremsstrahlung Collimator (BC1)

The Bremsstrahlung collimator prevents the Bremsstrahlung radiation fan from exiting the shield wall. This should be as tight to the beam as reasonable without undue mechanical tolerances or alignment difficulty.

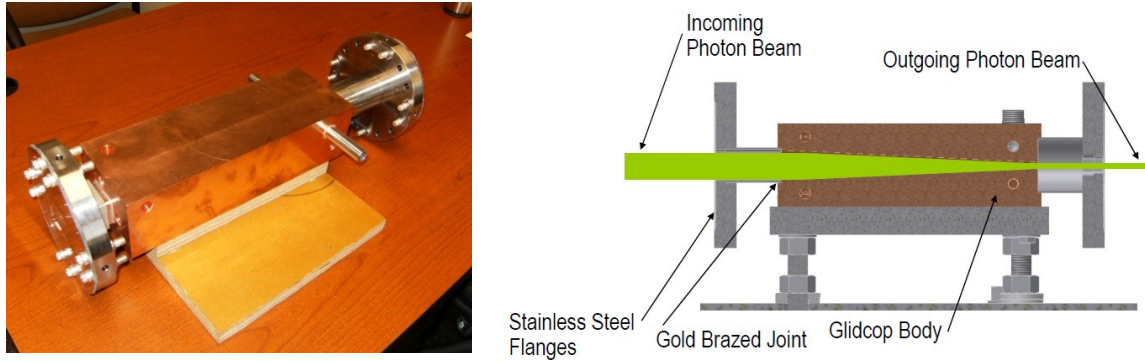


Figure 3-3. Photo and schematic view of the Fixed Aperture Mask.

3.2.7 X-Y Slits

A pair of white-beam X-Y slits is located immediately downstream of the first lead collimator to further reduce power loads and the angular acceptance.

The X-Y slits shall be of the SPring-8 dual “L” type design, connected with bellows to allow full adjustment of all four “blades” via two X-Y stages. The specifications are as follows;

Material	Water-cooled Glidcop with Tungsten blocks
Power protection	A pre-mask may be included if design considerations dictate
Maximum opening angle	Sufficient to allow full FAPM fan to continue to the FOE without clipping.
Motorized	Required to allow selection of any part of the FAPM fan. The same X/Y stage shall be used for the XBPMS.
Aperture stability	Low stability: $\Delta x, \Delta y = 4 \mu\text{m}$ or better over any 8-hour period

The aperture stability specification is governed by differential movement between the two X/Y slit units; the specification will be met with high stability X/Y stages. For the high stability stages some form of additional coupling between stands may be required to constrain any differential movement.

3.2.8 Photon Shutter (PS)

The photon shutter is required to stop the full white beam. For insertion devices this is expected to be water cooled Glidcop at a grazing incidence angle. The Photon shutter length will be 30 cm.

3.2.9 Fast Gate Valve (FV)

The fast valve is to shut within a few milliseconds once triggered by FV sensors located in the FE and the beamline whenever there is a sudden increase of pressure of a few decades. The stored beam has to be dumped prior to FV closing and the cause then investigated and mitigated.

3.2.10 Bremsstrahlung Collimator (BC2)

Bremsstrahlung collimator 2 protects the downstream dual safety shutter. The BC1, BC2, and the ratchet wall collimator should be made as tight as possible using a combination of in-vacuum Tungsten and out-of-vacuum lead designs.

3.2.11 Safety Shutter (SS)

The safety shutter is actually a pair of shutters, required for redundancy, and is air actuated with independent redundant and diverse position sensing. An external lead design is being used as shown below.

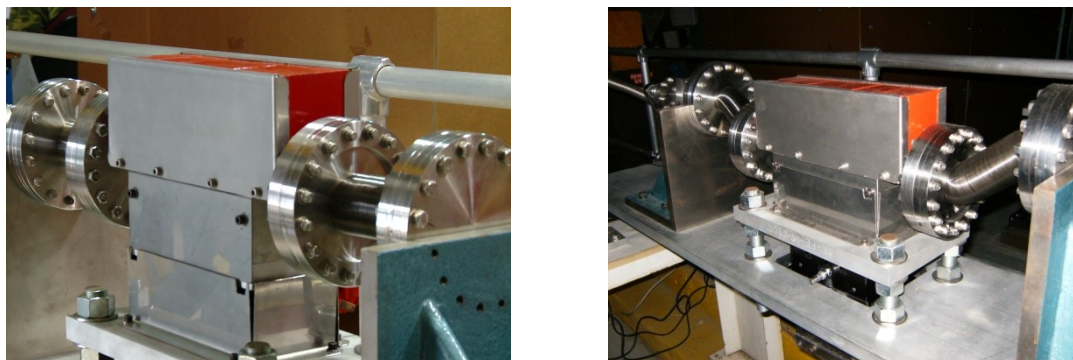


Figure 3-4. Photos of the safety shutter.

3.2.12 Ratchet Wall Collimator

The Ratchet Wall Collimator provides the final collimation of Bremsstrahlung radiation between the interior and exterior of the Ratchet Wall. Mounting bracket on the inner and outer faces of the ratchet wall will support the Beam Pipe with lead and Poly being stacked around. Final definition of the stacking arrangement of the lead is in progress.

3.2.13 Isolation Gate Valve

This slow gate valve, pneumatically actuated, with position sensing switches will be monitored and controlled by the SR vacuum PLC using vacuum sensors in the FE and beamlines. The slow gate valve is the last component downstream and is considered a part of the Front End. This valve cannot be removed after commissioning and must be protected from any exposure to beam.

3.3 Special Requirements (Beryllium Compound Refractive Lenses)

As a part of the optical design for the IXS beamline (see Section 4), a set of Be CRLs will be inserted between the two X-Ray beam position monitors (XBPM1 and XBPM2) at ~ 19.2 m from the source to provide close to 1:1 focusing of the beam for the high resolution monochromator. A water-cooled rectangular tapered 1×1 mm² aperture will be placed in front of the Be CRLs to protect the CRLs from being exposed to excessive heat power (see Figure 3-5). Except for the smaller opening, this rectangular taper aperture will be of the same design as the fixed aperture mask (FAPM). The support mechanism will be identical to that for the X-Y slits with the same motion range, resolution, repeatability and stability, with additional tilting (pitch and yaw) adjustments to align the optical axis of the CRLs to the beam axis. A 30 μ m thick highly oriented pyrolytic graphite (HOPG) filter will be used also before the Be CRLs to remove the low energy heat power. The optical and thermal analysis of this assembly is presented in Section 4.

This Be CRLs assembly is designed also to operate in a by-pass mode in which the Be CRLs and the HOPG filter will be removed from the beam, allowing the undulator beam passing thru without heating any part of the assembly. With the Be CRLs in place, however, the XBPM2 will no longer function properly. In the standard front end design, XBPM2 is intended to provide monitoring of the x-ray beam exit angle from the undulator source in conjunction with XBPM1 and as a redundancy to XBPM1. Without it the performance of the front end will not be affected. Further beam position monitoring will be provided in the FOE, upstream of the DCM.

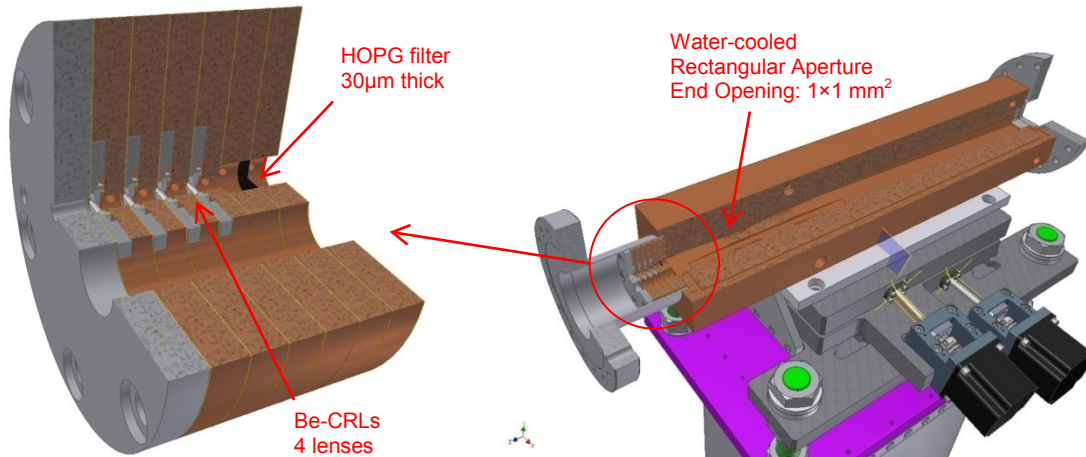


Figure 3-5. 3D model of the Be-CRL assembly.

3.4 Ray Tracings

Bremsstrahlung and X-Ray tracings have been performed to confirm the apertures and locations of the various front end components meeting the safety requirements as stimulated by Ref [12]. The Front End ray tracings are included in Appendix 2.

3.5 Finite Element Analysis

The total power of the IVU22-6m (CPMU17-5.7m) is 9.4 (8.6) kW and the peak power density is ~90 (104) kW/mrad² (see Table 2-1). In normal operation mode, the sides of fixed mask will intercept 2.4 kW and allow 7 kW of power through its downstream aperture (0.5 mrad (h) by 0.3 mrad (v)). The 7 kW power will be intercepted by the downstream photon shutter in the event of a beam dump. As a conservative approach and to account for beam mis-steering, in the analyses it was assumed that the fixed mask intercepts the total power of 9.4 kW delivered by the undulator and also it was assumed that the beam can hit either the horizontal surface or the vertical surface. The peak power density at the fixed mask location (20.65 m from the center of the straight section) is 215 W/mm² which results in a maximum temperature of 265 °C. The peak power density at the photon shutter location (23 m) is 171 W/mm², which results in a peak surface temperature of 262 °C. For the design of NSLS-II high heat load components we use the following failure criteria:

- Photon shutters and XY-slits: For these critical components which intercept the central portion of the beam, the maximum allowable temperature is ~300 °C. This temperature limit ensures that the thermal stresses will be below the yield limit of Glidcop Al-15 (330 MPa) at room temperature.
- Fixed Masks: Since these components see the tail portion of the beam and also are less likely to experience thermal fatigue failure due to continuous exposure to the beam, the maximum allowable temperature can be 400 °C. This condition ensures a fatigue life greater than 10,000 cycles.

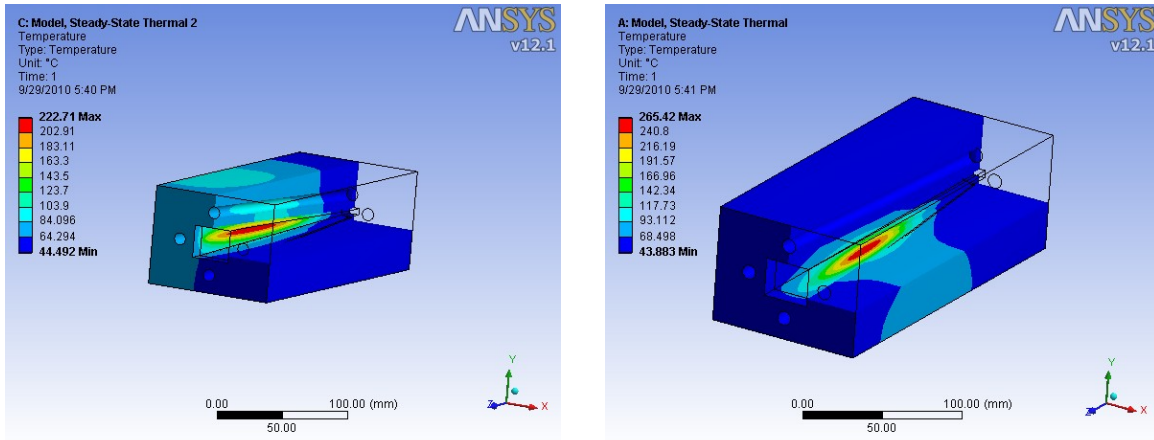


Figure 3-6. FEA heat load analysis of the fixed aperture mask located at ~20.65 m from the center of the straight section. Conditions and results of the analysis: absorbed power ~9.4 kW; vertical incidence angle 2.7°; horizontal incidence angle 3°; minimum length of the fixed mask 24 cm; peak temperature ~265 °C.

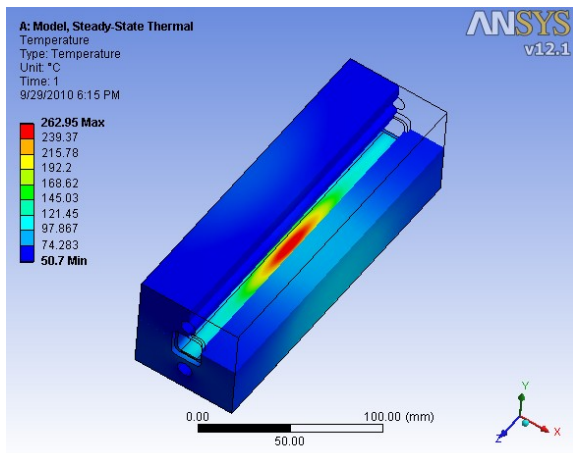


Figure 3-7. FEA heat load analysis of the photon shutter. Conditions and results of the analysis: absorbed power ~7 kW; beam incidence angle 3.5°; minimum component length 20 cm; peak temperature ~262 °C.

4 BEAMLINE DESIGN

4.1 Overview

Figure 4-1 presents an overview of the beamline. A reference drawing with dimension is provided in Appendix 2 (Figure A2-7). The layout is based on the optical design as discussed in detail in the Conceptual Design Report [1]. Major beamline components are listed in Appendix 3. Figures 4-2 and 4-3 provide a zoom-in view of the beamline components located in each hutch. As shown, there are in total four hutches (from right to left): Hutch A is the first optical enclosure (FOE) and houses the high heatload Double Crystal Monochromator (DCM). Hutch B is designed for the High-Resolution Monochromator (HRM) and for additional beam conditioning optics such as the Channel-Cut Monochromator (CCM) and the Phase Plate (PP) which are in the mature scope. Hutch C's primary function is for the installation of a set of K-B mirrors in the mature scope for achieving high momentum (Q) resolution and a optics testing bench. Hutch D houses the set of K-B mirrors in the baseline scope for achieving fine focusing and the endstation with two spectrometer arms; one designed for 1 meV resolution with a 5 m long arm and a large scattering angle range from -10 to 135 degrees and the other for 0.1 meV resolution with a 10 m arm and a limited scattering angle range (-5 to 15 degrees). The baseline scope includes only the 5 m arm with a single analyzer. All hutches except Hutch D have a monochromatic beam shutter. The shutters for Hutch A and Hutch B are designed for maintaining the heat load on the monochromator crystals while access to the downstream hutches is required. The shutter for Hutch C enables access to the end station hutch while Hutch C is being used for optics experiments. Further details of these hutches will be presented in Section 6.1.

In the following, details of optical components are presented in Section 4.2 to Section 4.4. Section 4.5 discusses beam transport components. The remaining major components are presented in Section 4.6.



Figure 4-1. A 3D CAD rendering of the IXS beamline. There are in total four hutches (from right to left): Hutch A is the First Optical Enclosure (FOE), Hutch B houses the high-resolution monochromators, Hutch C is designed to house a set of K-B mirrors for achieving high Q resolution as well as for optics testing, and Hutch D is for the IXS endstation with a set of K-B mirrors for achieving fine focusing.

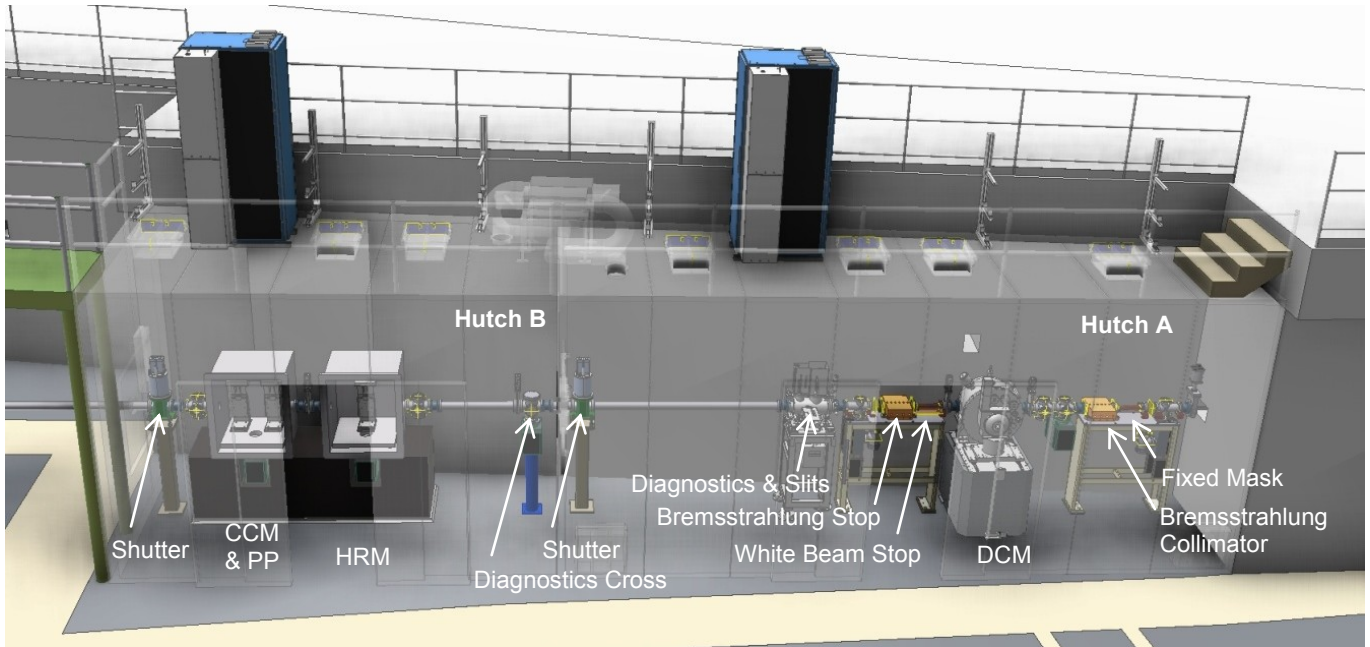


Figure 4-2. Details of Hutch A (FOE) and Hutch B with major components annotated. DCM: Double Crystal pre-Monochromator; HRM: High Resolution Monochromator; CCM: Channel Cut Monochromator (mature scope); and PP: Phase Plate (mature scope).

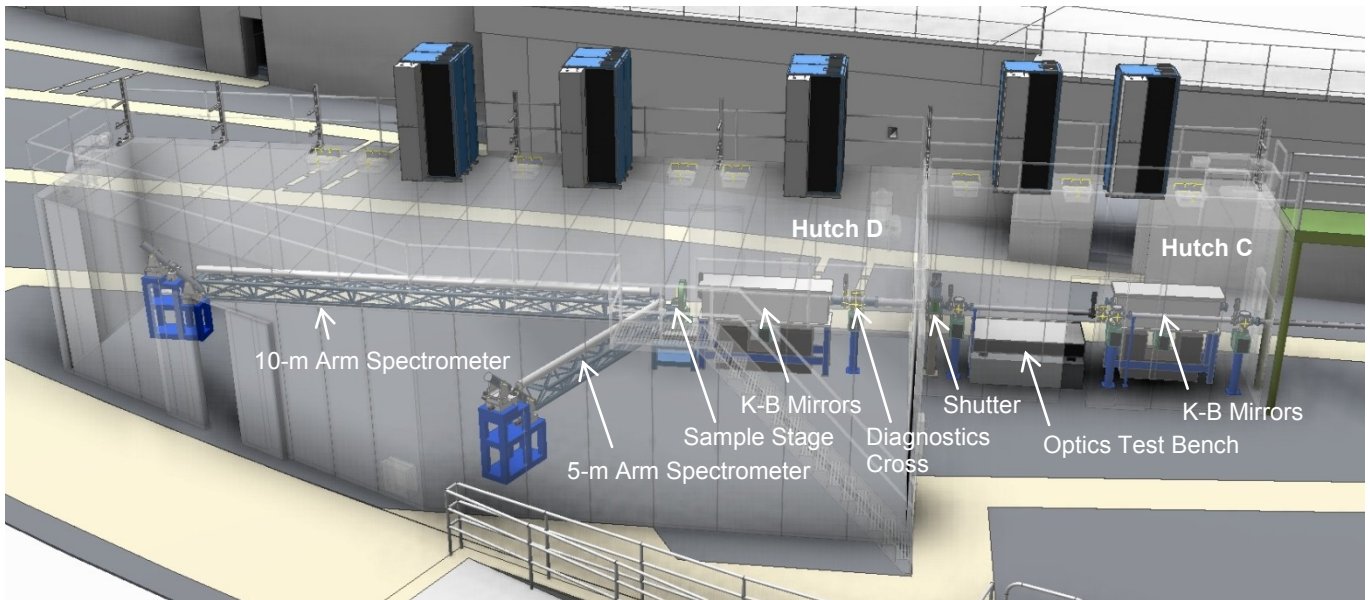


Figure 4-3. Details of Hutch C and Hutch D with major components annotated. The K-B mirrors in Hutch C and the 10-m arm in Hutch D are part of the mature scope.

4.2 High Heat Load Optics

There are two high heatload optical components for the IXS beamline. The first one is the Beryllium Compound Refractive Lens (CRL) installed in the Front End (FE) providing close to 1:1 focusing of the vertical source for the high-resolution monochromator. The second one is the double crystal pre-monochromator (DCM). Table 4-1 summarizes the power delivered to, absorbed by and transmitted through these components from the IVU22-6m undulator operating at the minimum gap of 6.95 mm with 500 mA ring current. This information forms a part of our design considerations. The technical details and their specifications are presented and discussed in the following.

Table 4-1. Calculated power load from the IVU22-6m operating at 9.13 keV with the 5th harmonic ($K \sim 1.5$) on various components in the front end and on the double crystal monochromator (DCM) under normal operation conditions.

Beamline Component	Aperture (H×V) μrad^2	Incident Power [W]	Power Absorbed [W]	Power Transmitted [W]	Notes
CASE I: With Be-CRLs Assembly in the Beam					
Be-CRL Collimator	~50 x 50	9,328	9,100	228	End opening: 1×1 mm ² @ 19.2 m
HOPG filter	-	228	62	166	Thickness: 30 μm
Be CRLs	-	166	52	114	N = 4, R = 0.3 mm, d = 0.1 mm
Fixed Mask	500 x 300	114	0	114	@ ~20.65m
X-Y Slits	60 x 50	114	0	114	@ ~21.8 m
DCM	-	114	114	~0 ^(*)	@ ~29.7 m from source
CASE II: With Be-CRLs Assembly in By-pass Mode					
Fixed Mask	500 x 300	9,328	2,292	6,946	@ 20.65 m from source
X-Y Slits	60 x 50	6,946	6,693	253	End opening for 6 σ of beam
DCM	-	253	253	~0 ^(*)	Worst heatload scenario for DCM

(*) The power transmitted through the DCM is less than 0.5 mW.

4.2.1 The Beryllium Compound Refractive Lens (CRL)

The CRL will be located at 19.2 m from the center of the undulator source in the Front End. Its primary function is to focus the vertical source to be immediately upstream of the CDDW high-resolution monochromator (HRM) in order to reduce the virtual source size broadening caused by the large angular divergence of the exit beam expected from the CDDW HRM [1]. Detailed discussions of the working principle and considerations for optimization of these lenses for specific applications can be found in the literature (see, for example, Ref. [13] and Ref. [14]). CRLs are widely used as focusing and collimating optical elements at high-energy third generation synchrotrons, including those under undulator white beams (e.g., the IXS-CAT at Sector 30 of the APS). Due to the lower energy of the NSLS-II storage ring, however, more severe heatload is expected. For the present application, we choose beryllium as the material to minimize absorption loss. The lens parameters are dictated by the required aperture size (acceptance), and by the possible physical locations of the CRL and the CDDW HRM along the beamline. Furthermore, the demagnification factor has to be chosen to ensure that the resulted divergence of the incident beam onto the CDDW HRM be less than 20 μrad FWHM. This is required to achieve the 0.1 meV resolution by the addition of a channel-cut monochromator (CCM) after the CDDW HRM in the mature scope [1].

Table 4-2 summarizes the parameters of the Be CRL for the required performance as stated above. These are one dimensional parabolic lenses with a radius of curvature of 0.3 mm. Figure 4-4(a) shows the cross sectional profile of

a lens with an apex thickness of 0.1 mm. A total of 4 lenses are required to produce a focal length of 9.176 m for the 9.13 keV photons, so that the image is located conveniently at 36.776 m ($= p + q$) from the center of the undulator source. The RMS acceptance of the lens as defined in Ref. [13] is 0.503 mm, which is sufficiently large compared to the vertical beam size of 0.345 mm FWHM at the position of the CRL [15]. The vertical focal size and beam divergence after the double crystal pre-monochromator (DCM) as obtained by the Shadow ray tracings are 29.4 μm and 19.4 μrad FWHM, respectively. Evaluation by partially coherent wavefront propagation simulations without the DCM produces similar results [16], which are presented in Figure 4-5.

These one-dimensional Be CRLs are available commercially, such as those fabricated by Prof. B. Lengeler and sold via RWTH Aachen [17]. Figure 4-4(b) shows a 3D model of such lenses. The fabrication of these lenses is done by printing rather than by machining which is believed to produce lenses of higher quality with minimum internal defects. It involves punching a 5 mm diameter and 1 mm thick Be disk onto a Kovar (an iron-nickel-cobalt alloy with thermal conductivity of 18 W/m·K) frame with a hole of 5.1 mm in diameter [18]. The frame is precision machined to $20 \times 20 \times 2 \text{ mm}^3$ in size with an alignment key to facilitate alignment of the optical axes of individual lenses to micron accuracy. Minimum apex thickness is guaranteed to be no more than 80 μm . These commercial lenses therefore appear to meet our requirements so long as lenses with the 0.3 mm radius of curvature are available.

Table 4-2. Performance parameters of the Be Compound Refractive Lenses.

Material	Beryllium
E (photon energy) [eV]	9132
$\delta = 1 - n$	$4.0867 \times 10^{-6(*)}$
Shape	One dimensional parabolic
R (radius of curvature) [mm]	0.300
d (lens apex thickness) [mm]	0.100
N (number of lenses)	4
F (Focal distance: $F = R/(2N\delta)$) [m]	9.176
p (source-CRL distance) [m]	19.200
q (CRL- focus distance) [m]	17.576
RMS lens acceptance [mm] [13]	0.503

(*) From CXRO (Center for X-Ray Optics) database: http://henke.lbl.gov/optical_constants/

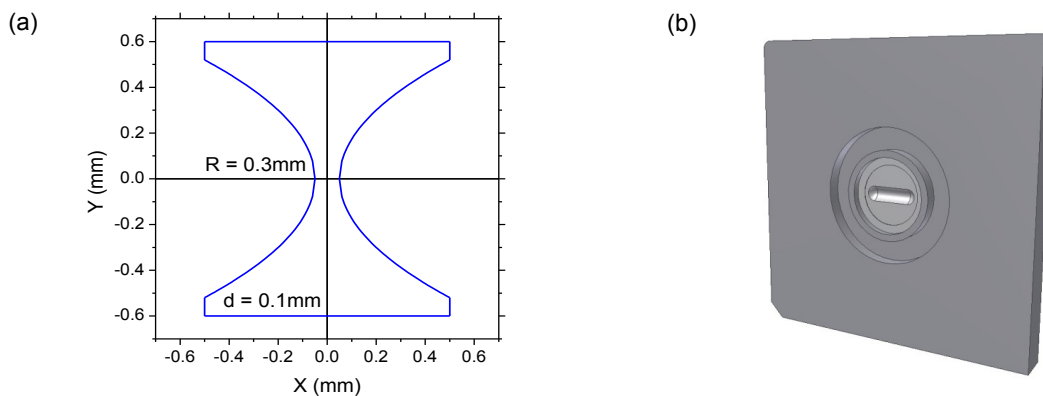


Figure 4-4. (a) Cross sectional profile of the one-dimensional Be Compound Refractive Lens. R is the radius of curvature and d the apex thickness. (b) A 3D model of the one-dimensional Be CRL fabricated by Prof. B. Lengeler and available from RWTH Aachen [17].

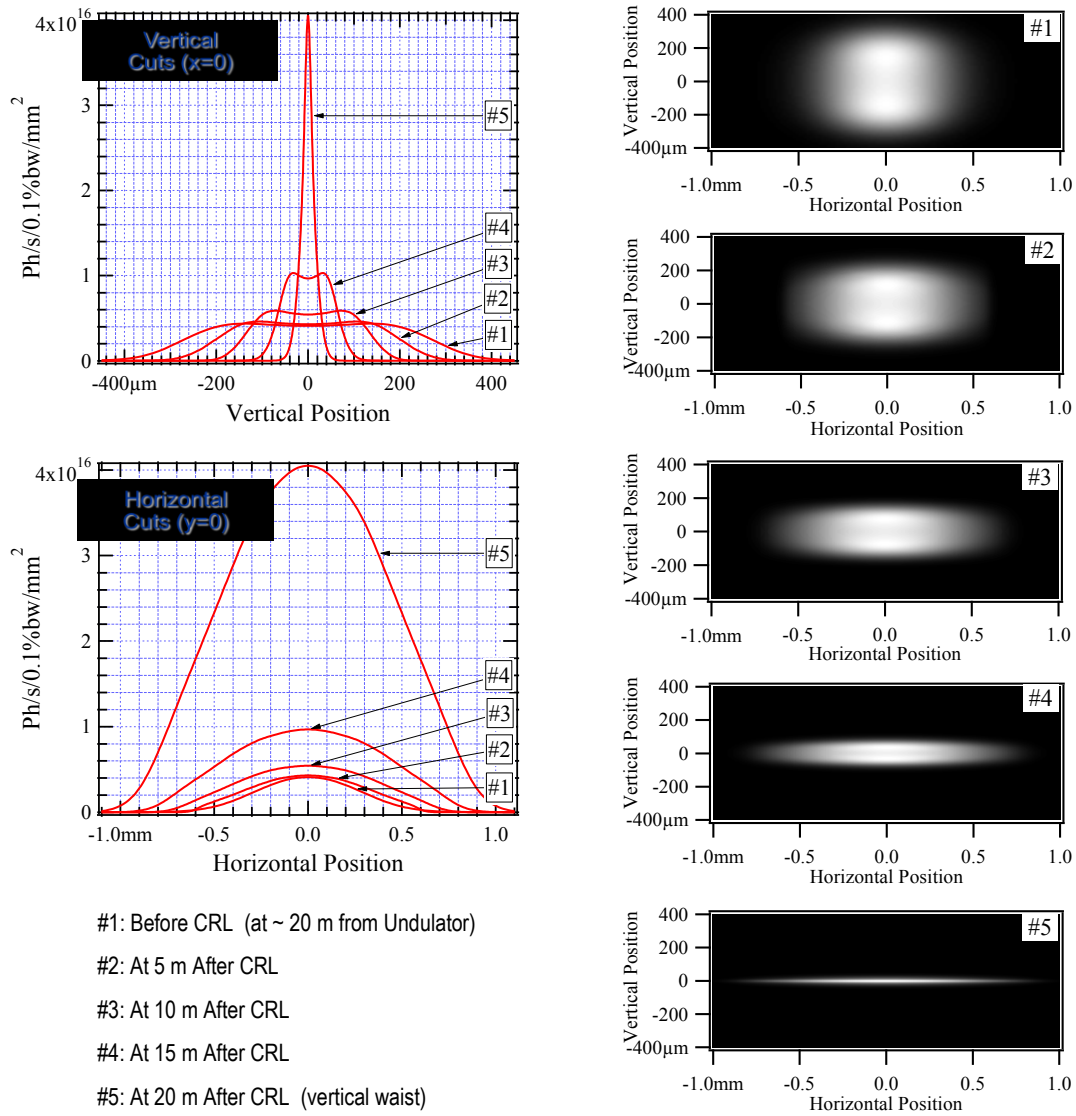


Figure 4-5. Intensity distribution at and after the Be CRLs at different locations as obtained by partially-coherent wavefront propagation simulations along the beamline at photon energy of 9.13 keV, showing the focusing of the vertical source size [16].

The optical design of the IXS beamline relies critically on the performance of these Be CRLs. Since the Be CRLs are placed in the Front-End and exposed to the undulator white beam, severe heatload is expected as shown in Table 4-1. We have carried out thorough heatload analysis and found that a 30 μm thick HOPG (highly oriented pyrolytic graphite) filter provides effective filtering of the undulator heat power with minimum flux penalty. The spectral transmission of the 30 μm thick HOPG at 9.13 keV is more than 98%, yet it removes most of the low energy heat power below 5 keV, covering the first 3 harmonics from the undulator (see Figure 4-6). Table 4-3 summarizes the heatload analysis results using finite-element simulations on the Be CRL with and without the HOPG filter [19]. The simulations assumes the IVU22-6m source with the heat power pre-collimated by a water-cooled collimator (see Figure 3-5) with an end opening of $1 \times 1 \text{ mm}^2$ located at $\sim 19.2 \text{ m}$ from the center of the source. The HOPG filter in the simulation was assumed to be $50 \times 50 \text{ mm}^2$ in size mounted on a copper frame which is water cooled to 25 $^\circ\text{C}$. The absorbed power was 62 W (see Figure 4-7). Clearly from operation safety standpoint, the temperature rise in the HOPG to 440 $^\circ\text{C}$ is well below its safety temperature of 1700 $^\circ\text{C}$, above which significant vaporization has been

observed [20]. The thermal-induced stress level in the Be CRLs under the heatload filtered by the HOPG filter is well within the acceptable level.

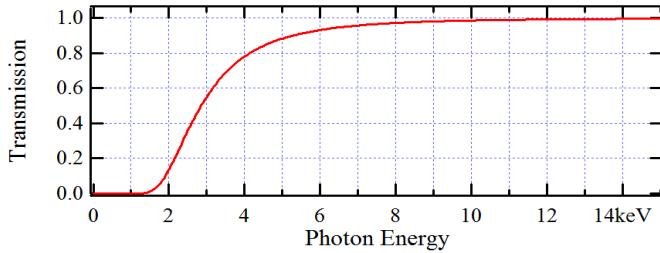


Figure 4-6. Spectral transmission of a 30 μm thick HOPG (highly oriented pyrolytic graphite) filter.

Table 4-3. Heatload on the Be CRL with and without the 30 μm HOPG filter. The power load is pre-collimated through a 1×1 mm² collimator located at ~19.2 m from the center of the undulator source. The FEA simulations are presented in Figure 4-7 and Figure 4-8.

Case	Without HOPG filter	With 30 μm thick HOPG filter
Total Incident Power	225 W	225 W
Absorbed Power	95 W by Be-CRLs	62 W by HOPG 52 W by Be-CRLs ^(*)
Peak Temperature	210 °C in 1 st Be-CRL	440 °C in HOPG 80 °C in 1 st Be-CRL
Total (Elastic and Plastic) Stress	~2%	~0.1%
Fatigue Life Cycles	< 100	> 1,000,000

^(*) There are in total 4 Be CRLs. The absorbed power is distributed among them with ~ 21 W by the 1st, ~13 W by the 2nd, ~10 W by the 3rd and ~8 W by the 4th CRL.

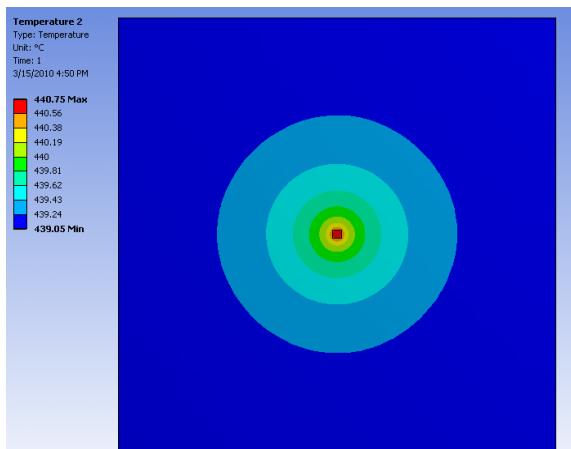


Figure 4-7. Temperature distribution of a 50× 50 mm², 30 μm thick HOPG filter illuminated by a 1×1 mm² IVU22-6m undulator beam. Absorbed power is 62 W. Peak temperature is 440 °C.

The finite-element analysis (FEA) results summarized in Table 4-3 assume direct thermal contact of the Be CRL with a water-cooled copper block maintained at 25°C. Figure 4-8 illustrates the temperature gradient distribution of the Be CRL and the boundary conditions for the simulation. With this cooling geometry, the maximum temperature rises to ~80 °C. Other cooling geometries have also been investigated but all yield higher maximum temperatures.

All these results indicate that the high heatload from the intense undulator beam of the IVU22-6m can be mitigated by introducing HOPG filters before the Be CRLs. For safety redundancy, we are considering using two 30 μm thick HOPG filters. The additional loss of flux is minimal but it will contribute greatly to the safe and reliable operation of the Be CRLs.

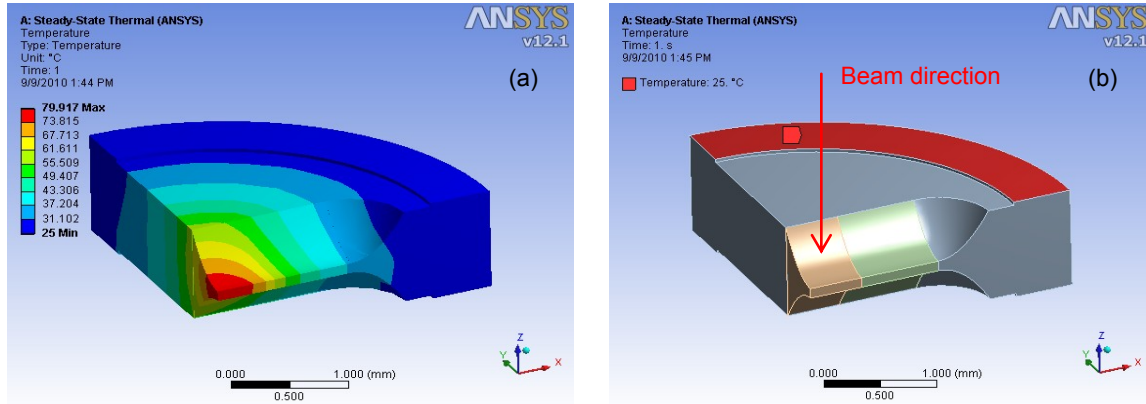


Figure 4-8. Finite-element analysis of the temperature distribution in the Be CRL with a deposited power of ~ 21 W after the 30 μm HOPG filter (a). The simulation assumes that a constant surface temperature of 25 $^{\circ}\text{C}$ is maintained around the ring of the Be CRL (b). The maximum temperature registered is ~ 80 $^{\circ}\text{C}$.

To help with the mechanical design and specifications of the Be CRL assembly in the final design stage, we have also examined a few other issues that may affect the performance of the Be CRLs. These include the optical efficiency under various misalignment conditions, and effects of imperfections (internal defects and external figure errors, etc). The results are summarized in Appendix 4. The conclusion from these evaluations is that contributions due to misalignments and surface roughness of the lenses do not dramatically affect the transmission as long as the respective deviations from the perfect configuration are of the order of 10 μm or less. Optical aberration due to thermal deformation is expected to be small under the present heatload after the HOPG filter. The presence of internal defects of substantial densities may contribute to the loss of intensity and broadening of the focus, and should be avoided as much as possible.

4.2.2 Double Crystal Pre-Monochromator (DCM)

The Double Crystal pre-Monochromator (DCM) will be located at ~ 29.7 m from the center of the undulator source. Its primary function is to remove the heat power from the beam and to provide a stable and pre-monochromatized beam for the high-resolution monochromator further downstream. This is the most important optical component for a stable and performing beamline. We will use cryogenically cooled Si(111) crystals as the technology has become very mature over many years of continuous development. There are several potential vendors providing this type of DCM with proven designs and performance that meet our requirements. We will evaluate existing designs from these vendors and make modifications to suit our needs.

The DCM will be operated primarily at a fixed energy of 9.13 keV, corresponding to the exact backscattering energy of the Si(800) reflection of the CDW/CDDW optics. Some energy tunability is required and would be useful for energy calibration purpose and to provide the flexibility for testing other optical schemes that may require different operation energies. The current choice is 5 – 15 keV, which should cover all foreseeable needs. A pseudo channel-cut crystal arrangement maintaining a fixed beam offset is preferred, which would simplify the mechanical design and alignment of the downstream optical components, and ease the preparation of the diffraction surface of the two crystals.

In order to maintain fixed offset, there are typically two schemes. One is based on a mechanically linked crystal mount, where the fixed exit is ensured by a cam system, and energy scan can be achieved by scanning only the main rotation axis. The other is through independent translation of the two crystals. One elegant way of implementing the

latter scheme is illustrated in Figure 4-9, where the center of rotation (COR) is located at half way of the required beam offset above the first crystal diffraction surface and on the extended line from the diffraction surface of the second crystal. When the Bragg angle is changed, the reflected beam will walk along the surface of the second crystal. Fixed offset can be obtained by a small translation of the first crystal perpendicular to its diffraction surface. Both schemes have been implemented by vendors and are used successfully at synchrotron light sources throughout the world. The solution as shown in Figure 4-9 was used by Kohzu Precision Co. Ltd. in one of their latest DCM models [21]. The crystal parameters shown are preliminary design parameters for the IXS beamline covering the two extreme energies of 5 and 15 keV and for 30 mm beam offset, which is required to meet the Bremsstrahlung shielding requirement¹². Over this energy range, the maximum translation required for the first crystal is only ~1.4 mm.

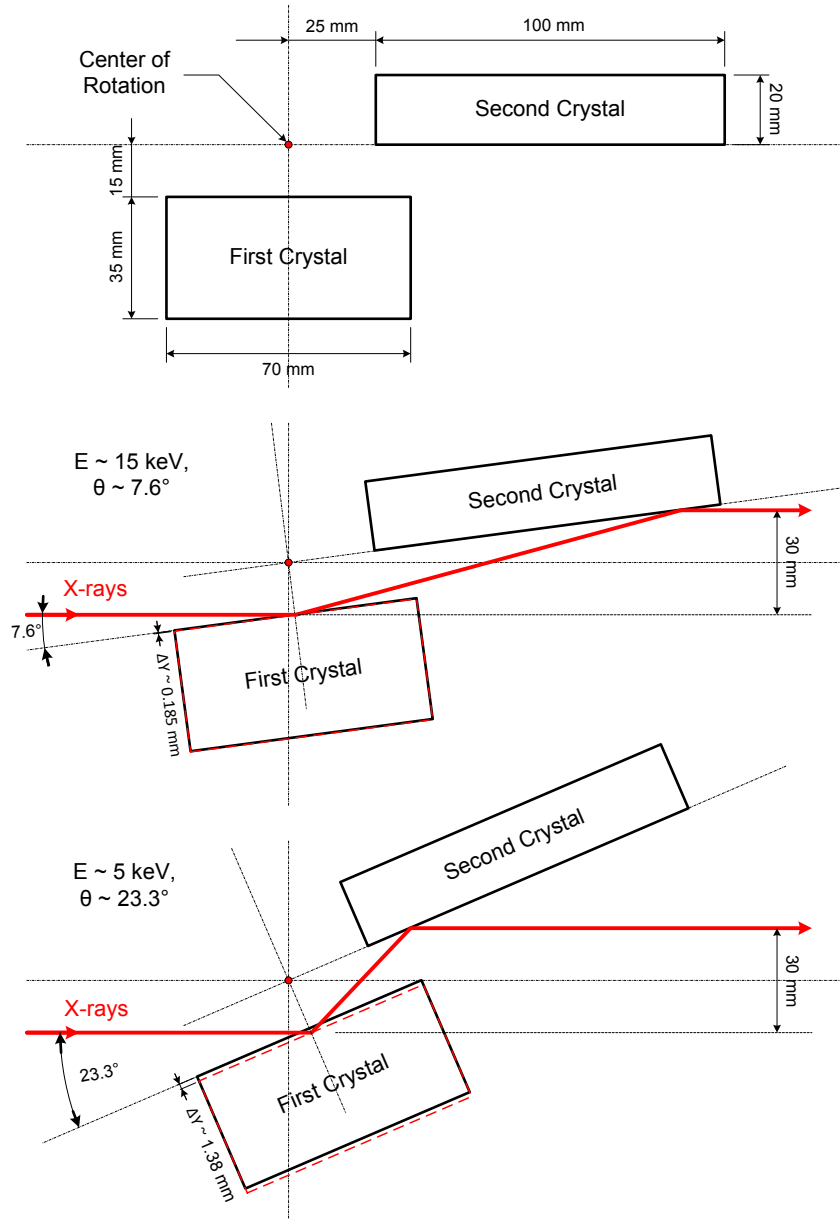


Figure 4-9. Schematic arrangement of the pseudo channel cut Si(111) double crystal monochromator. To maintain fixed offset over the two extreme energies of 5 and 15 keV, the required vertical motion of the first crystal is ~1.4 mm.

This scheme offers the possibility to build a rather compact crystal cage housing the two crystals, and therefore improves stability performance. The minimum required motions of the two crystals for energy tuning and for fixed offset are illustrated in Figure 4-10. In addition to the main rotation axis θ_M and the translation Y of the first crystal perpendicular to the diffraction surface for energy tuning with fixed offset, only three additional motions are needed for achieving and maintaining the parallelism of the two crystals: these are the θ and $\delta\theta$ for the first crystal and the χ for the second crystal. The θ and $\delta\theta$ axes coincide with the main rotation axis, with $\delta\theta$ actuated by a piezo drive for fast feedback control.

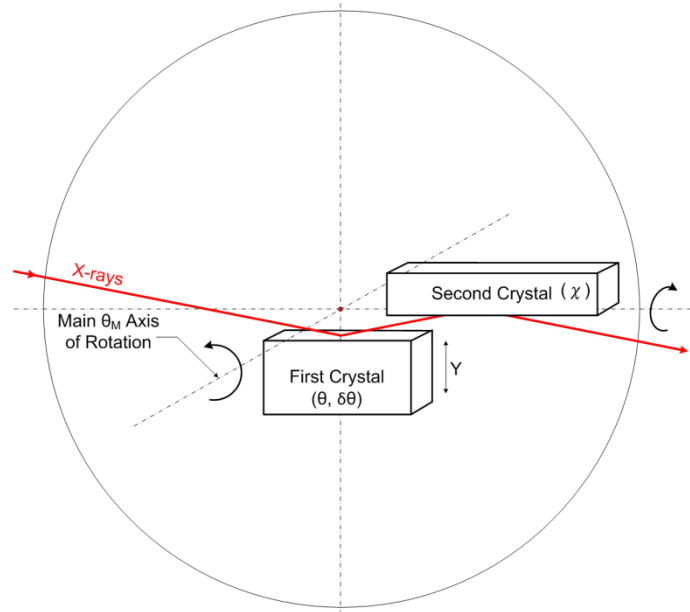


Figure 4-10. Minimum required motions of the two crystals to maintain fixed offset over the scanned energy range are the main axis rotation θ_M and the first crystal translation Y . (θ , $\delta\theta$) for the first crystal and (χ) for the second crystal are for achieving and maintaining the parallelism of the two crystals. ($\delta\theta$) is actuated by piezo drive for fast feedback control.

Table 4-4. Performance parameters of the DCM. The primary operation energy is 9.13 keV, and is the only energy where the DCM will be operated with the Be CRLs in the beam. For other energies, the Be CRLs assembly will be in the by-pass mode.

Energy [keV]	5	9.13	15
Bragg Angle for Si(111) [deg]	23.294	12.505	7.575
Rocking Curve Width FWHM [arcsec]	10.958	6.108	3.684
Rocking Curve Width FWHM [μ rad]	53.126	29.612	17.861
Peak Reflectivity	0.745	0.908	0.964
Relative Energy Resolution $\Delta E/E$	$\sim 2 \times 10^{-4}$		
1st Crystal Size [mm ³]	35 (H) \times 30 (W) \times 70 (L)		
2nd Crystal Size [mm ³]	20 (H) \times 30 (W) \times 100 (L)		
Beam Offset [mm]	30		
COR to 1 st Crystal Diffraction Surface [mm]	15		
COR to 2 nd Crystal Front Surface [mm]	25		

Table 4-5. Motion specifications of the DCM mechanism.

Part	Axis	Motion Range	Resolution	Repeatability	Stability	Actuator
Main Axis	θ_M	5-25 deg	< 1 μ rad	< 2 μ rad	< 2 μ rad	Stepper
1 st Crystal	Y	± 3 mm	< 0.2 μ m	< 0.4 μ m	-	Stepper
	θ	± 2 deg	< 1 μ rad	< 2 μ rad	< 2 μ rad	Stepper
	$\delta\theta$	± 50 μ rad	< 0.1 μ rad	< 0.2 μ rad	< 0.2 μ rad	Piezo
2 nd Crystal	χ	± 2 deg	< 5 μ rad	< 10 μ rad	< 10 μ rad	Stepper
Support Table	X_T	-15/+50 mm	<1 μ m	<1 μ m	-	Stepper
	Y_T	± 50 mm	< 0.2 μ m	< 0.4 μ m	-	Stepper

Based on the above discussion, we summarize the performance and preliminary design parameters of the double crystal pre-monochromator in Table 4-4.

The motion specifications of the mechanism are summarized in Table 4-5. Here the resolution of the angular motions needs to be better than $\sim 1/10$ of the rocking curve width of the Si(111) reflection as shown in Table 4-4. Due to the large angular acceptance of the CDDW optics, requirement on angular stability of the DCM is not strong. Our estimate suggests that a relative angular variation of the incident beam of up to 10 μ rad can be tolerated, which contributes to only $\sim 10\%$ energy variation of the exit beam from the CDDW monochromator with small variation in the throughput. However, if the inline 4-bounce monochromator, which has a lower angular acceptance compared to the CDDW optics, is adopted as the high-resolution monochromator for 1 meV resolution operation, the angular variation could lead to loss of intensity, and therefore would require higher angular stability from the DCM. State-of-the-art DCMs from vendors could achieve an angular stability down to 0.1 μ rad RMS. We therefore do not expect any problem in this aspect. Beam diagnostics will be implemented downstream of the DCM to provide essential monitoring of the intensity, position, and exit angle of the beam.

To ensure that the DCM crystal can handle the heat powers, preliminary finite element analysis (FEA) has been performed on the 1st crystal to quantify the amount of slope error induced by the incident x-rays for the two cases as summarized in Table 4-1 using the following parameters:

- The crystal dimension is 90 mm long, 50 mm wide and 35 mm thick.
- The crystal is located at 29.7 m from the source with the vertical diffraction geometry and an incidence angle of 12.505° , which is the Bragg angle for 9.13 keV.
- The crystal is cryogenically cooled with LN2 at 77K with a side cooling geometry and an effective convection coefficient of $h_{\text{conv}} = 0.003 \text{ W/mm}^2/\text{K}$ representing the effectiveness of thermal contact.

The results are summarized in Figure 4-11. In both cases, a slope error of $< \pm 4 \mu$ rad (PV) was obtained. This is $\sim 25\%$ of the rocking curve FWHM width of Si(111) reflection at 9.13 keV, and therefore is believed to have minimal effect on the performance of the DCM. This is confirmed by Shadow ray tracings.

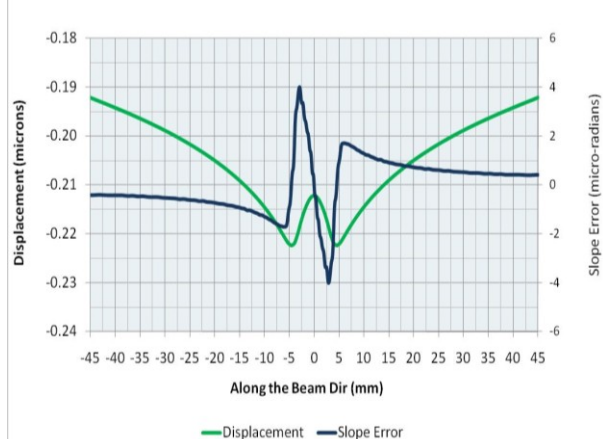
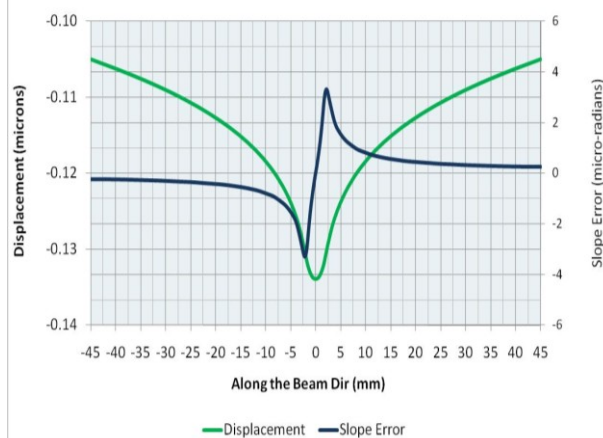
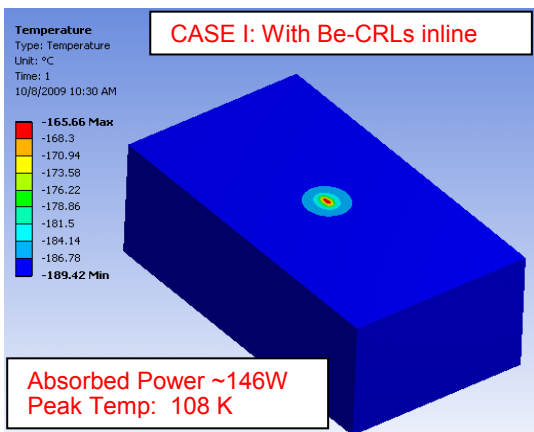


Figure 4-11. Finite element analysis (FEA) of the 1st DCM Si(111) crystal. Case I and Case II are defined in Table 4-1. The left panels show the temperature distribution on the crystal. The right panels show the vertical displacement and slope error induced by the heat load.

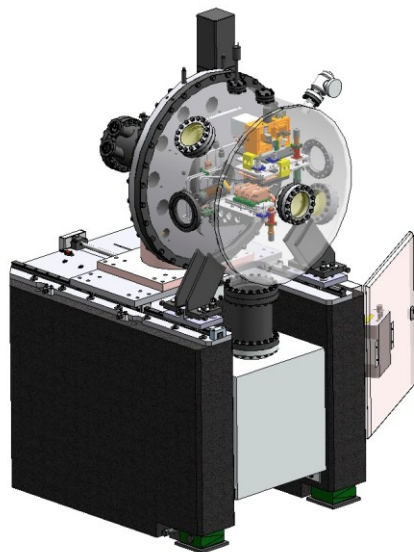


Figure 4-12. Isometric view of a Si(111) DCM (courtesy of FMB-Oxford).

4.3 High Resolution Optics

4.3.1 Status of High-Resolution Optics R&D

The design of the high-resolution optics for achieving the goal of 0.1 meV resolution remains very much on the conceptual level. Due to its R&D nature, it will be developed in house. As stated at the beginning, the design hinges upon the outcome of the high-resolution R&D program being carried out aggressively by the IXS team. Current effort is focused on understanding the working principle of the CDW/CDDW scheme and to address the technical challenges identified in the CDR. So far, most of the R&D work has been performed using a dedicated R&D beamline at the NSLS with a test endstation implementing a CDW monochromator and a CDW analyzer. The setup has allowed us to explore and gain substantial hands-on experience on the challenge related to the optimization of the multi-crystal alignment of the CDW optics. Figure 4-13 illustrates the optical layout and the experimental endstation as implemented on the R&D beamline. Our initial goal is to achieve a total energy resolution of ~1 meV, and upon achieving this initial goal, continuing R&D effort will be pursued to improve the resolution to reach the final goal of 0.1 meV. For this initial experiment, the crystal parameters used are listed in Table 4-6 and have been chosen for 1 meV resolution according to:

$$\frac{\Delta E}{E} \approx \frac{\Delta \theta_e}{2 \tan \varphi} \approx \frac{\theta_e \Delta \theta_e}{2},$$

where $\Delta \theta_e \sim 5 \mu\text{rad}$ is the angular width of the selected dispersion fan by the W crystal and $\varphi \sim 88.2^\circ$ is the asymmetric angle of the D crystal with θ_e (given by $90^\circ - \varphi$) being the glancing incidence angle of the incident beam onto the D crystal.

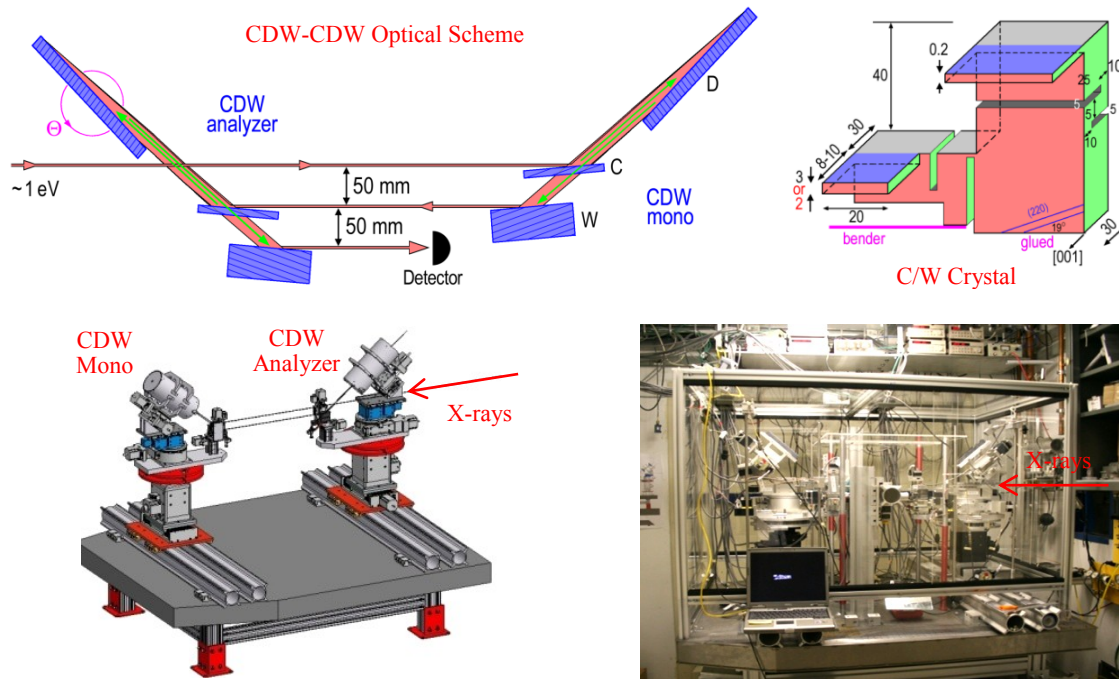


Figure 4-13. The CDW monochromator and CDW analyzer scheme implemented at the R&D beamline at NSLS for testing the CDW optics.

So far, an energy resolution of ~3.7 meV with an estimated efficiency of ~1% has been obtained. This is shown in Figure 4-14 by the rocking curves measured from rocking the D crystal of the CDW monochromator and that of the analyzer. The overall shape of the profiles is consistent with what is expected theoretically. The rocking curve from the CDW monochromator shows a sharp symmetric peak from the front edge of the D crystal and a broad,

asymmetric peak arising from the angular dispersion from the long D crystal surface. The width of the dispersion peak (~103 μrad) and the distance between the sharp peak and the center of dispersion peak (~190 μrad) are consistent with an asymmetry angle φ = 88.2 deg. However, the rocking curve for the CDW analyzer (Figure 4-14, right panel) shows a ~20 μrad broad dispersion peak, which corresponds to an energy width of ~5.3 meV or a deconvoluted resolution of ~3.7 meV for each of the two CDW units. This is much larger than the theoretical energy resolution of 0.74 meV for the monochromator exit beam and a convoluted energy width of 1.05 meV if an identical CDW analyzer is aligned to the monochromator based on the asymmetry angle of 88.2 degree. Further studies are underway to understand what contribute to the broadening of the experimental resolution function and the poorer efficiency. These include lattice inhomogeneities and/or strains, as well as surface imperfections (roughness and slope errors) in the diffraction surfaces of the crystals. For example, optical metrology studies of the diffraction surface of the D crystals used found that the surfaces are far from meeting the specifications listed in Table 4-7. New crystals are being fabricated to improve the surface quality and will be studied systematically. We expect to see improvement in the energy resolution, the resolution tails as well as the optical efficiency with improved crystal quality as the R&D progresses.

Table 4-6. Crystal parameters of the CDW monochromator used in the optics test experiments at NSLS.

Crystal	Reflection	Bragg Angle [deg]	Asym. Angle [deg]	Inc. Angle [deg]	Acceptance [μrad]
C	Si(220)	20.7	19.0	1.7	~110
D	Si(800)	90	88.2	1.8	-
W	Si(220)	20.7	-19.0	39.7	~5.15

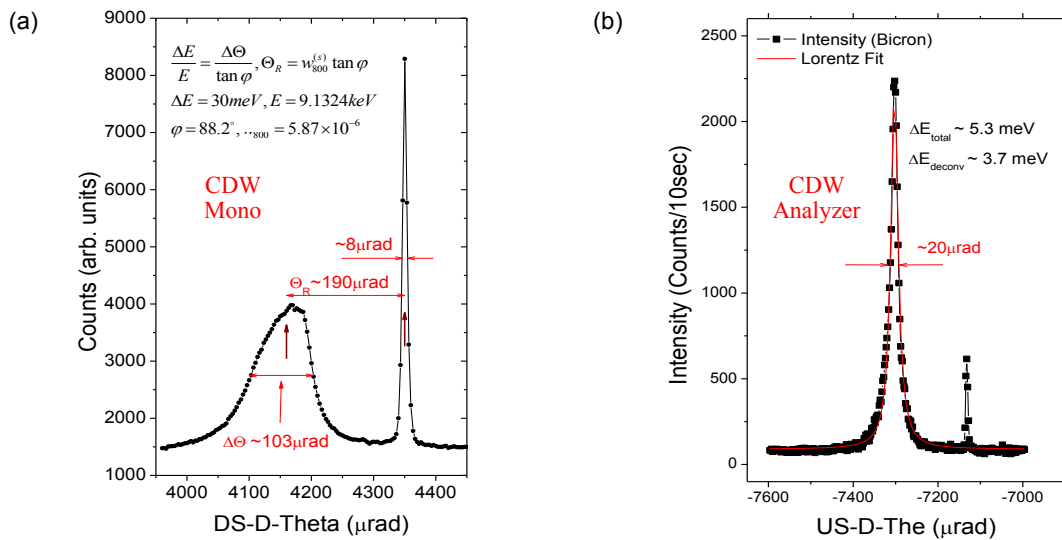


Figure 4-14. D crystal rocking curves measured after the CDW monochromator (a) and after the CDW analyzer with the CDW monochromator set on the maximum of the broad dispersion peak (b).

Table 4-7 lists the technical requirements that the CDW/CDDW schemes must meet in order to achieve the 1 and 0.1 meV resolutions. In the following, we discuss briefly all these requirements and our approaches to address them:

- **Lattice homogeneity**

As mentioned already, this is required by the fact that $\Delta d/d = \Delta E/E$. The lattice homogeneity requirement applies to all the crystals used in the optics. To ensure that this requirement is met, all optical elements should

be fabricated using high resistivity (≥ 10 k Ω /cm) float zone (FZ) single crystals, which are believed to have the least amount of defects and impurities. Their lattice homogeneity will be experimentally determined using comparative diffraction techniques at NSLS. We aim to identify ingots that meet this requirement. It is expected that for the smaller C/W crystal, a suitable crystal can be found. For the D crystal, however, a length of up to 1.8 m is required to accept a vertical beam size of 0.5 mm for 0.1 meV resolution due to the extreme glancing incident angle (0.34°). It is highly unlikely that a crystal of such a length can be found with the required lattice homogeneity. Alternative solutions are needed and discussed later.

Table 4-7. Technical requirements of the CDW/CDDW schemes for 1 and 0.1 meV resolution. The D crystal length was calculated assuming a vertical beam size of 0.5 mm.

Technical Requirements	For $\Delta E = 1$ meV		For $\Delta E = 0.1$ meV	
	CDW	CDDW	CDW ^(*)	CDDW
D crystal glancing incident angle θ_e	1.7°	3.4°	–	0.34°
D crystal length to accept 0.5 mm vertical beam size	360 mm	180 mm	–	1800 mm
Lattice homogeneity ($\Delta d/d$)	$< 10^{-7}$		$< 10^{-8}$	
Temperature uniformity and stability	< 40 mK		< 4 mK	
D crystal surface slope error	< 100 μ rad		< 10 μ rad	
D crystal surface roughness for $> 80\%$ of reflectivity	< 5 nm		< 2 nm	
Lattice distortion & relative angular stability	< 2 μ rad		< 2 μ rad	

^(*) For the CDW scheme to reach 0.1 meV, the required glancing incident angle (0.17°) would be below the critical angle of Si at 9.1 keV ($\sim 0.2^\circ$).

▪ Temperature uniformity and stability

This requirement is due to the thermal expansion of silicon ($\Delta d/d = \alpha \Delta T$, where $\alpha = 2.56 \times 10^{-6}$ K $^{-1}$ for silicon at 300 K). Temperature gradients along the crystal dispersion surface result in local variations of the d -spacing. A 4 mK in temperature gradient corresponds to a lattice variation $\Delta d/d \sim 10^{-8}$ or an energy broadening of ~ 0.1 meV. We have tested temperature control ovens designed for the D crystals, which showed an overall uniformity < 4 mK across a crystal length of ~ 120 mm. Temperature stability of the crystals affects the reflected energy in very much the same way and therefore should be maintained over the course of the experiment, which may take up to 24 hours for one spectrum. The same ovens tested have shown stability better than 4 mK over at least a 20 hours duration. Therefore, at least for 1 meV resolution, we believe that we have addressed adequately the temperature uniformity and stability issue. For 0.1 meV resolution, temperature uniformity and stability as high as 0.4 mK, corresponding to an energy variation of 0.01 meV, would be required, which remains an engineering challenge.

▪ Surface quality (slope error and surface roughness of the D crystal)

Slope error of the D crystal diffraction surface is equivalent to changes of the asymmetry angle of the D crystal and therefore causes energy broadening. Our calculations taking into account the dynamical shift of reflection angle suggest that the slope error should be smaller than 10 μ rad to limit the broadening to less than 0.1 meV. On the other hand, diffuse scattering due to surface roughness reduces the reflectivity of the D reflection and contributes to the resolution tails due to extreme glancing incidence. Modeling based on the distorted wave Born approximation suggests that, in order to achieve 80% reflectivity of a flat surface, its roughness should be less than 2 nm (RMS) for 0.1 meV, whereas for 1 meV resolution, the requirement is 5 nm (RMS) [22]. Surface qualities of sub- μ rad slope error and ~ 0.1 nm surface roughness can be routinely obtained using state-of-the-art polishing techniques on single crystal surfaces. However, obtaining such a surface without leaving damages to the crystallinity of the surface layers remain a nontrivial problem. So far, chemical-mechanical polishing (CMP) is probably the only proven technique that is capable of producing such a surface. We plan to explore the CMP technique coupled with x-ray characterization to produce the required surface finish for the crystals.

▪ **Lattice distortion and relative angular stability**

Lattice distortion can be either related to gravitational sag or induced by mounting strain, both resulting in changes of the θ angle as well as local variation of the lattice homogeneity, and therefore should be avoided. We will pay great attention to designing mounting schemes that minimize these effects through rigorous stress simulations and following known best practices. Another major technical challenge of the CDW/CDDW monochromators and analyzers is about maintaining the angular stability of the D crystal relative to the C/W crystal as this defines the energy stability of the monochromator. This is due to the fact that a rotation of the D crystal relative to the C/W crystal effectively changes the energy of the CDW/CDDW monochromator. The energy tuning rate depends on the energy resolution of the design (i.e., the asymmetry angle of the D crystal). Our calculation shows that a rotation of $\sim 2 \mu\text{rad}$ changes the energy by the same amount as the designed energy resolution. Therefore, unlike all other requirements, the angular stability is largely independent of the energy resolution. Vibration could be a major problem in maintaining such angular stability. In addition to careful engineering design to achieve high stability, we plan to evaluate the effect of vibrations and implement both passive and active vibration control on an as-needed basis to tackle this problem.

• **The length requirement of the D crystal**

Due to the extreme glancing incident angle for 0.1 meV, a D crystal length of up to 1.8 m is required to accept a vertical beam size of $\sim 0.5 \text{ mm}$. This is prohibitively long to meet the other requirements as outlined above for the D crystal. If the D crystal is used for the monochromator, a solution exists where one could combine a CDDW monochromator designed for 1 meV with a channel-cut crystal to further reduce the bandwidth to 0.1 meV, provided that the incident beam divergence is less than $20 \mu\text{rad}^1$. The required D crystal length is 180 mm for an incident beam height of 0.5 mm, and can be reduced further since the vertical beam size for the monochromator is smaller (in fact, the vertical beam size by Shadow ray tracing at the high-resolution monochromator location is $\sim 30 \mu\text{m}$). When the D crystal is used as the analyzer, however, the same approach cannot be applied since the divergence of the scattered photons onto the CDW/CDDW analyzer should be optimized to $\sim 100 \mu\text{rad}$ in order to maximize the efficiency. The CDW/CDDW analyzer must therefore be designed for a specific energy resolution. To solve this problem, we will develop the so-called “comb crystal” to replace the long D crystal in the CDW/CDDW design.

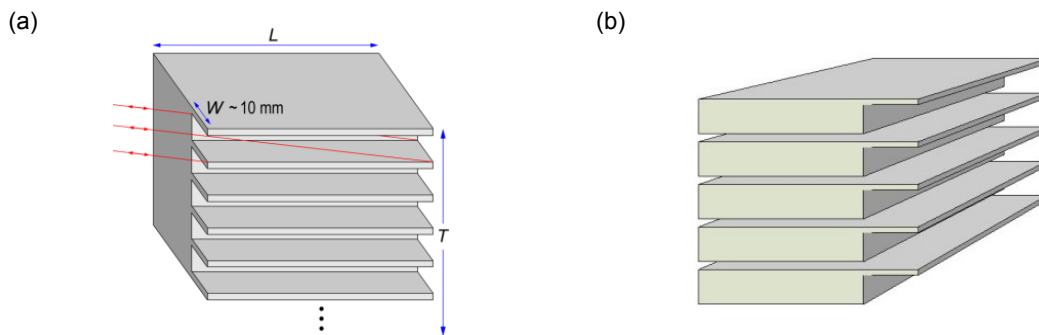


Figure 4-15. Two possible ways of fabricating the comb crystal: (a) as a monolithic block; and (b) as individual segments joined together by mechanical means.

Proposed by Shvyd’ko [23], the idea of the comb crystal is essentially to reduce the physical length of the long D crystal by sectioning it into segments and stacking them together (see Figure 4-15). Here the individual segments have a thickness of a few hundred microns, a width of $\sim 5 - 10 \text{ mm}$ and a length of $\sim 100 - 200 \text{ mm}$. The thickness should be chosen to be greater than the extinction length of Si(800) reflection but minimized to reduce loss of diffracting area. It should be thick enough to provide sufficient strength to withstand the gravity sag. The separation between the segments obviously depends on the glancing incident angle for the desired resolution and should be optimized together with the length of the segment. Clearly, it would be ideal if such

crystals can be fabricated as a monolithic block as proposed, as this helps to maintain the crystalline alignment of the individual segments. There is however considerable technical challenge in doing so due to the difficulty in polishing the diffraction surface inside the grooves to the required level of roughness and slope errors. Another approach would be to first fabricate the segments individually and then combine them together by mechanical means. In this way, the diffraction surface can be prepared by the CMP polishing technique. However, putting them back together afterward with the crystalline planes aligned and maintained becomes an engineering challenge. Both approaches therefore have their pros and cons. The latter approach however seems more amendable. We therefore plan to explore the individual segments approach. For achieving 1 meV resolution, only a few segments will be needed. We note also that in the individual segments approach, the segments can either be stacked vertically to save space and reduce the complexity of temperature control, or they can be laid out horizontally one after the other. The benefits of the horizontal arrangement are that it can conceal the front edge of subsequent segments under the shadow of the previous one, and that the individual segments need not be thin. However, maintaining the temperature uniformity over an extended length to the required level may become a real challenge.

4.3.2 CDW/CDDW Prototype

In order to demonstrate the overall feasibility of the optics, we have designed a prototype system capable of implementing the CDW-CDW or the CDDW-CDDW scheme for ~ 1 meV energy resolution. The objectives of the prototype include: (1) test the CDW / CDDW optics designed for ~ 1 meV resolution, measure the energy resolution and resolution tails, and determine the efficiency; (2) test the multilayer mirror for the angular acceptance, collimation and reflectivity; and (3) determine the total energy resolution function by measuring the elastic scattering from a Plexiglas sample using the two CDW or CDDW units, one as the monochromator and the other as the analyzer in conjunction with the multilayer mirror, and perform energy calibration by measuring the phonon spectrum over a limited Q range from a well-known sample (e.g., diamond).

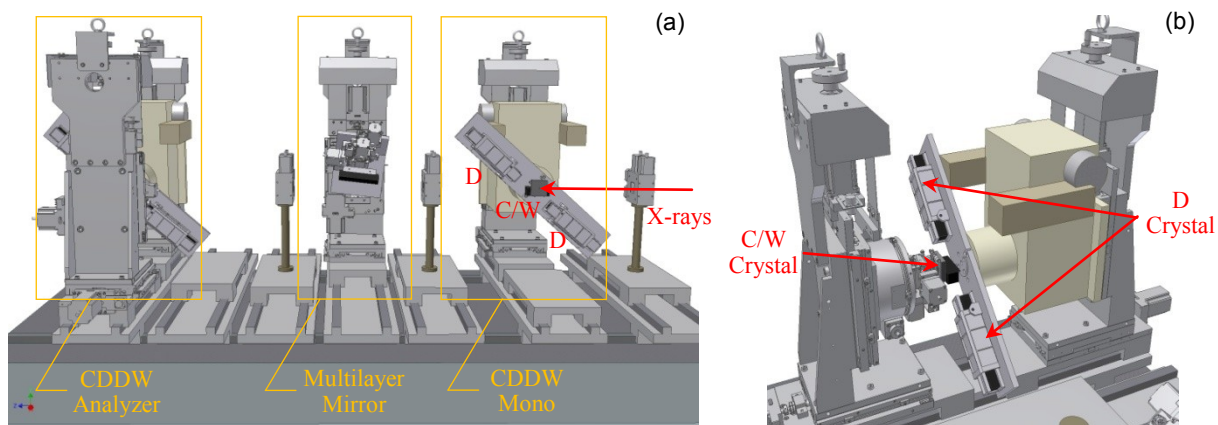


Figure 4-16. Overview of the CDDW-CDDW prototype including the multilayer mirror (a), and a close-up of the CDDW crystal arrangement in the monochromator/analyzer design (right).

Figure 4-16 provides an overview of this system implementing the CDDW-CDDW scheme. The design is based on the so-called Ishikawa system [24], a versatile precision diffractometer assembly with now commercially available high-precision goniometers, which has been adopted widely at SPring-8 and APS for ultrahigh resolution X-ray optics positioning and control. The key components are the high-precision dual-axial goniometers from Kohzu with an angular resolution of $0.025 \mu\text{rad}$ over an angular range of $\pm 2.5^\circ$, which are used for the positioning of the D crystals in the optical scheme. The C/W crystal will be mounted on an independent goniometer and aligned to the same rotation axis. Temperature control will be implemented for the D crystals in order to obtain the temperature uniformity and stability required for sub 1-meV resolution. The system includes two CDDW units of the same configuration to facilitate energy resolution measurements by diffraction, in which the first CDDW unit is aligned

to the incident X-ray beam from the beamline as the monochromator, whereas the second CDDW unit is aligned to the first one to determine the convoluted energy resolution.

Further developments of the system are anticipated depending on the experience gained from the current R&D activities of the IXS team. The above prototype system is highly flexible and reconfigurable, and would become the backbone for such developments. For example, in order to maintain the angular alignment of the CDW/CDDW crystals, we plan to implement the flexure wheels invented by Deming Shu at the APS to create a pseudo channel cut monochromator involving all three crystals in one assembly. This is illustrated in Figure 4-17, where the C crystal is affixed at the center of rotation of the high-precision goniometer, whereas the D and W crystals are each mounted on a flexure wheel, allowing precise angular motion and control of the crystals in the dispersion plane. It can be further expanded to include multiple D crystals in a comb-like assembly which ultimately can be developed into an analyzer unit for the 1 meV resolution operation.

This prototype system will become part of the optics test bench in Hutch C for the IXS beamline.

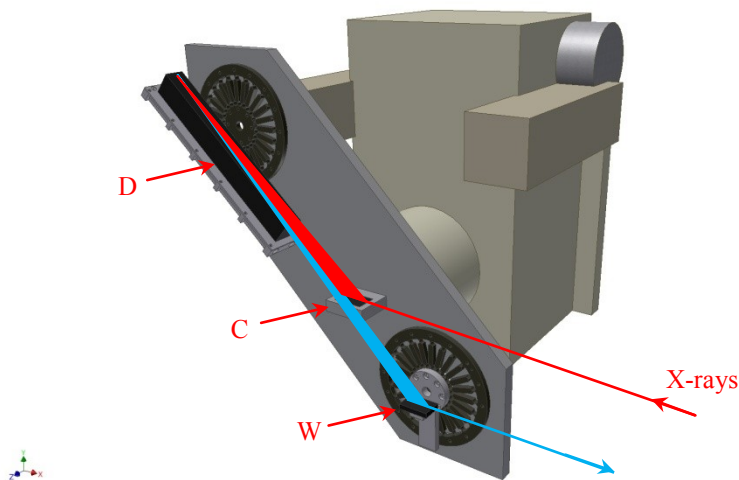


Figure 4-17. Conceptual layout of a pseudo channel-cut arrangement for the CDW scheme mounted on a high-precision goniometer.

4.3.3 Alternative Optical Schemes

As discussed in the CDR, the CDW/CDDW monochromators are chosen for the IXS beamline because of their novel design that gives a *large angular acceptance and the potential to lead us to the ultimate resolution of 0.1 meV at a moderate energy of ~10 keV*. For this reason, they remain at present the focus of our R&D effort. However, there are considerable technical challenges as we have presented in the previous sections. In order to ensure that a workable, best in class user instrument can be ready on day one of NSLS-II operation, a number of alternative monochromator designs have been considered. In choosing an alternative design, our main considerations include (1) the practically achievable energy resolution, (2) the angular acceptance or compatibility to be used as analyzer optics, and (3) compatibility with the current beamline design. Among the alternatives we have examined, the inline 4-bounce scheme designed by Yabashi et al [25] and Toellner et al [26] is the most applicable. The monochromator designed and built by Toellner and Su et al (Figure 4-18) in particular was proven to deliver 1 meV resolution at the ^{83}Kr nuclear resonant energy at 9.403 keV with an overall efficiency of 36% using four Si(800) reflections.

For our purpose, it would be convenient if the 4-bounce monochromator is designed to operate at the same energy as the CDW/CDDW optics. This ensures full compatibility with the CDW/CDDW optics and allows the possibility of combining the 4-bounce monochromator with analyzer optics built based on the CDW/CDDW scheme. Figure 4-19 presents one such design using four Si(642) reflections with asymmetric factor of -1/12, -1/10, 12, and 10. The angular acceptance as designed is 30 μrad . The vertical beam size acceptance is 0.5 mm. The theoretical peak

reflectivity is 43.6%. This design is therefore quite suitable for the high-resolution monochromator for the beamline for 1 meV resolution operation. To increase the angular acceptance, it is necessary to increase the asymmetric factor of the 1st and 4th crystal, which will sharply reduce the efficiency and at the same time require longer 2nd and 3rd crystals.

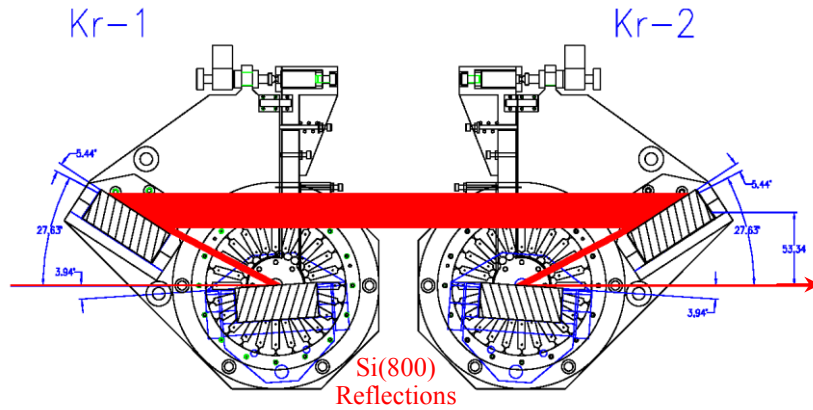


Figure 4-18. The Kr monochromator designed and built by Toellner and Su et al²⁶, delivering 1 meV resolution at the ⁸³Kr nuclear resonant energy at 9.403 keV with an overall efficiency of 36%. Note that the relative angular motions of the crystals are implemented by two flexure wheels in a pseudo channel cut arrangement supported by high-precision goniometers (courtesy of T. Toellner).

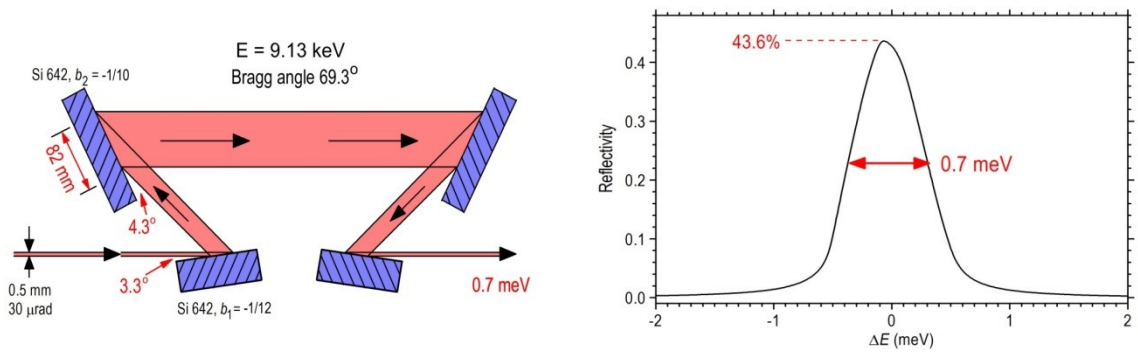


Figure 4-19. A 4-bounce monochromator design for 0.7 meV resolution at 9.13 keV using Si(642) reflections with asymmetry factor of -1/12, -1/10, 12, and 10. The angular acceptance is 30 μ rad. Vertical beam size acceptance is 0.5 mm. The theoretical peak reflectivity is 43.6%.

4.3.4 Other Design Considerations

The high-resolution monochromator will be located at ~37 m from the center of the undulator source. This location was chosen in order to position (essentially the C crystal of) the CDDW monochromator ~200 mm downstream of the vertical waist of the Be CRLs, which is located at 26.776 m from the center of the undulator source. This provides an effective mean to reduce the source size broadening due to the large angular divergence of the exit beam as discussed in the CDR. In practice, the focus of the Be CRLs acts as a virtual source in the vertical for the CDDW monochromator. A four-blade slit will be included as part of the high-resolution monochromator system to define this virtual source. The focal size of the Be CRLs after the DCM from the Shadow ray tracings studies is 886 (H) \times 29.5 (V) μ m² FWHM. A slit opening of ~2.25 (H) \times 0.075 (V) mm², corresponding to 6 σ of the beam size, would allow the full beam through. The horizontal opening of the slit offers a very effective means of controlling

the final horizontal divergence of the beam onto the sample and can be used to improve the Q resolution of the incident beam at the expense of the incident flux (a factor of 2 improvements in horizontal divergence results in a factor of 2 losses in flux). On the other hand, the vertical opening will not be effective in controlling the final vertical divergence of the beam onto the sample but can be used to reduce the beam focus on the sample.

The HRM will be placed in vacuum in order to minimize air absorption loss, and to provide a better environment for implementing temperature control of the crystals. The vacuum chamber will be large enough to accommodate two high-precision goniometers allowing the implementation of the inline 4-bounce monochromator, although the CDDW optics requires in principle only one such goniometer. This is schematically illustrated in Figure 4-20.

We plan to implement the channel-cut monochromator, which is required for the 0.1 meV resolution operation, and the phase plate, which is used to rotate the polarization to the vertical plane, in a similar fashion; both are in the mature scope. They will be housed in a separate vacuum chamber downstream of the HRM. In order to ensure stable operation of the optics and their relative alignment, the two vacuum chambers will be supported by a common granite block (see Figure 4-2).

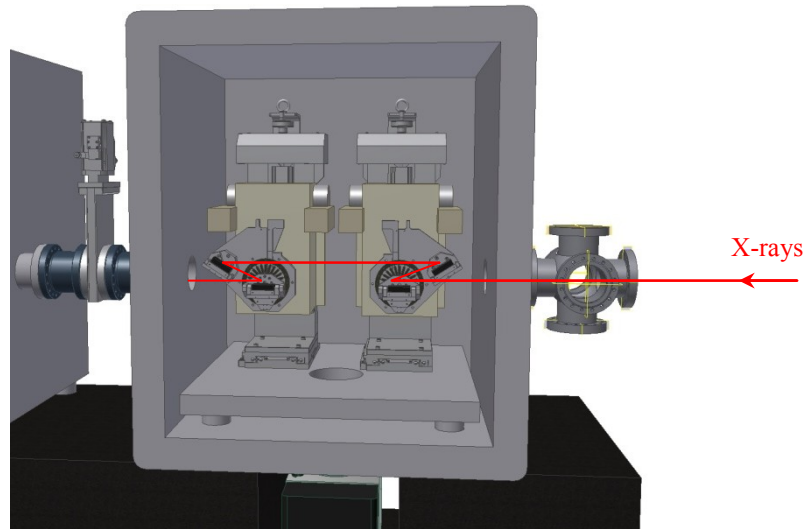


Figure 4-20. Conceptual layout of the HRM showing the in-line 4-bounce monochromator setup on two high-precision goniometers. For the CDDW scheme, only one goniometer would be needed.

4.4 Focusing Optics

There are two sets of focusing mirrors in the optical design of the beamline, both of which will be implemented in the K-B configuration. One set in the baseline scope is designed to provide fine focusing at medium Q resolution ($\sim 0.1 \text{ nm}^{-1}$). The essential goal is to produce a beam focus on the sample to be less than $\sim 10(H) \times 5(V) \mu\text{m}^2$. The other set in the mature scope is for obtaining high Q resolution and therefore necessarily with weaker focusing. The required Q resolution is $\sim 0.01 \text{ nm}^{-1}$ at low-Q. Considering only the horizontal scattering plane, the total Q resolution is given approximately by the sum of the incident beam divergence onto the sample and the horizontal angular acceptance of the analyzer optics as discussed in the CDR [1]. A 0.01 nm^{-1} Q resolution therefore limits the horizontal divergence of the focused beam onto the sample to be less than or $\sim 0.2 \text{ mrad}$. Similar argument applies also in the vertical. Table 4-8 summarizes the current locations of these mirrors on the beamline and their demagnification factors in order to meet these requirements of the beam.

On the other hand, the choice of mirror material and the incidence angle are generally dictated by the critical angle of the materials and the energy range to be covered by the mirrors (e.g., for harmonic rejection). A larger incidence angle is favorable for reducing the length of the mirrors and improving harmonic rejection with lower cut-off

energy, but the reflectivity of the mirrors decreases. We have considered bare Si, Silica (SiO₂, less expensive option and good alternative to Si for monochromatic beams) and Pt, Pd and Rh coatings and concluded that Rh coating on a Si substrate is the most suitable choice for the present beamline. In Figure 4-21, we compare the critical angle $\alpha_c = \sqrt{2\delta}$ as a function of the incidence energy for Si, SiO₂, Rh and Pt. Here, most mirror suppliers will guarantee densities of Rh in the coatings to be better than 90% of the bulk material which is 12.41 g/cm³. The calculations therefore assume a density of Rh of 11.17 g/cm³. The densities are usually lower, about 85% of the bulk, for bimorph mirrors. The double curves for Rh and Pt represents the two densities considered.

Table 4-8. The location of the two sets of K-B mirrors and their corresponding source and focus position.

K-B Mirror Set		Source Location [m]	Mirror Location [m]	Focus Location [m]	Demag. Factor
A: High Q Resolution Weak Focusing (Mature Scope)	VFM	36.776	48.500	58.000	~1.2
	HFM	0	49.373	58.000	~5.7
B: Low Q Resolution Strong Focusing (Baseline Scope)	VFM	36.776	55.825	58.000	~8.8
	HFM	0	56.953	58.000	~54.4

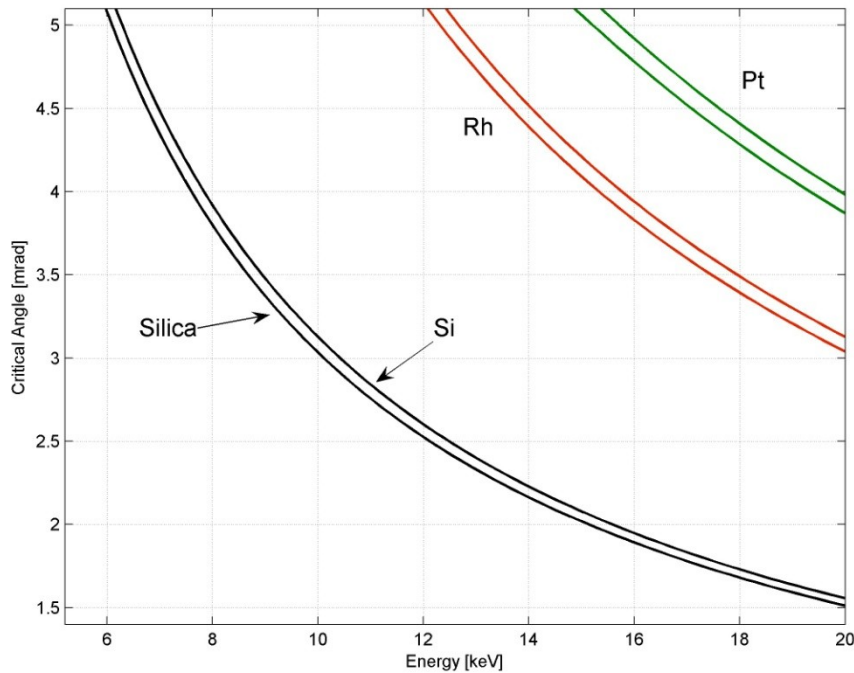


Figure 4-21. Variation of the critical angle versus energy for bare Silica, Silicon, Rhodium and Platinum. The double lines for Rh and Pt correspond to different densities of the materials: 85% density of the bulk for the lower line and 90% for the upper line.

We choose Rh coating with an incidence angle of 3.5 mrad in order to cover the energy range of 5 – 15 keV and to limit the length of the mirrors to 1 m or shorter. If we limit the operation to only around 9.13 keV and below, bare Si mirrors with an incidence angle of 3.0 mrad would also be acceptable. However, the required length for the vertical mirror in the baseline scope (low Q resolution / strong focusing) will need to be 1.2 m long due to the large

angular divergence of the beam after the CDDW HRM. The reflectivity for Rh coating with 3.5 mrad incidence angle is only a few percent lower than Si at 3.0 mrad incidence angle (see Figure 4-22).

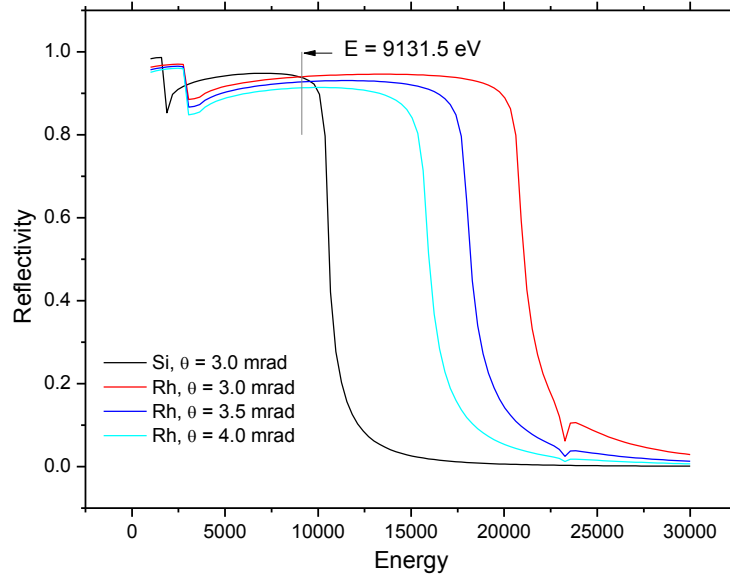


Figure 4-22. Reflectivity curves of Si and Rh at various incidence angles. The Rh reflectivity was calculated assuming 90% of the bulk density at 11.17 g/cm³.

The shape of the mirrors will be plane ellipse. Table 4-9 summarizes the mirror parameters defining the elliptical shape of the two sets of mirrors. Here, s_1 and s_2 are the source-mirror and mirror-focus distance, respectively; a and b are the semi major and minor axis of the ellipse; and c is the semi focal length. The beam footprint defined by 4σ of the illuminated area as obtained from the Shadow ray tracings and the mirror size are also listed.

Table 4-9. Parameters of the two sets of K-B mirrors with plane ellipse figure. s_1 and s_2 are the source-mirror and mirror-focus distance; a and b are the semi major and minor axis of the ellipse; c is the semi focal length. All mirrors are silicon mirrors with Rh coating, and use an incidence angle of 3.5 mrad. The footprints are illuminated area on mirrors defined by 4σ of the beam size.

K-B Mirror Set	s_1 [m]	s_2 [m]	a [m]	b [m]	c [m]	Footprint 4σ [mm ²]	Mirror Size [mm ²]
A VFM	11.724	9.500	10.611933	0.036937	10.611869	1.9(W) × 580(L)	50(W) × 640(V)
A HFM	49.373	8.627	29.000000	0.072234	28.999910	1.9(W) × 540(L)	50(W) × 600(V)
B VFM	19.049	2.175	10.611933	0.022528	10.611909	2.4(W) × 940(L)	50(W) × 1000(L)
B HFM	56.953	1.047	29.000000	0.027027	28.999987	1.5(W) × 780(L)	50(W) × 840(L)

Due to the strong bending, particularly for the HFM and VFM of the second (B) set of K-B mirror, we plan to use bimorph with pre-figured mirror substrates to produce the required ellipse shape. The strong demagnification factors of this set of mirrors also mean that the focus will be less sensitive to slope errors. The beam focus and divergence on the sample as obtained by Shadow ray tracings are shown in Figure 4-24 and the results are summarized in Table 4-10. A slope error of up to 0.5 μ rad RMS is acceptable, which broadens the focus by ~20%. For the first (A) set of K-B mirror, due to the intrinsically larger focus with the weaker demagnification, pre-figured mirrors with slope error of up to 0.5 μ rad are acceptable.

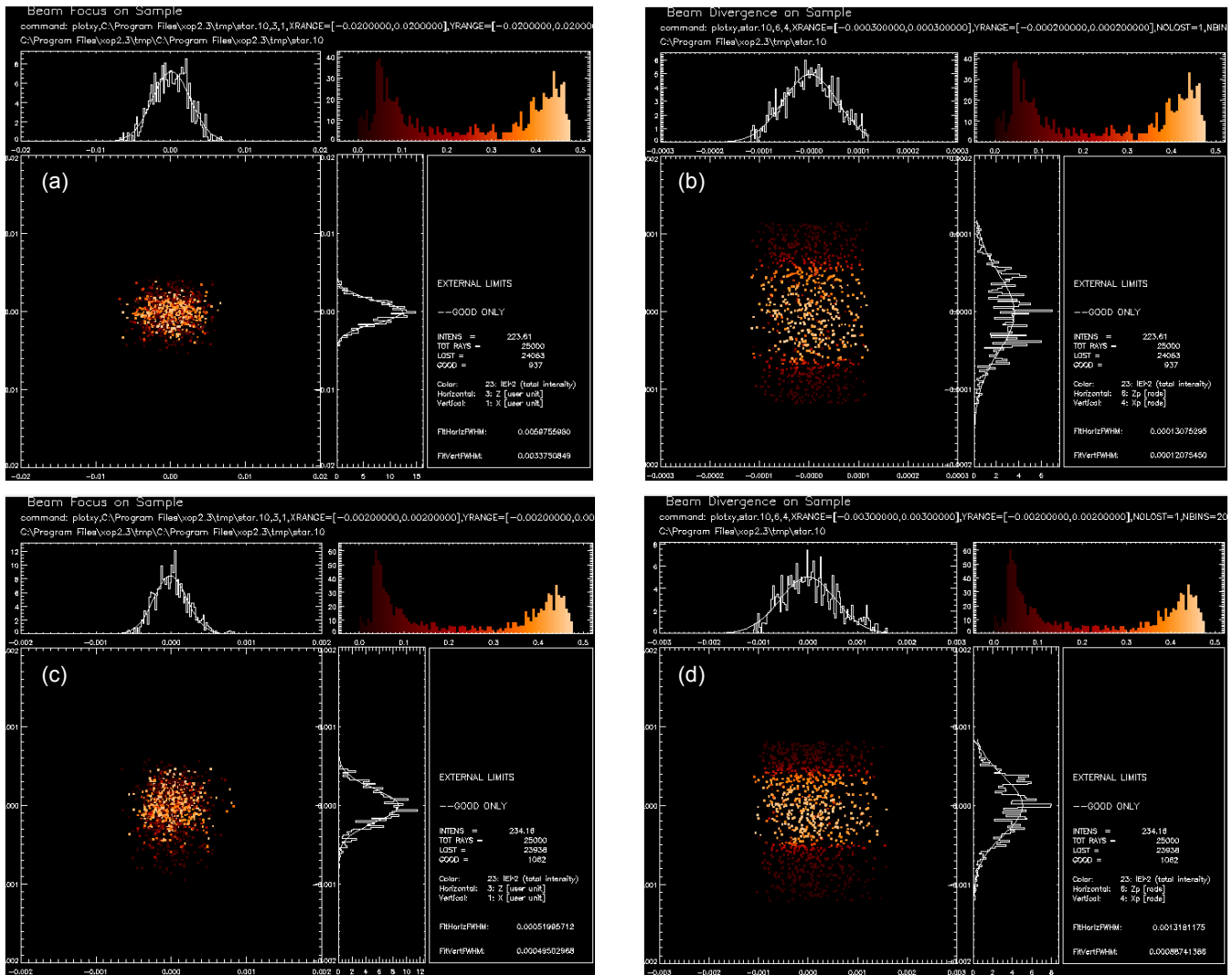


Figure 4-23. Shadow ray tracings results of the two sets of mirrors. The tracings include all optical elements of the beamline from the Be CRLs, DCM, and the CDDW HRM. The heat load in Case I of Table 4-1 was included in the tracings. (a) Focus and (b) divergence of the beam on sample of K-B Mirror Set A; (c) focus and (b) divergence of the beam on sample of K-B Mirror set B.

Table 4-10. Beam size and divergence on sample obtained by Shadow ray tracing. DCM heat load bump due to the heat load in Case I of Table 4-1 was included in the tracings. Mirror slope error was not included.

K-B Mirror Set	Beam Size (H) × (V) [μm^2] FWHM	Beam Divergence (H) × (V) [mrad^2] FWHM
A	59.8 × 33.8	0.131 × 0.121
B	5.20 × 4.95	1.319 × 0.887

The mirrors perform as expected based on these Shadow ray tracings results. The final beam divergence for the mirrors in the mature scope (A set) and the beam focus for the mirrors in the baseline scope (B set) meet design specifications.

Bimorph mirrors of similar lengths to the second (B) set of K-B mirrors in Table 4-9 are available commercially. Figure 4-24 shows one such K-B mirror system produced by ACCEL Instruments GmbH [27]. The HFM is 1050

mm long, and the VFM 600 mm with the total length of the mirror chamber at 2100 mm. The alignment and control system of our K-B mirrors is expected to be similar.

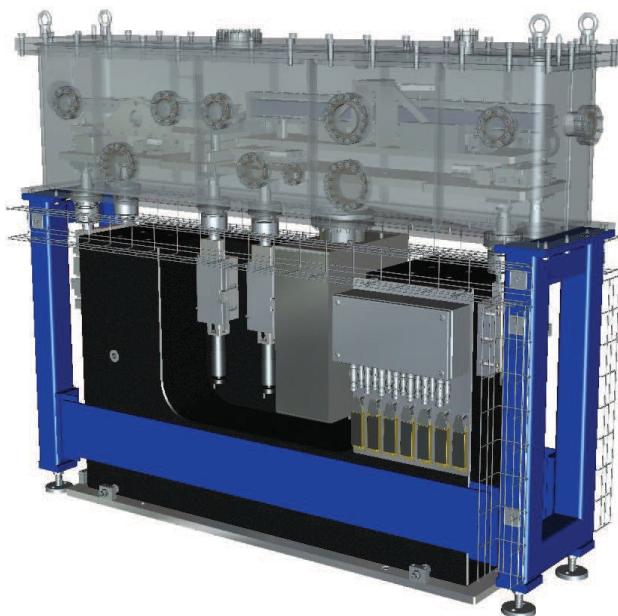


Figure 4-24. 3D model of a bimorph K-B mirror system from ACCEL Instruments GmbH.

4.5 Beam Transport

4.5.1 Beamline Vacuum System

The IXS beamline is divided for vacuum purposes into 8 vacuum sections, plus sample environment and spectrometer. Each section is pumped by ion pumps and monitored with dual up-to-air and UHV vacuum gauges, and isolated by gate valves. We refer to the beamline drawing and controls layout included in Appendix 2 for relative locations of the components described here.

Section 1 contains white beam diagnostics and the fixed mask in Hutch A. Due to the limited conductance of this aperture, pumping and gauges are provided on both upstream and downstream ends. Since the beamline is intended for windowless operation, the small conductance of the fixed mask in this section allows for differential pumping separating the beamline vacuum from that of the Front End.

Section 2 contains the double-crystal monochromator, including pump and gauges.

Section 3 includes white beam and Bremsstrahlung beam stops after the monochromator, diagnostics, monochromatic beam slits, a 2 meter section of unoccupied beam pipe, and the photon shutter. Although the beam stops are not expected to significantly limit pumping conductance, the photon shutter is. For this reason two pump / gauge instances are included in this section. The photon shutter is the last (most downstream) element in Hutch A, and Hutch B starts with the ion pump followed by a gate valve (on a common stand).

Section 4 includes a diagnostics cross and the high-resolution monochromator in Hutch B.

Section 5 includes the channel-cut monochromator in Hutch B, the phase plate, diagnostics cross, and a photon shutter. As with section 3, the photon shutter is pumped (and gauged) on both upstream (CCM/PP) and downstream (PS) side. A roughly 8 m length of pipe transports the beam in this section between the photon shutter and downstream pump and gate valve. This gate valve is expected to be fitted with a beryllium window in order to

deliver x-rays to experiments to be performed in air in the downstream Hutch C (valve is used as a window in the closed position).

Section 6 defines a removable ~ 3 m length of pipe which passes above an optics table in Hutch C. When operated in vacuum, this section is pumped and gauged at the downstream end.

Section 7 includes a photon shutter and transport pipe from Hutch C into the experimental hutch (D). In the mature scope this section will also include a mirror tank in Hutch C.

Section 8 includes the focusing mirror tank just upstream of the sample in Hutch D and terminates with a beryllium window.

The sample environment will vary and will be discussed in Section 5.2.

The analyzer arm(s), including the collimating mirror, the analyzer optics and the spectrometer flight path, will be pumped separately from the beamline to HV/UHV vacuum levels for maximum cleanliness and x-ray transmission.

Two sets of fast valves and sensors are provided. The upstream sensor located in section 1 will be part of the control for a fast valve located in the front end. The downstream sensor located in section 8 will be part of the control for a fast valve located in section 4 (the most upstream monochromatic hutch location).

4.5.2 Beam Diagnostics

Beam diagnostics for the beamline serves two main purposes: (1) for commissioning and alignment of individual components, and (2) for monitoring their operation and performance. In some cases, these diagnostics will also provide feedback control. Each optical component of the IXS beamline has a specific diagnostic location for one or both of the above purposes. In some cases, the precise form of diagnostics is not yet fully decided, although there are several possible feasible choices. Refer to the beamline controls layout drawing (Appendix drawing A2-15) for more detail of the components described here.

Diagnostics for the Be CRLs and the white beam slits (of the Front End) will be carried out at the location of the dedicated diagnostics ports in vacuum section 1. On the stand which holds the fixed mask and collimator, and upstream of these elements, is a vacuum cross which can carry a white beam diagnostic such as diamond transmission BPM, or some screen/camera arrangement. In addition, several white beam ports are available between this stand and the DCM in the same section; slits can also be mounted at this location. Installation of second transmission monitor can be used at this location to provide white beam angle information. Since the CRL focus is expected to be near the upstream (input) end of the high-resolution monochromator, a diagnostic port is made available there as well. In that case, the diagnostic is likely to be a screen and camera, but slits and point sensor could also be used to measure the beam profile at this position. In the optical design, a set of slits will be installed at the focal position of the CRL to define the vertical secondary source for the high-resolution monochromator.

Diagnostics of the monochromatic beam (from the DCM) is expected mostly to be carried out by intensity monitor(s) located in section 3 (just downstream of the DCM). The fine pitch control of the second crystal can be utilized in closed-loop fashion for feedback control using a transmission or foil type monitor. Slits are also available at this location and can be used both for diagnostics and beam conditioning.

Diagnostics for the HRM are part of the optics R&D effort, and will likely include several intensity monitors which can be inserted and removed from the beam path.

Diagnostics for the CCM and PP will be installed onto the diagnostics cross located just downstream of that common chamber.

Alignment of the focusing mirrors can be done at the sample position using slits and diagnostics available there.

Sample-dedicated diagnostics include high-bandwidth telescope cameras, intensity monitors, attenuators, and slits.

Diagnostics for critical components include cooling water temperature and flow meters for CRL, fixed mask, DCM, and white beam x-ray diagnostics. In addition, temperature monitors for the cryogenic cooled DCM as well as temperature controllers for the HRM and IXS analyzer optics and detector will be available for diagnostics.

Ambient diagnostics will also be made available in the form of hutch temperature sensors (one-wire monitors), ambient lighting control (on/off/dim), and hutch cameras (pan/tilt/zoom). Vacuum levels, floor and tunnel temperatures, and accelerator parameters (such as ring current) will also be collected under the controls scope for this beamline (see Section 6.4).

4.6 Other Major Components

The other major components in the beamline are the white-beam fixed-mask and stop, the monochromatic shutters, the monochromatic slits, and the diagnostic/pumping crosses.

4.6.1 White-Beam Fixed Mask and White-Beam Stop

The fixed mask and beam stop are located in the FOE. The fixed mask is one of the first components in the beamline. Its purpose is to prevent the FOE Bremsstrahlung Collimator from being struck by the X-ray beam. The fixed mask and its support stand are essentially duplicates of the IXS front end assembly (see Figure 4-25).

The white-beam stop will be located just downstream of the DCM. Its purpose is to stop the portion of the direct beam which is not diverted by the DCM, and in particular preventing it from striking the Bremsstrahlung stop. The stop will be of similar design to the fixed masks and the FE white-beam shutters. The stand will be similar in design to the fixed-mask stand (see Figure 4-26).

4.6.2 Monochromatic Shutters

The monochromatic shutters will be of NSLS2 standard design (see Figure 4-27). These are a Tungsten dual-shutter design. They are un-cooled, and are actuated by compressed air. The shutters in Hutches A and B will be unmodified from the standard design. The shutter in Hutch C will need to be modified to increase the aperture size to accommodate the beam position change from the insertion or removal of the KB mirrors located in Hutch C.

4.6.3 Monochromatic Slits

There will be several sets of monochromatic slits. The first set of slits is located in the FOE downstream of the DCM. It will be used to define the size of the monochromatic beam as it exits the FOE. This set of slits will be a commercially available unit with four independently controlled blades.

There will be a set of monochromatic slits located at the focal-point of the Be CRLs. This focal-point is just upstream of the HRM in Hutch B. This set of slits will be used to define the secondary-source size for the HRM. It is expected that this set of slits will be in-vacuum within the HRM chamber. It will be a commercially available in-vacuum design with four independently controlled blades.

There will be a set of monochromatic slits at the upstream end of each KB mirror set. These will be located within the mirror chamber. They will be used during commissioning and diagnostics of the (bimorph) mirrors, providing a means to scan the beam along the length of the mirrors for tuning the focus and figure. These slits will be of the scanable-gap design, providing a stable gap size which can then be scanned horizontally or vertically as needed. They also provide an effective mean to control the final beam divergence onto the sample, and can be used to improve the Q resolution of the incident beam if required.

4.6.4 Diagnostics and Pumping Cross

The pumping of the vacuum transport line will be done by ion pumps. These pumps will be incorporated into an assembly of stand, pump, and six-way cross with additional pump-out valve and gage ports (see Figure 4-28). These pumping assemblies will be used in six locations along the beamline. There will be one additional location in the FOE without a pump, and one location in Hutch D which will require a larger flange size cross.

The many flanges and ports provided by these crosses will provide locations for the diagnostic tools anticipated for the beamline.

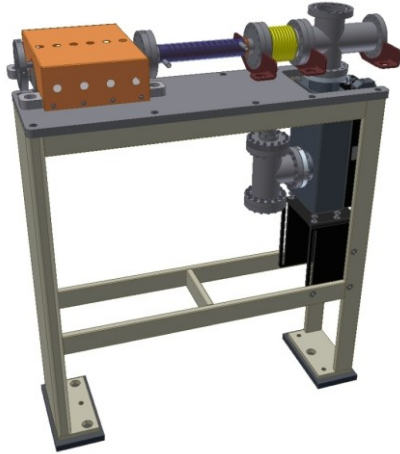


Figure 4-25. Image of the FOE Fixed Mask assembly.



Figure 4-26. Image of the FOE Beam Stop Assembly.



Figure 4-27. Image of the Monochromatic Shutter Assembly.



Figure 4-28. Image of the Pumping/Diagnostics Cross Assembly.

5 END STATION DESIGN

5.1 Overview

While a preliminary design of the endstation has not been done there are a number of conceptual requirements and expected features. These are discussed here.

It is expected that the experimental endstation will consist of the following items:

- Sample Environments
- Sample Stage and Spectrometer
- Collimating Optics
- Analyzer Optics
- Detector(s)

Various sample environments will be used to support the expected range of experiments.

The analyzer optics will be of the CDW scheme for the baseline scope.

The analyzer optics will require the use of a collimating mirror. This mirror is located just downstream of the sample. It will collect a particular solid-angle of the scattered beam, collimate it for acceptance by the analyzer, and then direct it to the analyzer.

The detector will be a strip-detector type, providing resolution enhancement by positional detection, and to improve Q resolution as necessary.

The collimating optics, analyzer optics, detector and flight paths will be in-vacuum. The vacuum design will be to HV/UHV standards, with the expectation that vacuum can be maintained by ion pumps for requirements of low-vibration operation and operation reliability.

The spectrometer will provide motions for the sample and for the detection optics. Scattering from the sample will be collected in the horizontal plane. The base of the spectrometer will be the location of the sample environment and is the pivot point for the spectrometer arm. The sample location is 58 m from the source. There will be two spectrometer arms, one of which is 5 m long, the other 10 m long. One of the two arms will be parked in an off-line location within the experimental hutch while the other arm is in use.

A conceptual image of the spectrometer is shown in Figure 5-1.

Several options are explored for the configuration of the spectrometer arm and analyzer base, including: a large rigid arm; an analyzer base unit with loosely coupled arm truss (this is basis for Section 5.3); virtual-pivot arm configurations; etc. Several options are explored for the supporting/guiding configuration for the analyzer base, including: air-pads running on a granite surface (preferred); rails of various sorts; etc. Several options are explored for the driving/positioning mechanism for the spectrometer arm, including: drive chain; gear at central pivot; long-travel linear drive(s); etc.

The collimating optics will direct the beam to the analyzer at a significant downward angle, providing a challenge to the design of the analyzer base mechanism. The center of the "C" crystal of the CDW optical scheme could be as close as 400 mm to the floor for the 10 m length arm.

The overall design of the instrument will account for future provision of multiple collimating and analyzer optics.

5.2 Sample Environments

One of the major objectives of the high resolution IXS project at NSLS-II is to provide ultimately a substantial advances in field as diverse as, e.g., the onset of quantum effects on the dynamics, the occurrence of liquid-liquid phase transitions, insulator-to-metal crossovers, and other critical phenomena in disordered systems. Since those phenomena typically occur in extreme domains of the thermodynamic plane, it is crucial to equip the beamline

sample environments with state of the art instrumentation allowing exploring these regions. A detailed list of equipment is proposed below.

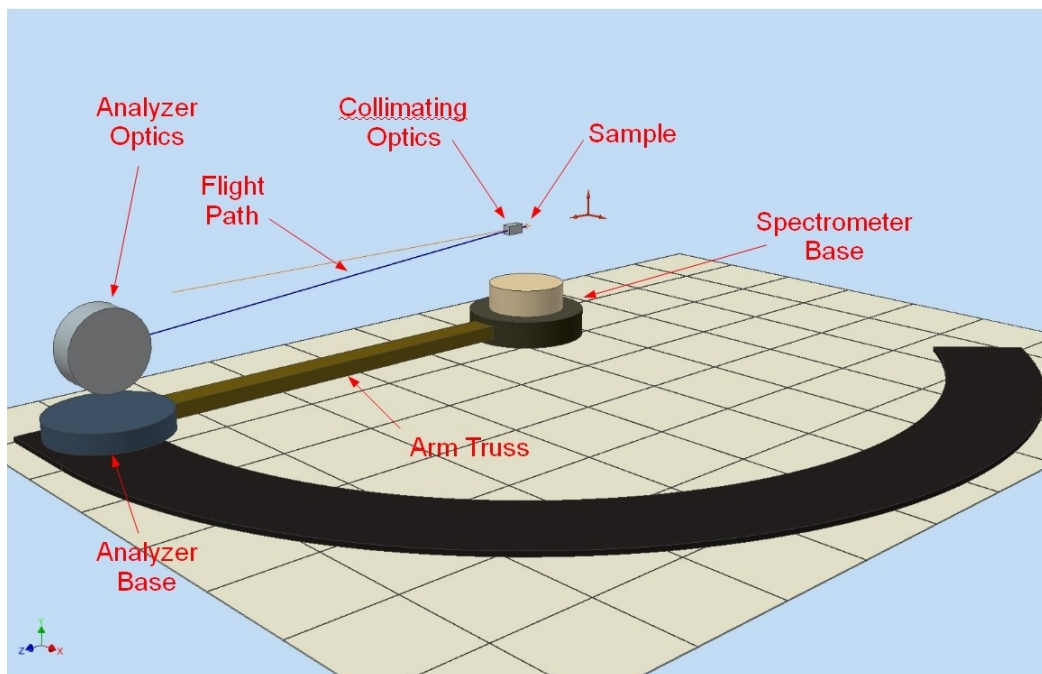


Figure 5-1. Conceptual Image of the 1-meV Spectrometer.

5.2.1 Goniometer, sample positioning and direct beam conditioning system

The use of a goniometer stage is essential to allow the alignment of the sample to both the beam axis and the center of rotation of the spectrometer arm. All axes of rotation of the goniometer as well as the rotation axis of the spectrometer arm must intersect in one point and in such point the sample has to be placed. In order to correctly position the sample the goniometer should provide the motorized rotation (θ), tilt (ϕ , χ) and translation (x , y , z) of the sample container/holder.

In order to clean up the incident and transmitted beam a system of pin-holes will be used both upstream of the sample stage and at the entrance of the spectrometer.

Moreover a set of different thickness x-ray filters will be used to allow an adjustable intensity attenuation of the direct beam.

Some free room surrounding the sample position is essential to allow sample positioning/alignment rotation of the sample in a reasonably large angular range so as to allow, e.g. the proper orientation of crystalline samples.

The sample stage should be able to support loads up to 50 kg. For sample environment exceeding this weight, a counterweight system may be needed.

5.2.2 Special High Temperature Chamber for Inelastic X-ray Scattering

In order to explore high temperatures and reach the melting of many metal samples we plan to use a high temperature oven explicitly built for the beamline with a maximum temperature of around 1700 K. It is worthwhile mentioning that a similar oven is currently in use at both ID28 and ID16 beamlines of the European Synchrotron Radiation Facility in Grenoble and has been employed successfully in several experiments. A picture of such oven is shown in Figure 5-2. Such oven can be purchased from MRI (materials research instruments). The sample (up to

2 cm³) is placed in the middle of the omega resistance and is mainly heated through radioactive thermal exchange with the resistor.



Figure 5-2. A picture of the high temperature oven to be developed at the IXS beamline and the related vacuum chamber.

The use of the oven is very broad, among the most interesting applications we recall the study of liquid metals or fused glass, or more in general the study of disordered systems at the melting, or, finally the investigation of critical phenomena.

5.2.3 The Cryostat

In order to explore the low temperature region we foresee the employment of a cryostat. The kind we have in mind is a Pulse tube which allows reaching cryogenic temperature of a few K. It should be relatively small, light and, potentially work with any inclination (also in the horizontal plane) so as to allow an easy orientation of crystalline samples. The Cryo-Pulse solution is particularly advantageous since it allows an extremely smooth, virtually vibration-free, cooling process. A similar cryostat, presently used at ESRF (working temperature 2.8 K <math>T < 350\text{ K}</math>), is shown in Figure 5-3.

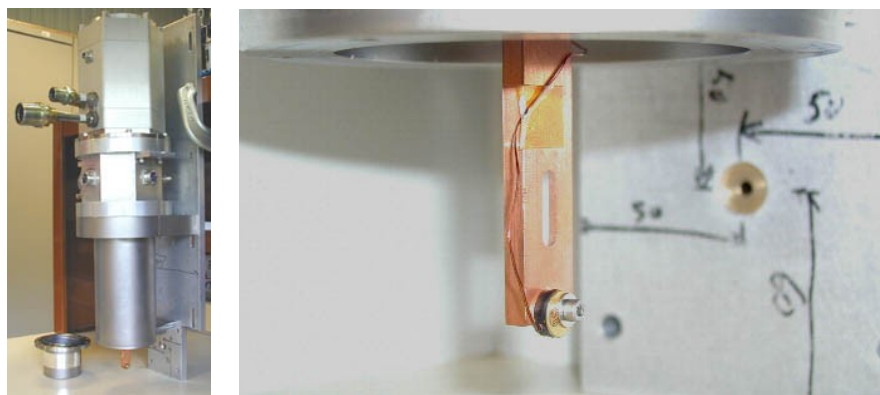


Figure 5-3. A picture of the high temperature oven to be developed at the IXS beamline with a detail of a typical sample holder and temperature sensor

The use of a cryostat is essential in a host of applications, such as the study of liquid-gas transition in noble gases, the study of quantum systems or semiconductors, and the study of a possible polymorphic nature of water, etc.

5.2.4 The high-pressure setups

The high pressure (HP) setup to be used at the beamline strongly depends on the pressure region to be explored. We plan to equip the beamline with 3 different setups to be used in three different pressure ranges (and correspondingly with three different volumes of the sample).

Low pressure (< 5 kbar)

In order to explore relatively low pressure we plan to use a large volume (suited for 1 cm³–sized samples) high pressure cell. Suitable designs are available and can be fabricated by a mechanical workshop for a relatively low price (< 2.5 K\$). The cell windows are flat 1 mm thick diamond disks. This type of low pressure cells have been built and successfully used in other IXS beamlines, such as the ID16, ESRF and at Sector3, APS.

Such model of *HP* cell has demonstrated to operate with pressure stability better than 10 bar at 4 Kbar, within a broad range of T (spanning from a few K to almost 700 K). To explore extreme temperature conditions, special adapting systems will be set up to connect the cell either to the cryostats or to the oven. The cell body can be connected, through a HP capillary tube, with a standard Nova Swiss piston intensifier and a HP gauge allowing a continuous monitoring/adjustment of the hydrostatic pressure.

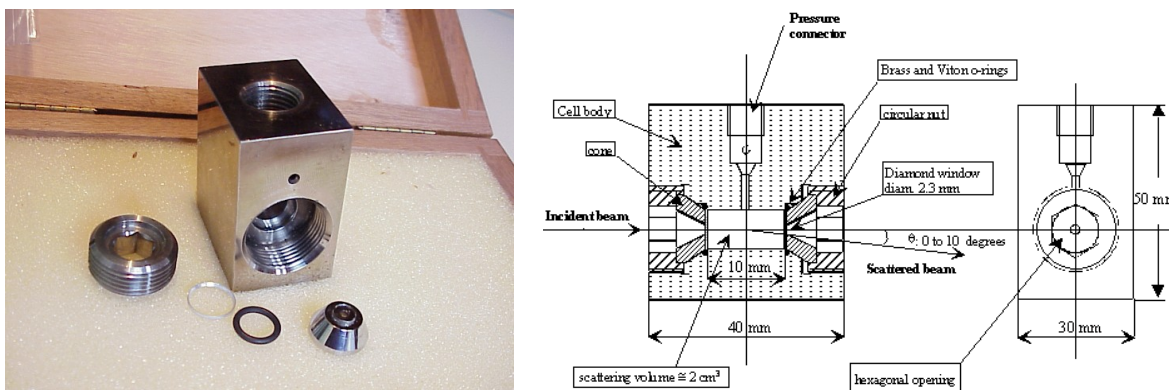


Figure 5-4. A picture of the HP large volume cell (left panel) and a schematic drawing of it (right panel).

Examples of applications of the large volume HP cell include but are not limited to: studies of the dynamics of compressed gases, or simple/hydrogen bonded liquids as, e.g., water and alcohols.

Intermediate pressures (>10 kbar and < 25 kbar)

The intermediate pressures range (between 10 and 25 kbar) will be covered by a high pressure Paris-Edinburgh press, whose schematic drawing is shown in figure 5-5. The high pressure chamber consists of two opposed anvils, which are hollowed out so as to define the pressurized volume for the sample and the pressure transmitting medium. The heating of the sample is achieved through resistors. One problem of this cell is the considerable weights (greater than 70 pounds) which would require the use of appropriate counterweights to limit the load on the goniometer head.

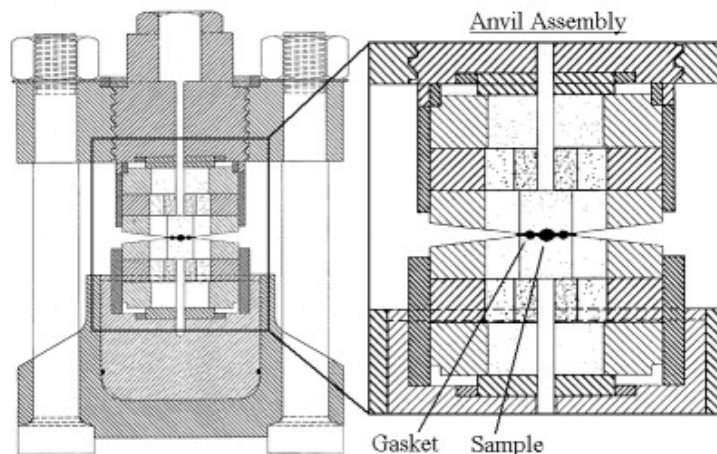


Figure 5-5. A typical drawing of a Paris-Edinburgh press used for X Ray spectroscopy with an enlarged view of the region surrounding the sample .

A host of possible applications can be envisaged for this cell. Relevant examples include IXS investigations on: polymorphic liquid-liquid transitions, liquid to glass transition with pressure, or critical phenomena.

Extremely high pressure ($> 10^4$ bar)

In order to reach extremely high pressures we will finally use a Diamond Anvil Cell, DAC similar to the one reported in Figure 5-6.



Figure 5-6. A picture of a Diamond Anvil Cell, DAC.

The pressure is generated by simply tightening the four screws holding the opposing supports, of the diamond anvils made of high gem quality, flawless diamonds, and 0.2 mm thickness (before compression) gasket foils separating the two culets and containing the hydrostatic fluid in the cavity between the diamonds. The pressure in the DAC can be measured through the shift of the fluorescence line of ruby chips (Al_2O_3 doped with Cr^{3+}). It is well known that such determination cannot be performed *in situ*, but has to be carried out at room temperature before and after each spectral acquisition. Unfortunately, due to the different thermal expansion of the cell components, in principle the pressure changes when the temperature is lowered/raised. An alternative, *in situ*, determination of the pressure can be achieved by measuring (e.g. with a CCD) the pressure-variation of the diffraction pattern of the gasket, since the angular (q -) position of Bragg peaks is dependent on pressure.

Interesting applications of this cell are: studies of phonons in single crystal, insulator-to-metal transitions or the investigation of acoustic properties material of geological interest (as inner earth materials) or material forming the core of planets.

5.2.5 Spectrometer Arm Truss

The spectrometer arm truss will connect the analyzer optics base assembly to the central 2θ rotation platform. This structure will provide a rigid connection in the horizontal plane (2θ rotation plane) plus the longitudinal direction, while providing flexibility in the other rotational planes and directions. This truss will support the vacuum flight path from the collimating optics vacuum chamber to the analyzer optics vacuum chamber. This truss will also support cabling and piping.

There will be two truss assemblies. One will be for the 5m arm, the other for the 10m arm. Each truss assembly will remain attached to its respective analyzer base assembly. One of these analyzer/arm assemblies will be attached to the spectrometer base when in use. The other will be parked within the experimental hutch in an off-line state until needed.

5.3 Collimating Optics

In order to utilize the CDW/CDDW monochromator as analyzer optics, the angular acceptance must be increased to $\sim 5 \times 5$ mrad² by combining with collimating optics to be comparable to those of the current IXS spectrometers. This can be achieved using laterally graded multilayer mirrors, which collect the $\sim 5 \times 5$ mrad² of scattered photons and collimate them to within 0.1×0.1 mrad² for acceptance by the CDW/CDDW optics. This requires multilayer mirrors with a demagnification factor of at least 50:1. The vertical collimation is required because of the angular acceptance of the CDW/CDDW optics, whereas the horizontal collimation is required for two reasons [1]: (1) Near backscattering, the horizontal divergence φ of the incident beam causes energy spread of the reflected beam by $\Delta E/E = \varphi^2/2$. To limit the energy spread to less than 0.1 meV, a horizontal divergence of less than 0.15 mrad is required. For energy spread of less than 1 meV, this horizontal divergence can be relaxed to ~ 0.5 mrad. (2) The horizontal divergence of the beam collected by the multilayer mirror determines the momentum transfer resolution in the scattering plane. For 9.1 keV photons, a 5 mrad acceptance angle of the scattered photons corresponds to a range from ~ 0.23 nm⁻¹ at close to zero momentum transfers to ~ 0.12 nm⁻¹ at momentum transfers of ~ 80 nm⁻¹. In order to improve this further to substantially better than 0.1 nm⁻¹ required by some experiments, one can either reduce the horizontal acceptance of the multilayer mirror according to the required momentum resolution or subdivide the accepted fan into smaller segments after the CDW/CDDW analyzer using a position sensitive detector. How well the latter can be done depends on how well the multilayer mirror collimates in the horizontal direction. A momentum resolution of 0.01 nm⁻¹, for example, would require a horizontal collimation to be better than 0.2 mrad at low momentum transfers. This applies also to the collimation in the vertical as the collected fan defines the momentum transfer resolution in the vertical direction.

We have studied in details the performance of such laterally graded multilayer mirrors by modeling and ray-tracing (see Ref [28]). It involves the optimization of the layer materials, thickness and the mirror figure (parabolic or elliptic), taking into consideration the source size and divergence, mirror errors (slope errors, roughness, and interlayer thickness fluctuation) and imperfections, etc. To achieve collimation in both the vertical and the horizontal directions, we have adopted the so-called Montel optics, where two 1D mirrors are mounted side-by-side at 90 deg to each other [29] (see Figure 5-7). This type of “L-shaped” multilayer mirrors has been used in commercial powder diffractometers, and has been proven to work well [30,31]. To provide the same functionality using a single toroidal mirror would require a rather complicated surface figure, which would be extremely difficult to fabricate. No such mirrors are available currently from commercial vendors that meet our specifications. The only advantage of a single toroidal mirror compared to these “L-shaped” mirrors is that every ray is reflected only once in the former, whereas they are reflected twice in the latter, resulting in some additional loss due to the finite reflectivity. We will monitor the situation and consider the option of a single mirror when such mirrors become available for the improved reflectivity.

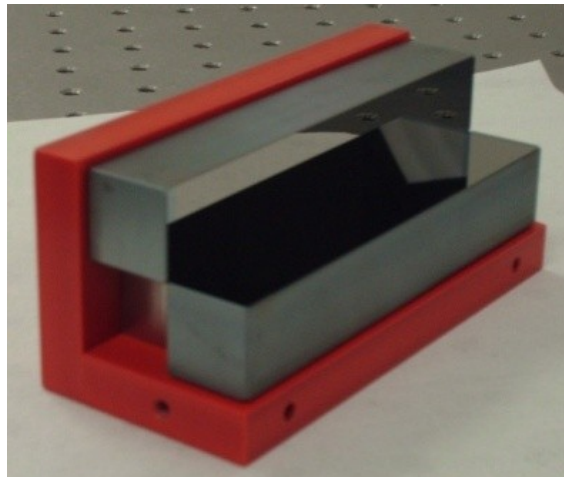


Figure 5-7. A Montel multilayer mirror produced by INCOATEC [32]

Based on the simulation and ray tracing results, we have procured an L-shaped mirror with a parabolic figure to test the performance in terms of reflectivity and collimation (Figure 5-7). The specifications of the mirror have been chosen to collect up to $\sim 10 \times 10 \text{ mrad}^2$ and collimate to $\leq 0.1 \times 0.1 \text{ mrad}^2$ for a source size of $5 \times 5 \text{ }\mu\text{m}$ with a total reflectivity of at least 50%. Table 5-1 summarizes the specifications. Metrology characterization of the mirror has confirmed these specifications.

Table 5-1. Specifications of the Montel multilayer collimating mirror for 9.13 keV

Substrate	Si<100>
Dimension	120 mm × 20 mm × 20 mm
Optical surface	100 mm × 18 mm (clear aperture)
Vertex radius	0.3 mm
Distance between source and mirror center	200 mm
Acceptance angle	> 10 mrad
Meridional slope error	< 10 μrad RMS – spatial sampling 2 – 100 mm
Sagittal slope error	< 10 μrad RMS – spatial sampling 2 – 20 mm
Micro roughness	$\leq 0.2 \text{ nm}$ RMS high spatial frequency roughness – spatial sampling 4 nm – 1 μm
Calculated divergence	$\leq 0.1 \text{ mrad}$ for $5 \times 5 \text{ }\mu\text{m}$ source size
Coating	W-C multilayers
Stripe dimension	100 mm × 18 mm
Multilayer period (graded)	2.20 – 2.87 nm
Interface roughness	2 – 3 Å RMS
Number of layer pairs	100
Theoretical reflectivity	$\sim 70\%$ @ 9.1 keV

Within the prototype system mentioned in Section 4.3, the multilayer mirror will be mounted on an independent goniometer stage located between the two CDDW units. The scattering geometry is shown in Figure 5-8. In order to

constraint the scattering in the vertical plane so that the measurement of the scattered beam collected by the multilayer mirror involves only a vertical translation and an overall angular rotation of the CDDW analyzer from its inline position, the L-shaped multilayer mirror will be mounted 45° rotated around its corner axis with respect to the nominal horizontal mounting position. In this configuration, the diffraction condition of the L-shaped multilayer mirror is met with an incident angle of $\sim 2.25^\circ$ (or a scattering angle of $\sim 4.5^\circ$ with respect to the incoming beam) in the vertical plane. Another consequence of rotating the multilayer mirror by 45° is that the image of the collimated beam is also rotated by 45° . This effectively increases the horizontal beam size by 40%, which to our advantage will help increase the acceptance of the CDDW analyzer in this configuration.

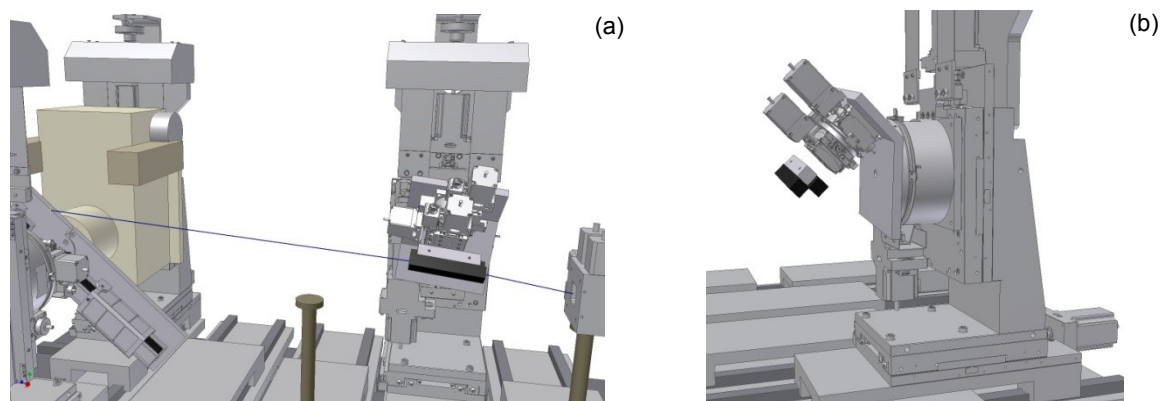


Figure 5-8. The scattering geometry with the multilayer mirror in a vertical scattering geometry (a). The goniometer arrangement for the multilayer mirror (b). The “L-shaped” multilayer mirror is rotated 45° about its corner axis in order to constraint the scattering in the vertical plane.

5.4 Analyzer Optics

The analyzer optics will be based on the same CDW/CDDW optics being developed for the high-resolution monochromator. A few points that we should address:

- Each analyzer must be coupled with a collimating mirror. The incoming beam divergence is expected to be at least $100 \mu\text{rad}$. Therefore, each analyzer must be designed for a specific energy resolution.
- Multiple analyzers require multiple collimating mirrors.
- The vertical focal size from the multi layer mirror is expected to be $\sim 0.5 \text{ mm}$ with a focusing collimating mirror for a $5 \mu\text{m}$ focus on the sample. This beam size will be larger if the multilayer mirror is collimating rather than focusing, or if the analyzer optics cannot be placed at the focal point of the multilayer mirror. The D crystal length needs to be long enough to accept the full beam.
- The mechanism may include multiple D crystals in stack-up or line-up mode.
- While the initial alignment of the analyzer optics can be done either with the direct incident beam from the high-resolution monochromator, or with the elastic scattered signal from a sample. The alignment must be sustained by the mechanism itself during the experiment. Any feedback control relying on the weak scattering signal (a few counts per sec) would be extremely difficult if not impossible. How to maintain the alignment mechanically would be a challenge. Some form of feedback control might be necessary (e.g., using laser interferometry).

Our initial goal is to develop an analyzer optics based on the CDW scheme for 1 meV resolution operation. The above considerations will be taken into account.

5.5 Detectors

The IXS experiment relies critically upon a multiple-pixel spectroscopic detector system to capture and record scattered x-rays passing through the analyzer optics. This system is currently projected to be a strip detector designed and fabricated at BNL by the detectors group of NSLS/NSLS-II (Figure 5-9). Integration requirements with respect to the geometry of the analyzer, as well as vacuum, cooling, and electronics are under development. Alternative designs are also under consideration in case the in-house device is not ready for day-one operation.

Additional detectors and diagnostics for the experimental hutch and beamline as referred to in section 4.6.2 are also described below.

Ancillary detectors available to the experimental hutch include point detectors of various forms (scintillators, PIN, SDD, APD, PD), as well as camera/telescope and phosphor screens for setup and diagnostics. Ion chamber or equivalent solid state device will be available for flux and position monitoring at the sample location.

Diagnostic sensors for alignment of the monochromator and analyzer are expected to be integrated. These may be silicon or diamond photodiodes, possibly with pneumatic actuators to insert and remove them from the beam or transmission geometry to pass the beam (solid state ion chamber arrangement). They also may include segmentation for position sensing. Photodiode readouts are anticipated to be low-current type. Alternative devices include compact APDs and associated electronics.

Diagnostic sensors for alignment and optimization of the beamline optics (CRL, DCM, mirrors, slits etc.) may take several forms, including (but not limited to) screen/camera systems, quadrant transmission diodes, and foil BPMs.

Support electronics for the diagnostics are expected to be located near the sensors and are therefore distributed along the beamline, allowing control and read back access via the beamline controls network.



Figure 5-9. A BNL strip detector designed and fabricated by the NSLS/NSLS-II detector group.

6 INFRASTRUCTURE FOR BEAMLINE AND USER SUPPORT

6.1 Hutches

The IXS beamline will have four radiation safety enclosures (hutches). Hutch A (FOE) will contain all of the white beam components. Hutch B is for the High-Resolution Monochromator. Hutch C will contain the upstream set of K-B mirrors (mature scope) and also provisions for optics development. Hutch D will contain the downstream set of K-B mirrors and the experimental endstation (spectrometer). Hutch A is a lead-lined white-beam hutch; the others are steel walled monochromatic-beam hutches. Each hutch will be 3.5 m in height to the outside top surface.

Each of the hutches A and B will have a sliding double-door arrangement with a 2 m wide opening. Hutch C will have one sliding double-door of 2 m width and one sliding single-door of 1 m width. Hutch D will have one sliding double-door of 2 m width and two sliding single-doors of 1 m width each. There will be no windows in any of the hutches. (Visual access to the hutch interiors will be provided by web-based video cameras.)

Each of the hutches will have three roof mounted labyrinths. These will be allocated to utilities and instrument requirements. Hutch A will have one additional labyrinth for monochromator cryo-cooler use. Hutch D will have two additional labyrinths for instrument cabling use.

Each of the hutches B and C will have one key-accessible interlocked labyrinth for use by the Users. Hutch D will have two such labyrinths. These will be accessible from floor level.

Each of the hutches A and B will have one electronics equipment rack located on the roof of the hutch. Hutch C will have two racks on the roof. Hutch D will have six racks on the roof. It is expected that all of these racks will be used for beamline related equipment such as networking, motors, vacuum, EPS, PPS, etc.

There will be two electronics equipment racks at floor level allocated for frequent-access equipment such as computers, detector electronics, meters, NIM bins, controllers, etc. These will also be available for temporary User needs.

Each hutch roof will be accessible from the Mezzanine level, via walkways along the roofs and a bridge located between hutches B and C. There will be a set of stairs to the roof of hutch D. The hutch roofs and the bridges will be equipped with a safety hand rail and kick plates.

Each of the hutches A, B, and C will have a full-coverage manual hoist. Each hoist will have a capacity of 1000 kg. Hutch D will have a partial-coverage hoist of 250 kg minimum (1000 kg if possible) capacity. This hoist will cover the K-B mirror, sample, and some of the zero-beam analyzer arm area.

Hutch specifications and overview drawings are provided in the Appendix.

Hutches A and B are shown in Figure 6-1. Hutches C and D are shown in Figure 6-2.

In addition to controls for optics and diagnostics, controls for hutch environment will also be included in the IXS beamline design. Specifically, temperature sensors (1-wire monitors), variable hutch lighting and remote cameras are included in the controls layout as indicated in the attached drawing A2-13.



Figure 6-1. Hutch A (FOE) and Hutch B (High-Resolution Monochromator)

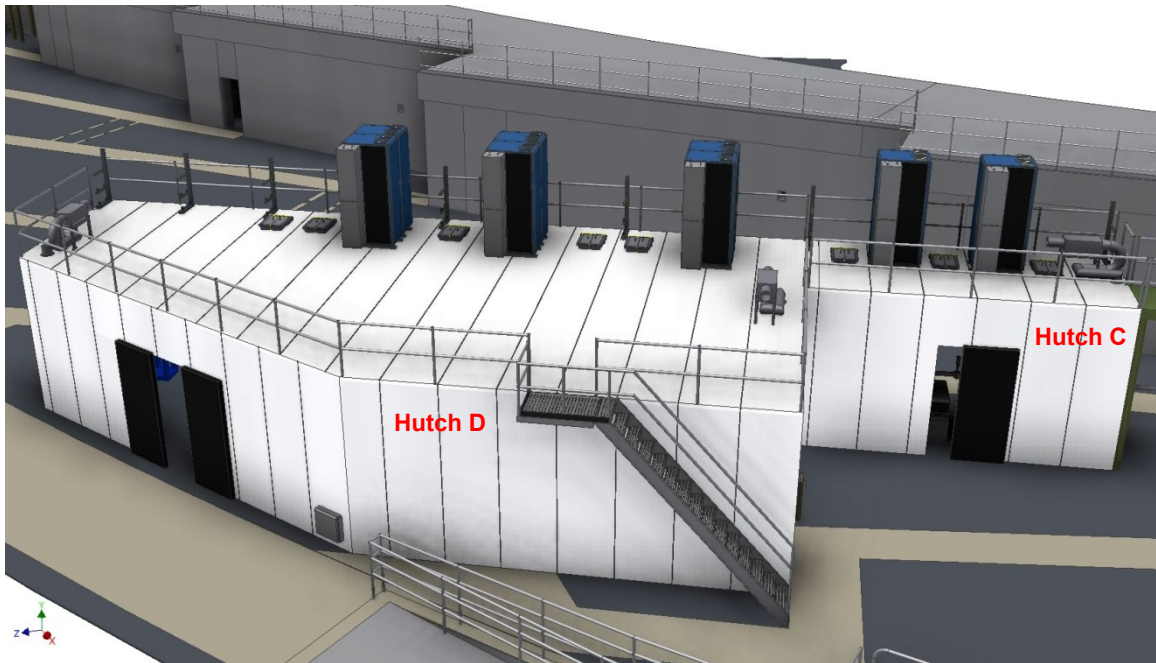


Figure 6-2. Hutch C (Optics Development) and Hutch D (Experimental Hutch).

6.2 Environmental Requirements

6.2.1 Temperature

Each of the four hutches will be temperature controlled to improve the mechanical stability of the optics devices.

The temperature in each hutch will be controlled by way of the hutch's air-handling system. Each hutch is fitted with one or two roof-mounted forced-air blower unit(s), which are incorporated with an air inlet heat exchanger for temperature control. Inside each hutch an 'air sock' device located at ceiling level and running the length of the hutch will be used to create a uniformly distributed air flow. Air exits each hutch through air outlet labyrinths located at the base of the sidewalls. Other temperature stabilization techniques will be evaluated during the design phase of the hutches.

Hutch A (FOE) will be designed to provide temperature stability at the ± 0.3 °C level. Temperature stability requirements are not critical.

Hutches B, C and D will be designed to provide temperature stability at the ± 0.1 °C level. This is required for the mechanical stability of the high resolution optics located within each of these hutches.

As indicated in section 6.1, temperature sensors (1-wire monitors) for each of the hutches are included in the controls layout as indicated in the attached drawing A2-13.

6.2.2 Other

There are no other critical environmental requirements for the hutches.

As indicated in section 6.1, controls for hutch lighting will also be included in the IXS beamline design. For optimum remote viewings of hutches, experimental systems and diagnostics, variable hutch lighting and remote cameras are included in the controls layout as indicated in the attached drawing A-13.

6.3 Surveying Requirements

The NSLS-II facility, including the storage ring tunnel and experimental floor, is fitted with a network of survey monuments referenced to a pair of monuments in the center of the ring. This network will be regularly surveyed with a laser tracker to create a robust and accurate network of arbitrarily positioned monuments. Monuments can be added as required, including inside hutches and on the storage ring wall etc. Positioning a laser tracker on a tripod such that it can view more than three monuments allows it to calculate its position, and the position of any new monuments.

Precision machined holes in components are surveyed prior to installation, relative to the component aperture, crystal, mirror or grating surface etc., fitting a reflector into the precision hole allows the laser tracker to survey the absolute reflector position so that the aperture or optic position can be accurately calculated. This system of surveying is extremely accurate, globally (within the NSLS-II complex) components may be positioned to within 100 microns, and where components are close to one another (within a few meters and without sighting restrictions) the accuracy improves to ~30 microns.

6.4 Controls and Data Acquisition Requirements

6.4.1 Beamline and Hutch Controls

The IXS beamline will make use of the NSLS-II controls network to access all devices along its length, including optical and experimental systems. Controls elements can be considered actuators or sensors.

Most actuators are stepper motors. For fine controls, piezo or picomotor-style actuators may be implemented. Some additional actuators are pneumatic (such as moving valves, diagnostics, or beam conditioning elements). Temperature control for the optical elements may also be accomplished using closed-loop temperature controllers (heaters). Bimorph mirror figures will be adjustable on-the-fly using dedicated voltage control electronics.

Beamline sensors range from beamline diagnostics (such as temperature/flow meters and beam position/intensity monitors) to experimental detector systems (including strip detector anticipated for the IXS spectrometer).

Further details about specific components can be found in the beamline controls layout drawing Figure A2-13.

6.4.2 Data Acquisition

Data acquisition for IXS will take the form of “step-and-count,” meaning that each scattering intensity value measured as a function of energy and angle will be a static measurement (no motors moving). Single photon counting will be used for scattering data.

IXS data sets will likely be collected continuously over several hours or days, so stability of energy and angle, as well as maintenance of maximal intensity (count rates are expected to be low) will be required. Scripting of incremented angle / energy steps will be required. Visualization of data in 1 or 2 dimensions will be required.

Where “step-and-count” cannot be used at IXS is mainly at the temperature control of optics which controls the energy. In this case, data may be collected at a range of temperatures (energies) and for each event (photon detected) the parameters must be recorded. In this “fly scan” mode, data will need to be sorted and binned for usable representation.

Beamline diagnostics data will also be harvested for troubleshooting and investigation of correlations between environmental parameters. Any or all of the beamline, accelerator, and facility variables may be utilized along with experimental data and visualized using scientific software in order to maximize understanding of any beamline issues should they arise.

6.5 Utilities Requirements

The utilities requirements for the IXS beamline will be met by the standard utilities package. There are no special utilities requirements anticipated.

The DCM located in Hutch A (FOE) will require LN2 for its attendant Cryo-cooler. It is expected that the Cryo-cooler will be located on the mezzanine adjacent to the LN2 panel, which is adjacent to the FOE. This will minimize the length of the connection to the LN2 panel. The Cryo-cooler hoses connecting to the DCM will run off of the mezzanine onto the FOE roof, through a labyrinth, and to the DCM.

All other utilities and their uses are listed by hutch in the following Tables.

Table 6-Error! No text of specified style in document.-3. Hutch A (FOE) Utility Requirements

Utility	Device(s)	Notes
Compressed Air	Gate Valves	Intermittent
Nitrogen Gas	N/A	Purging of vacuum chambers
DI Cooling Water	Fixed Mask, DCM, White Beam Stop	
Chilled Water	Electronics Racks	Located on hutch roof
Cylinder Gas	None	
AC power	Lighting and outlets	120V, 15/20A outlets

Table 6-2. Hutch B (High Resolution Monochromator) Utility Requirements

Utility	Device(s)	Notes
Compressed Air	Gate Valves	Intermittent
Nitrogen Gas	N/A	Purging of vacuum chambers
DI Cooling Water	None	
Chilled Water	Electronics Racks	Located on hutch roof
Chilled Water	Recirculating Chiller	HRM Temperature Control System
Cylinder Gas	Gas Outlet Panel	As-needed temporary gas supplies
AC power	Lighting and outlets	120V, 15/20A outlets

Table 6-3. Hutch C (Optics Development) Utility Requirements

Utility	Device(s)	Notes
Compressed Air	Gate Valves	Intermittent
Nitrogen Gas	N/A	Purging of vacuum chambers
DI Cooling Water	None	
Chilled Water	Electronics Racks	Located on hutch roof
Chilled Water	Recirculating Chiller	Test Temperature Control System
Cylinder Gas	Gas Outlet Panel	As-needed temporary gas supplies
AC power	Lighting and outlets	120V, 15/20A outlets

Table 6-4. Hutch D (Experimental Endstation) Utility Requirements

Utility	Device(s)	Notes
Compressed Air	Gate Valves	Intermittent
Compressed Air	Spectrometer Air Pads	Intermittent, very low flow
Nitrogen Gas	N/A	Purging of vacuum chambers
DI Cooling Water	None	
Chilled Water	Electronics Racks	Located on hutch roof
Chilled Water	Recirculating Chiller	Analyzer Temperature Control System
Cylinder Gas	Gas Outlet Panel	As-needed temporary gas supplies
AC power	Lighting and outlets	120V, 15/20A outlets

6.6 User Space

There will be an enclosed area for the user control stations, sample preparation space, and interaction space. This cabin will be located on the upstream and outboard side of Hutch C. See Figure 6-3 for a conceptual image of this cabin.

The cabin shown provides approximately 42 m² of floor space. It is expected that this space will be fitted out with modular-type desk space, electronic equipment racks, table space, bench space for sample preparation, storage

cabinets, etc. Location, size, and quantities of doors and windows will be considered during the layout of the interior of the cabin.

The cabin provides a quiet working environment for users; at the same time, it minimizes thermal exchange with the experimental hall when access to Hutch C and D is required during experiments, which will help maintain the temperature stability of Hutch C and D.



Figure 6-3. User Space Cabin Concept.

7 SPECIAL BEAMLINE REQUIREMENTS

As written in the preceding sections of this report, there are several special requirements for this beamline that are outside the normal utilities provision for beamlines (the standard utilities pack). They are described above in detail, and summarized below as a bulleted list.

- Air temperature control (± 0.1 °C)
- Baffled air flow to minimize air currents
- Signal patch panel (BNC, HV, RS232, ethernet, etc.)
- Experimental gas farm and station patch panels with flowmeters (He, N₂, Ar)
- Floor fiducials

APPENDIX 1: SCHEDULE

September 30	2010	Preliminary Design Report
October 19-20	2010	PDR Technical Review
November 15-17	2010	DOE review
November 03	2010	Technical Design – Approval of Long Lead Time Procurement
January 11	2011	Start Long Lead Time Procurements (monochromator, mirrors, enclosures, ...)
April 14	2011	Complete Final Design of Beamline Major Components
February 07	2012	Complete Final Design Report
April 1	2012	Beneficial Occupancy of Experimental Floor
April 10	2012	Start Installation
May 15	2012	Start Sub-System Testing
April 20	2012	Start Other Procurement
November 05	2012	Complete Long Lead Time Procurements
August 14	2013	End Procurement
August 19	2013	Start Integrated Testing
January 07	2014	Complete Installation
February 03	2014	Complete Sub-System Testing
February	2014	Complete Integrated Testing – Beamline available for Commissioning
February	2014	Beam-ready
June	2015	CD-4, Approve Start of Operations

APPENDIX 2: REFERENCE DRAWINGS

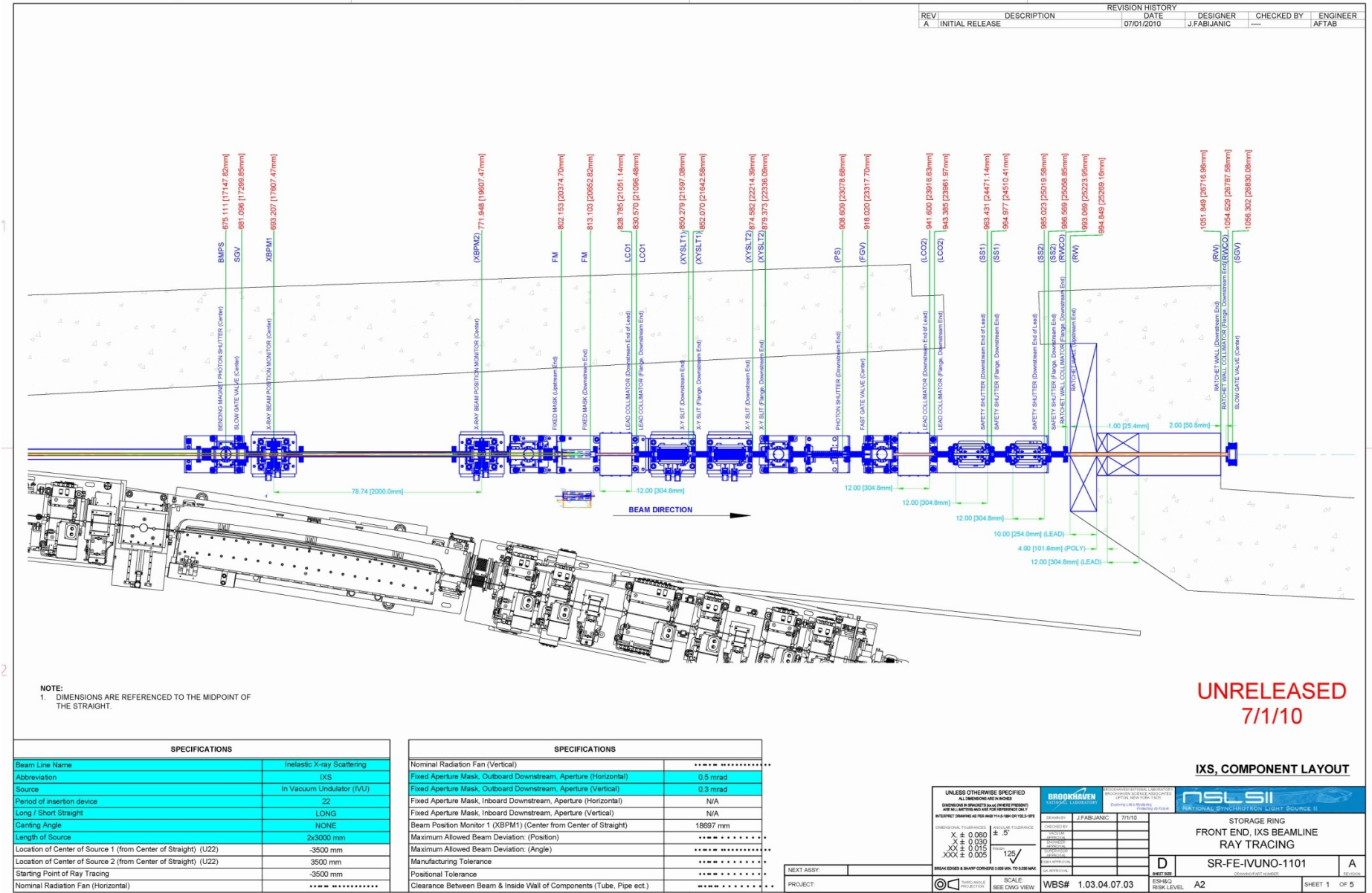
The following drawings are provided here for reference:

- Figure A2-1: Sector Layout
- Figure A2-2: Front End Layout
- Figure A2-3: Front End Horizontal Synchrotron Ray Tracings
- Figure A2-4: Front End Vertical Synchrotron Ray Tracings
- Figure A2-5: Front End Horizontal Bremsstrahlung Ray Tracings
- Figure A2-6: Front End Vertical Bremsstrahlung Ray Tracings
- Figure A2-7: Beamline Layout (plan & elevation view)
- Figure A2-8: Beamline Horizontal Synchrotron Radiation Ray Tracings
- Figure A2-9: Beamline Vertical Synchrotron Radiation Optical Aperture Ray Tracings
- Figure A2-10: Beamline Horizontal Bremsstrahlung Ray Tracings
- Figure A2-11: Beamline Vertical Bremsstrahlung Ray Tracings
- Figure A2-12: Shielding Enclosure Layout
- Figure A2-13: Utility Layout
- Figure A2-14: Personnel Safety System Schematic Layout
- Figure A2-15: IXS Beamline Controls Layout

Figure A2-1: Sector Layout



Figure A2-2: Front End Layout



UNRELEASED
7/1/10

IXS, COMPONENT LAYOUT

SPECIFICATIONS	
Beam Line Name	Inelastic X-ray Scattering
Abbreviation	IXS
Source	In Vacuum Undulator (IVU)
Period of insertion device	22
Long / Short Straight	LONG
Clanking Angle	NONE
Length of Source	2x3000 mm
Location of Center of Source 1 (from Center of Straight) (LZ2)	-3500 mm
Location of Center of Source 2 (from Center of Straight) (LZ2)	3500 mm
Starting Point of Ray Tracing	-3500 mm
Nominal Radiation Fan (Horizontal)

SPECIFICATIONS	
Nominal Radiation Fan (Vertical)
Fixed Aperture Mask, Outboard Downstream, Aperture (Horizontal)	0.5 mrad
Fixed Aperture Mask, Outboard Downstream, Aperture (Vertical)	0.3 mrad
Fixed Aperture Mask, Inboard Downstream, Aperture (Horizontal)	N/A
Fixed Aperture Mask, Inboard Downstream, Aperture (Vertical)	N/A
Beam Position Monitor 1 (XBP1) (Center from Center of Straight)	18687 mm
Maximum Allowed Beam Deviation (Position)
Maximum Allowed Beam Deviation (Angle)
Manufacturing Tolerance
Positional Tolerance
Clearance Between Beam & Inside Wall of Components (Tube, Pipe ect.)

UNLESS OTHERWISE SPECIFIED ALL DIMENSIONS ARE IN MILLIMETERS UNLESS OTHERWISE SPECIFIED		BROOKHAVEN NATIONAL LABORATORY		NLSL II NATIONAL SYNCHROTRON LIGHT SOURCE II	
DESIGNED BY	J.FABJANIC	DATE	7/1/10	STORAGE RING	FRONT END, IXS BEAMLINE RAY TRACING
CHECKED BY		SCALE	125%	PROJECT	SR-FE-IVUNO-1101
APPROVED BY		WBS#	1.03.04.07.03	RISK LEVEL	A2
DATE		SHEET NO.			

Figure A2-3: Front End Horizontal Synchrotron Ray Tracings

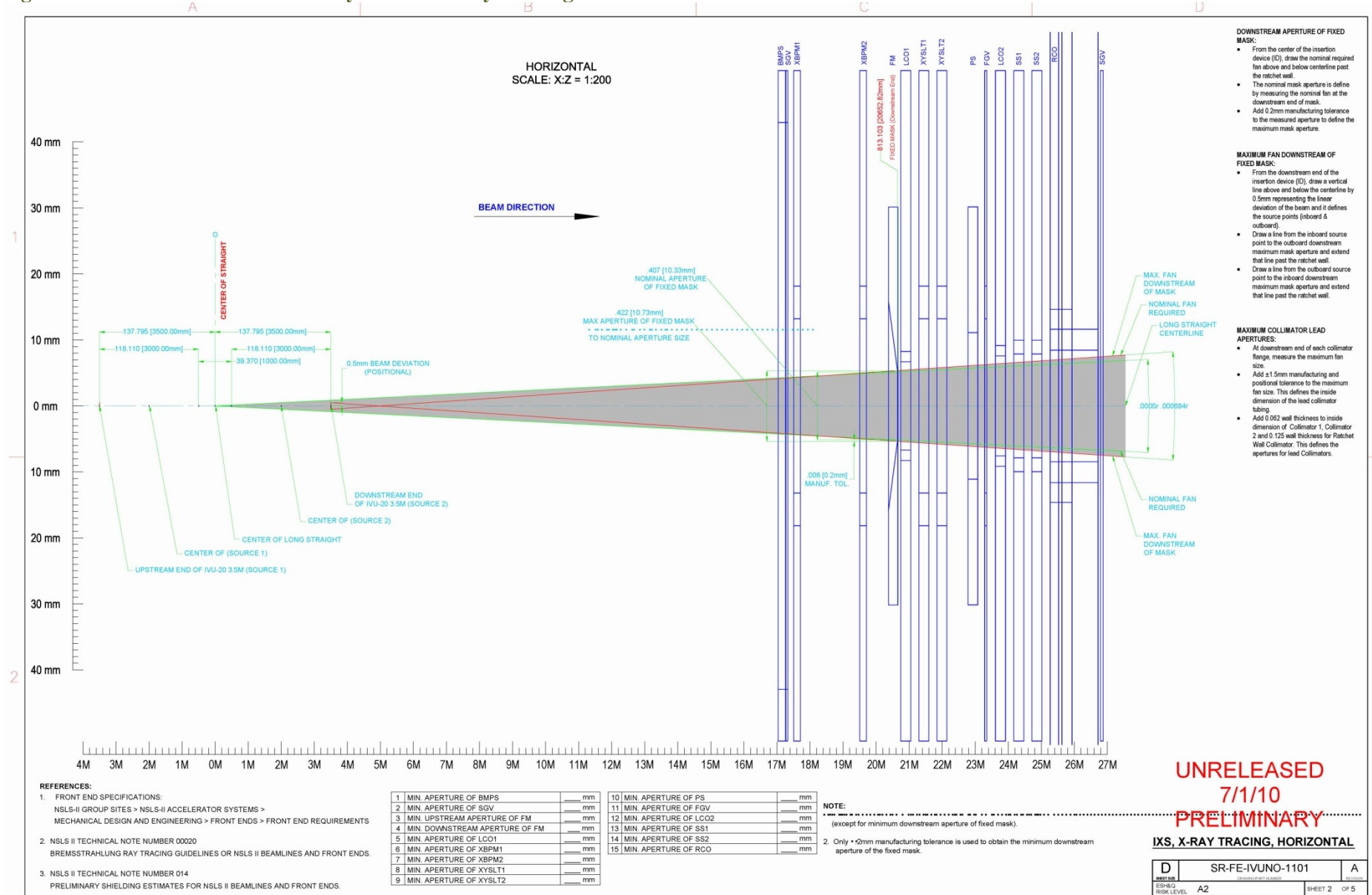


Figure A2-4: Front End Vertical Synchrotron Ray Tracings

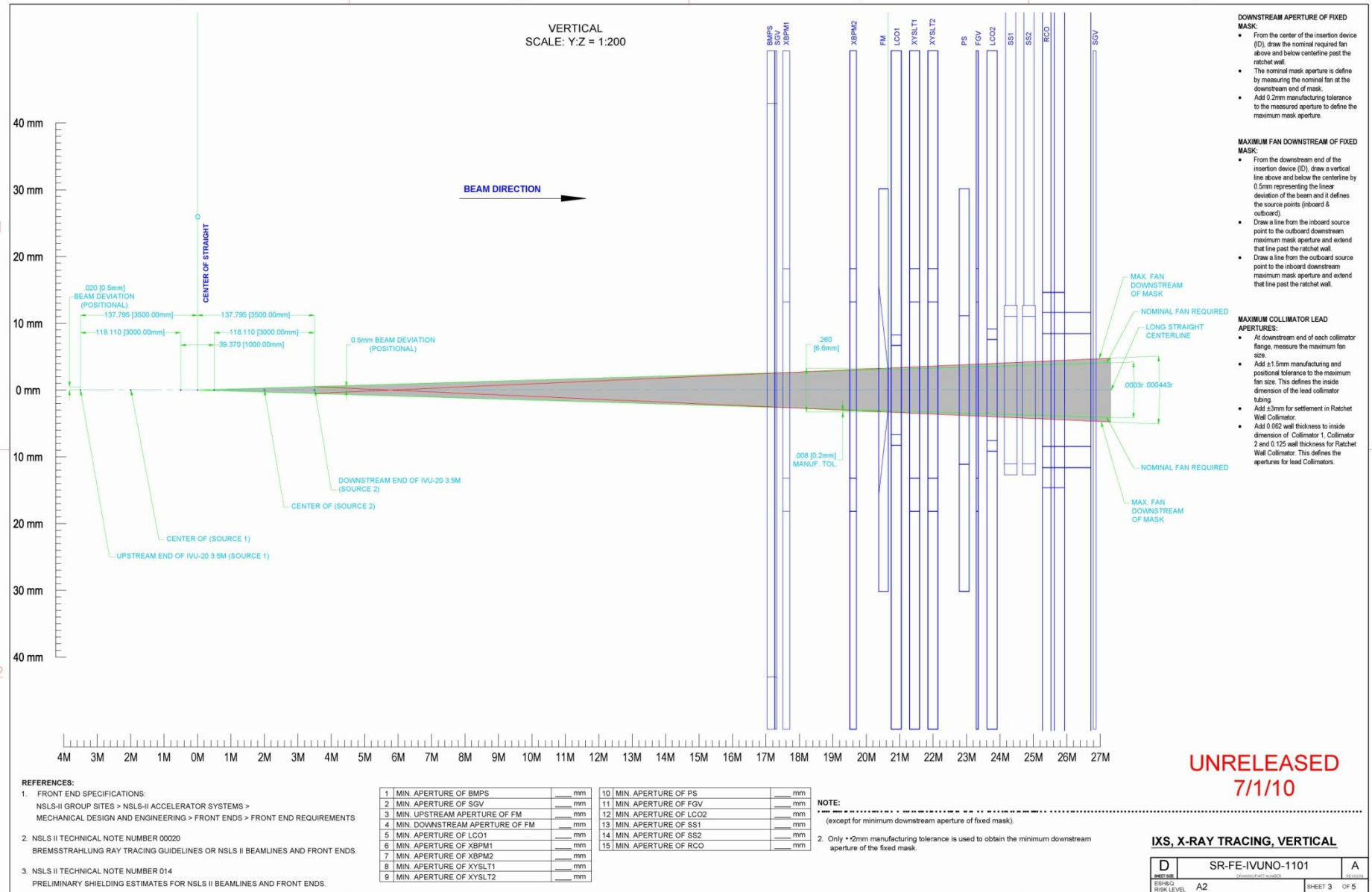


Figure A2-5: Front End Horizontal Bremsstrahlung Ray Tracings

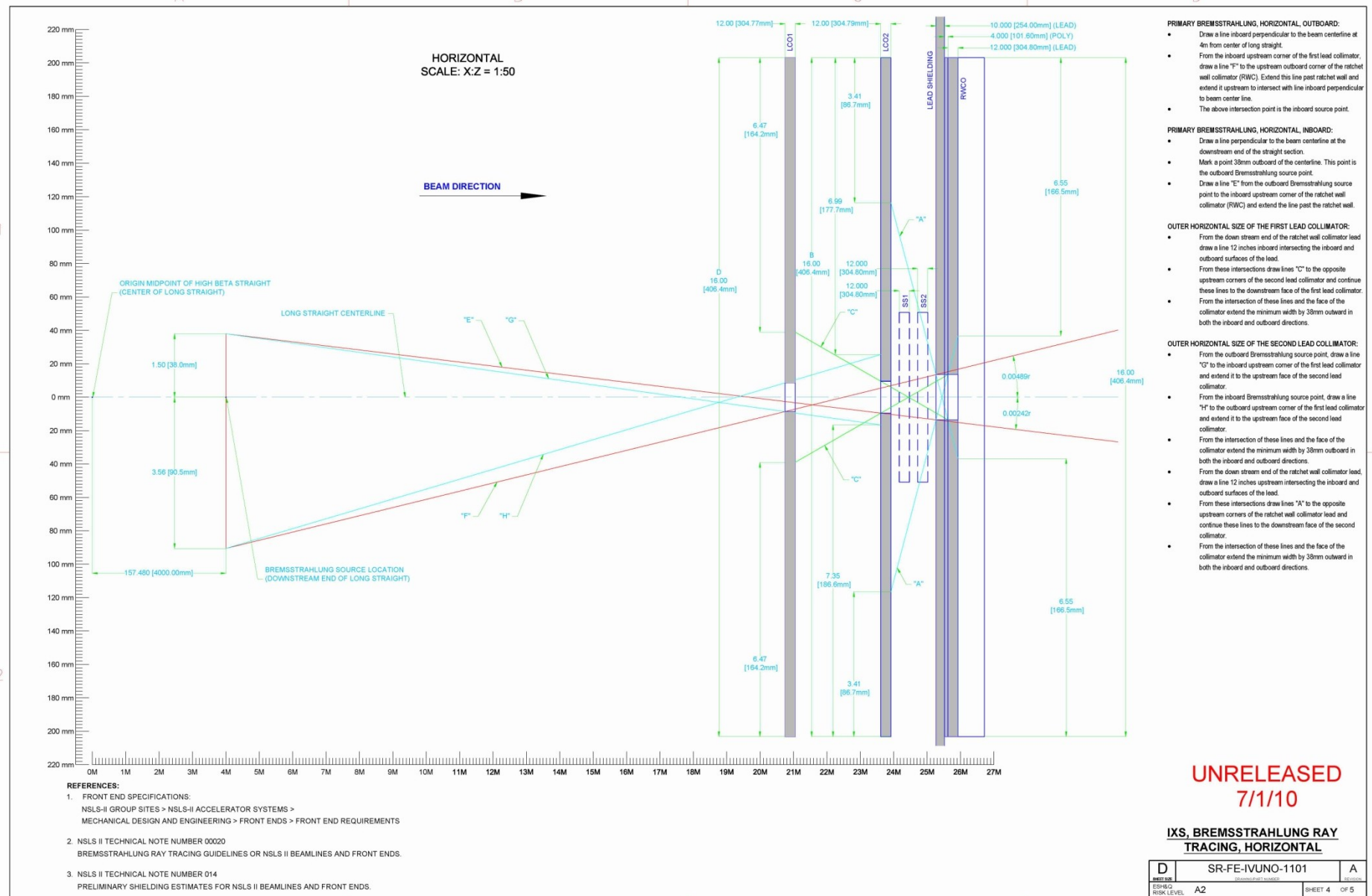


Figure A2-6: Front End Vertical Bremsstrahlung Ray Tracings

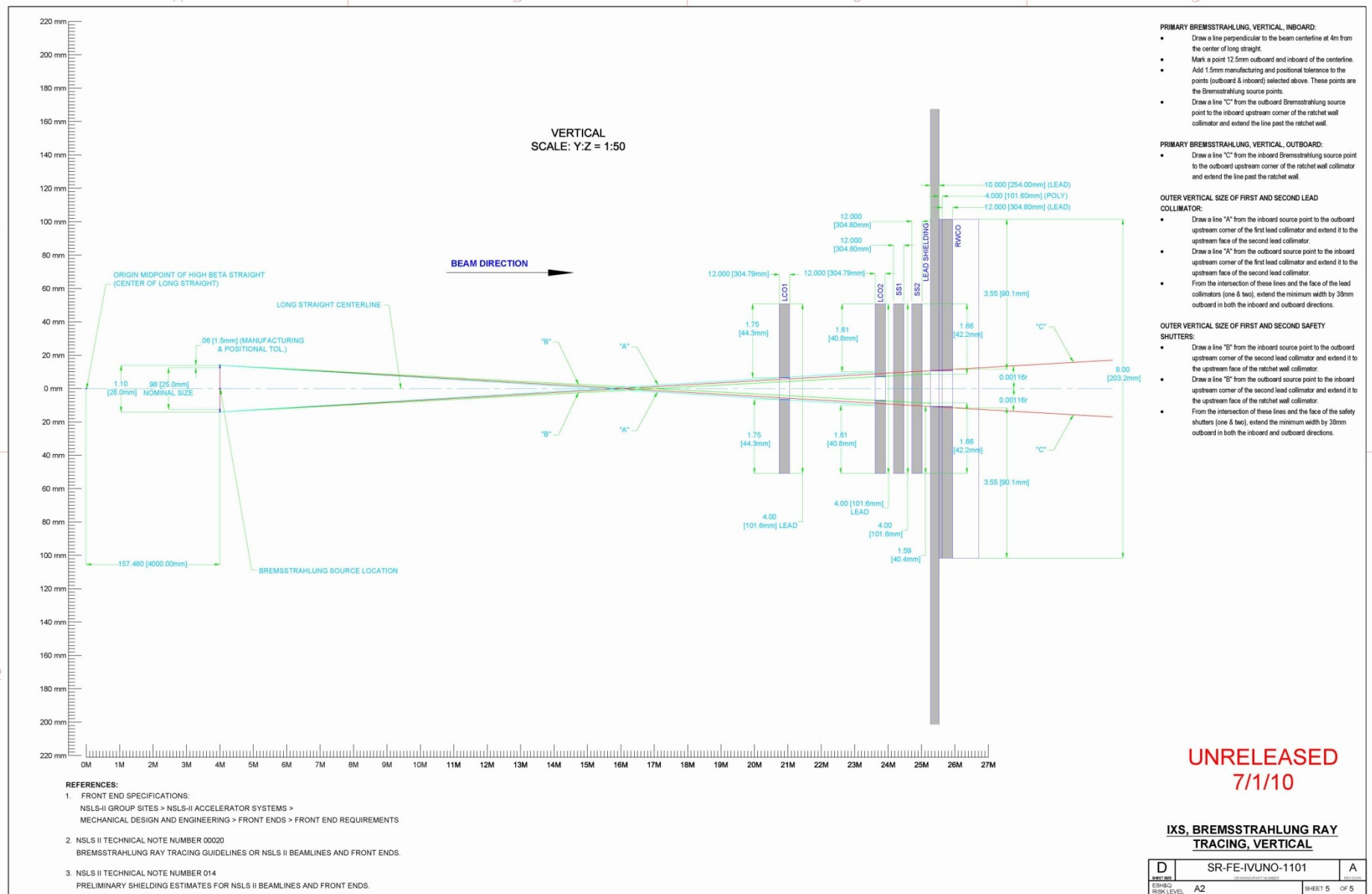


Figure A2-7: Beamline Layout (plan & elevation view)

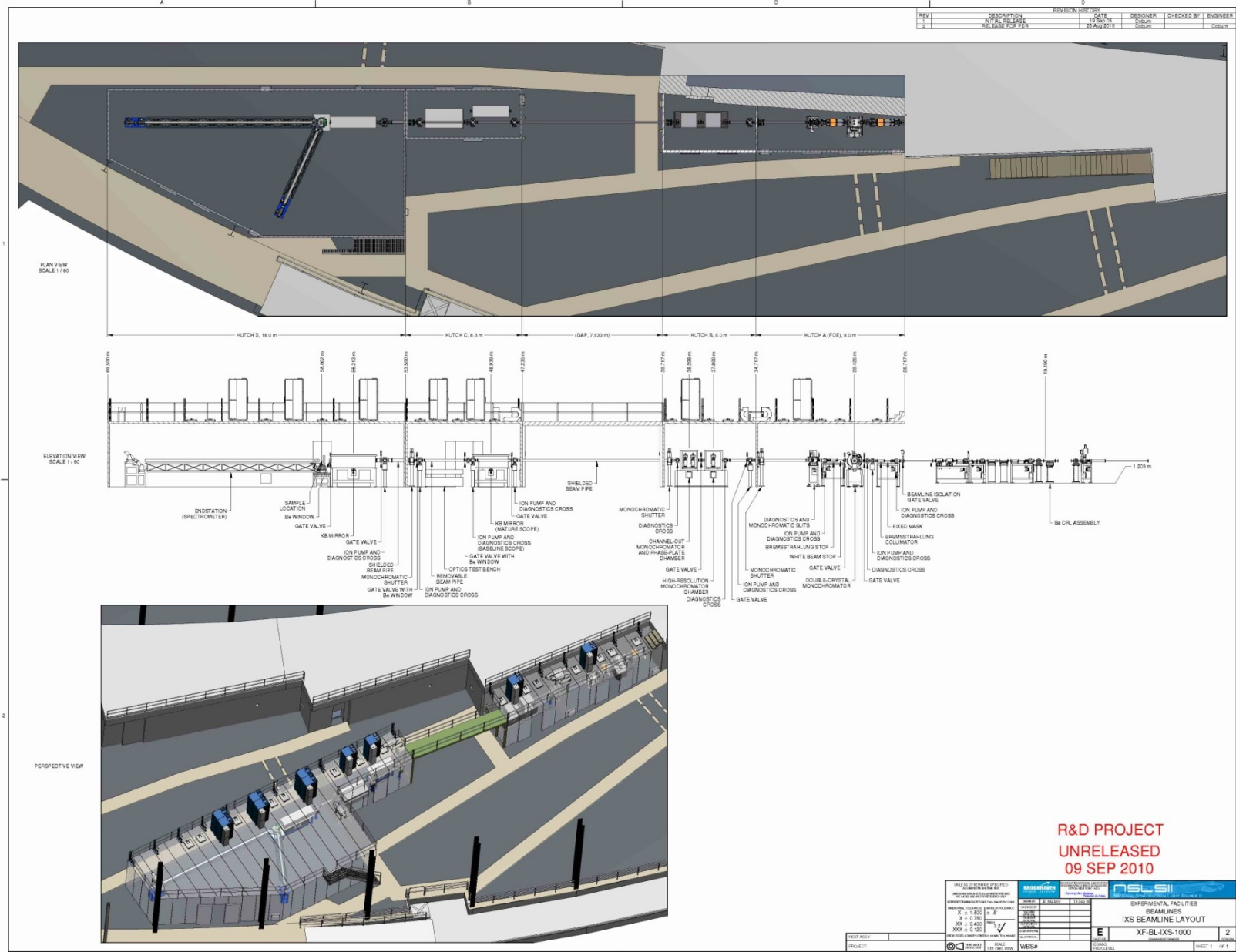


Figure A2-8: Beamline Horizontal Synchrotron Radiation Optical Aperture Ray Tracings

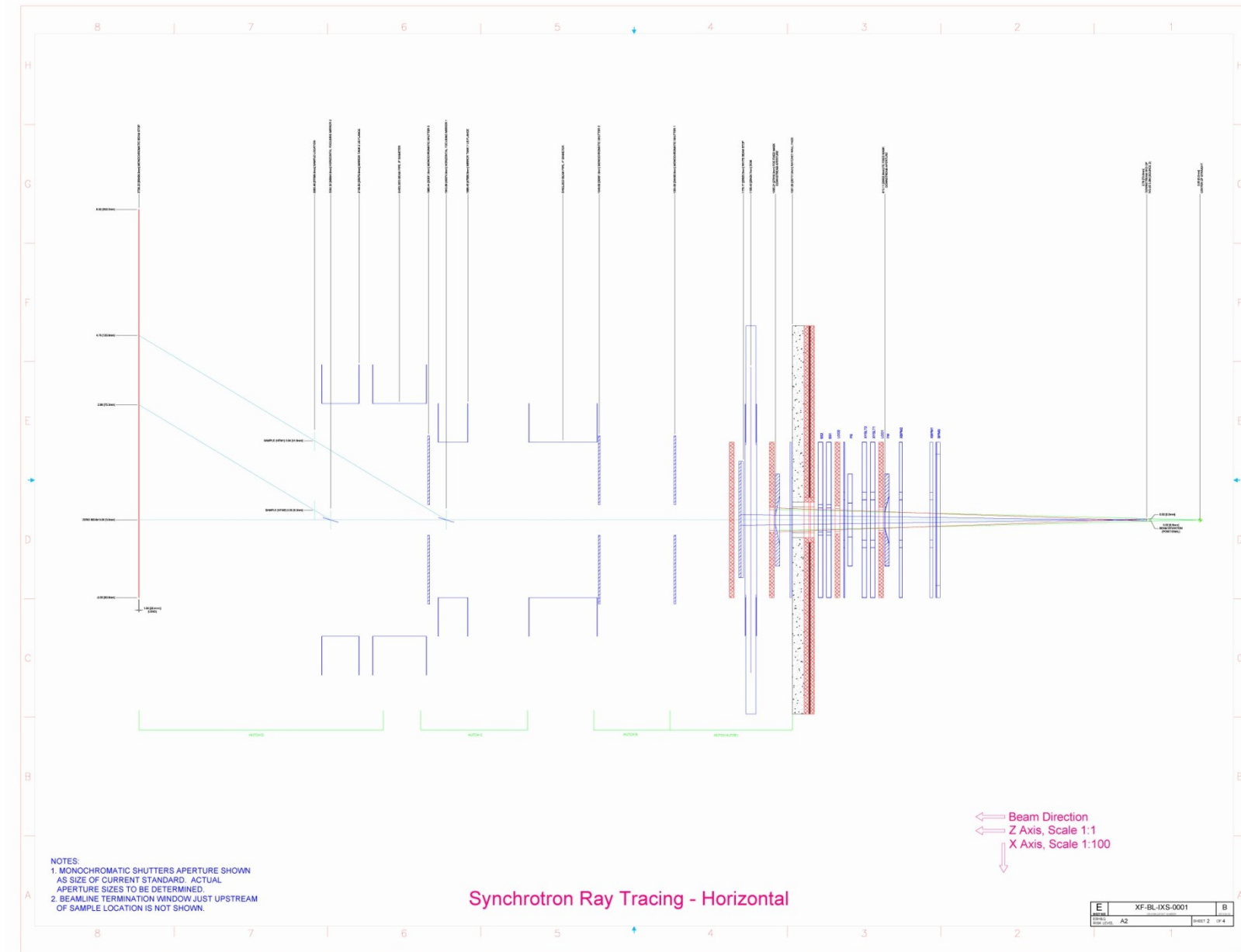


Figure A2-10: Beamline Horizontal Bremsstrahlung Ray Tracings

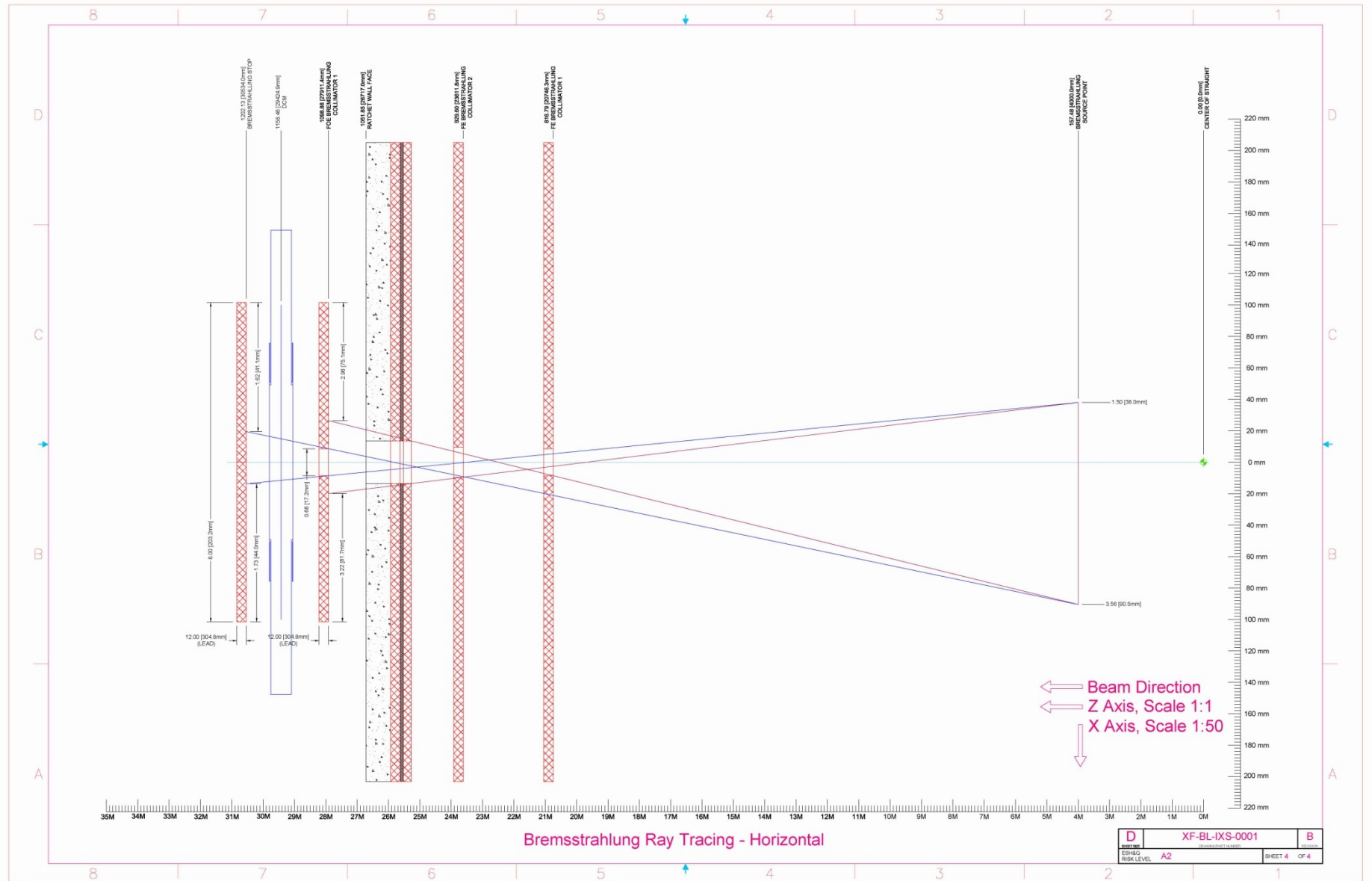


Figure A2-11: Beamline Vertical Bremsstrahlung Ray Tracings

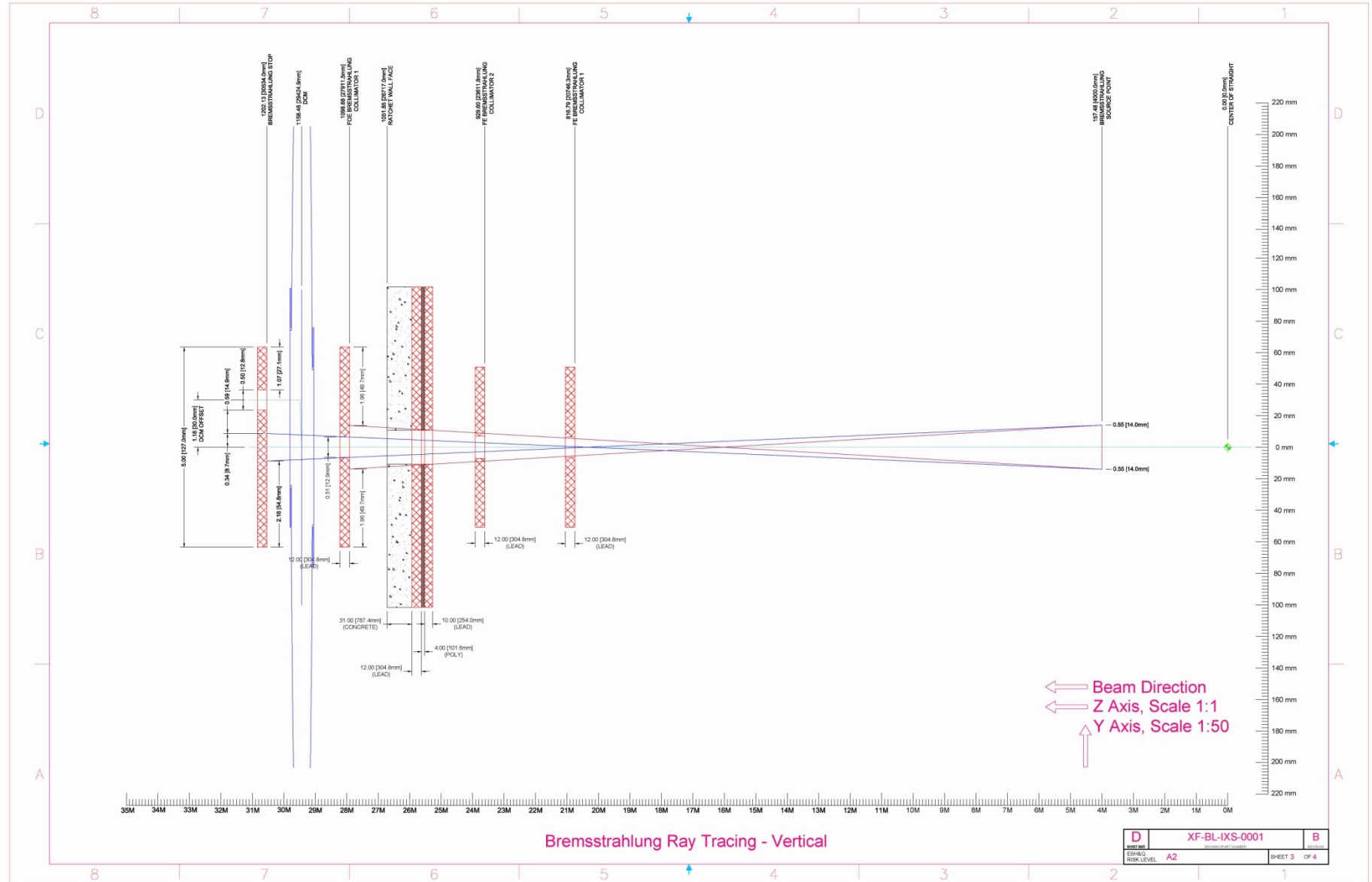


Figure A2-12: Shielding Enclosure Layout

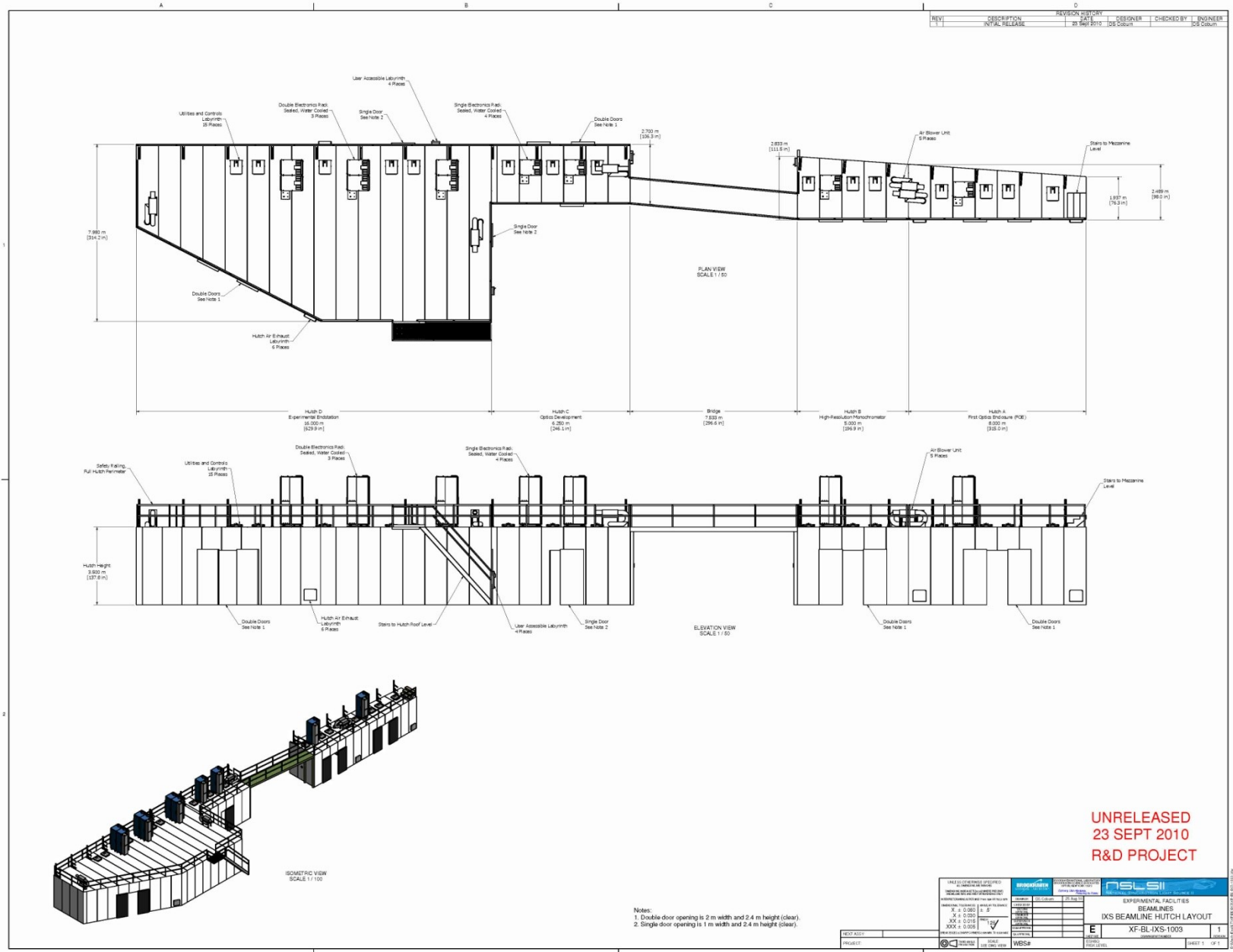


Figure A2-13: Utility Layout

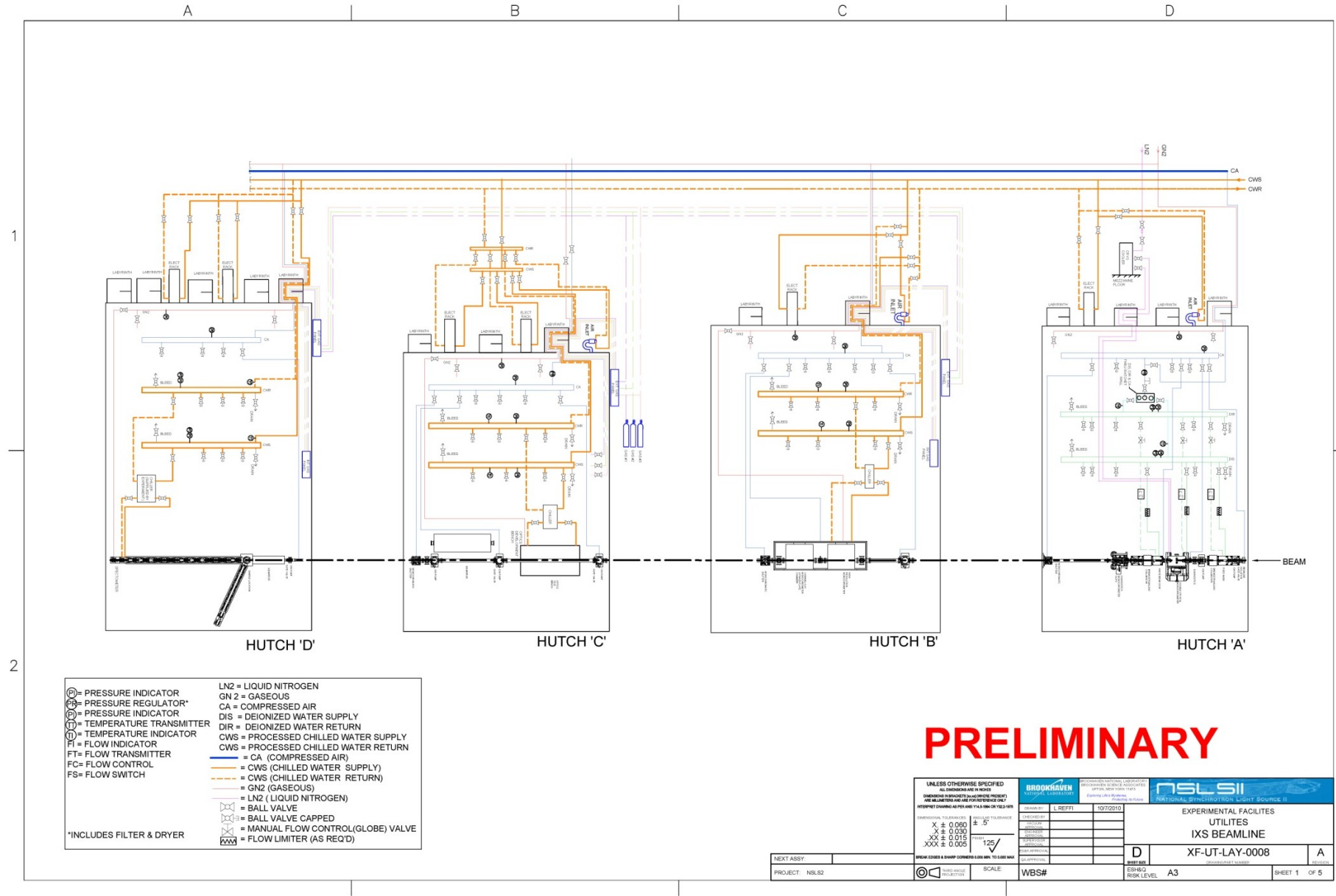


Figure A2-14: Personnel Safety System Schematic Layout

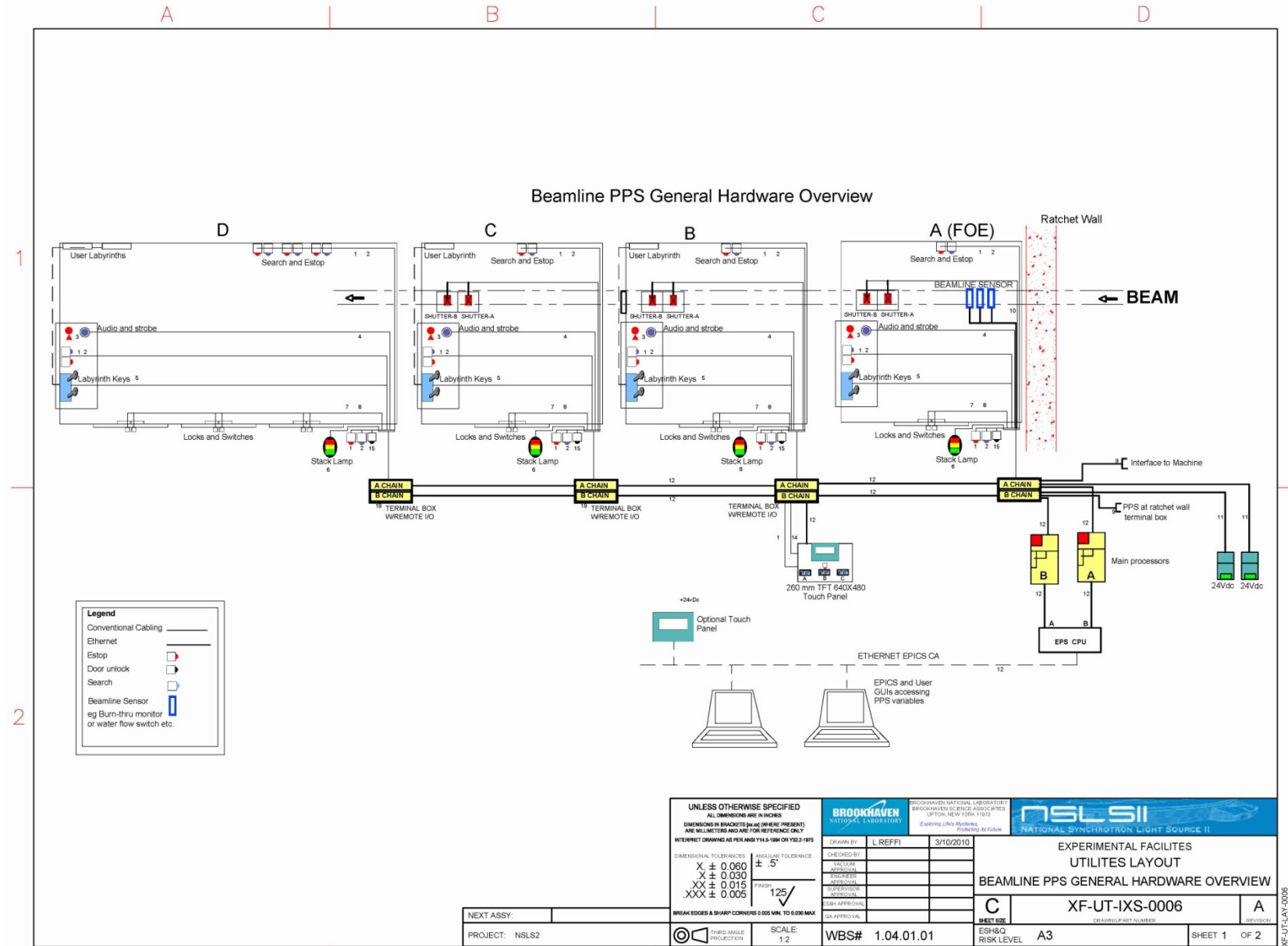
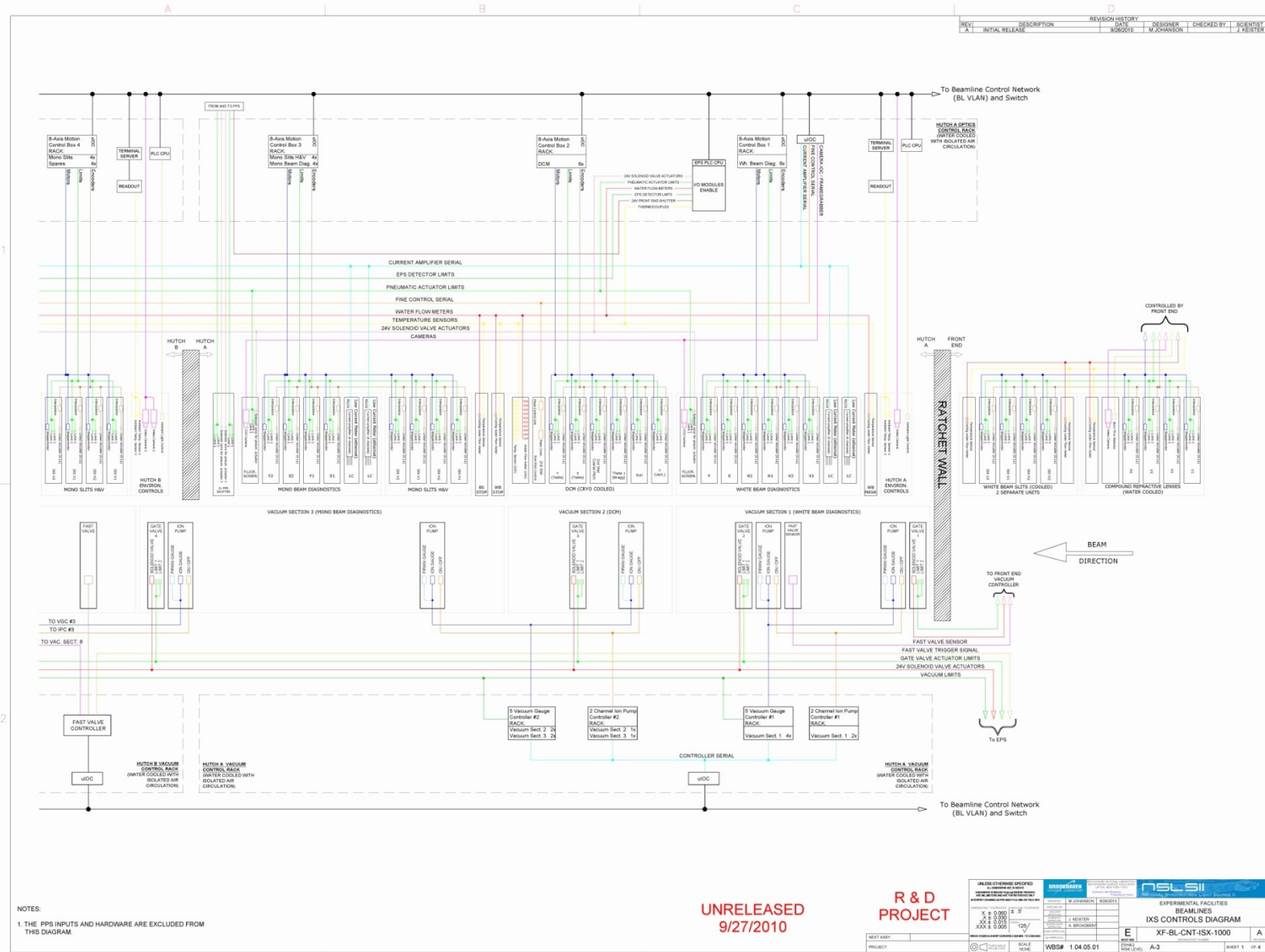
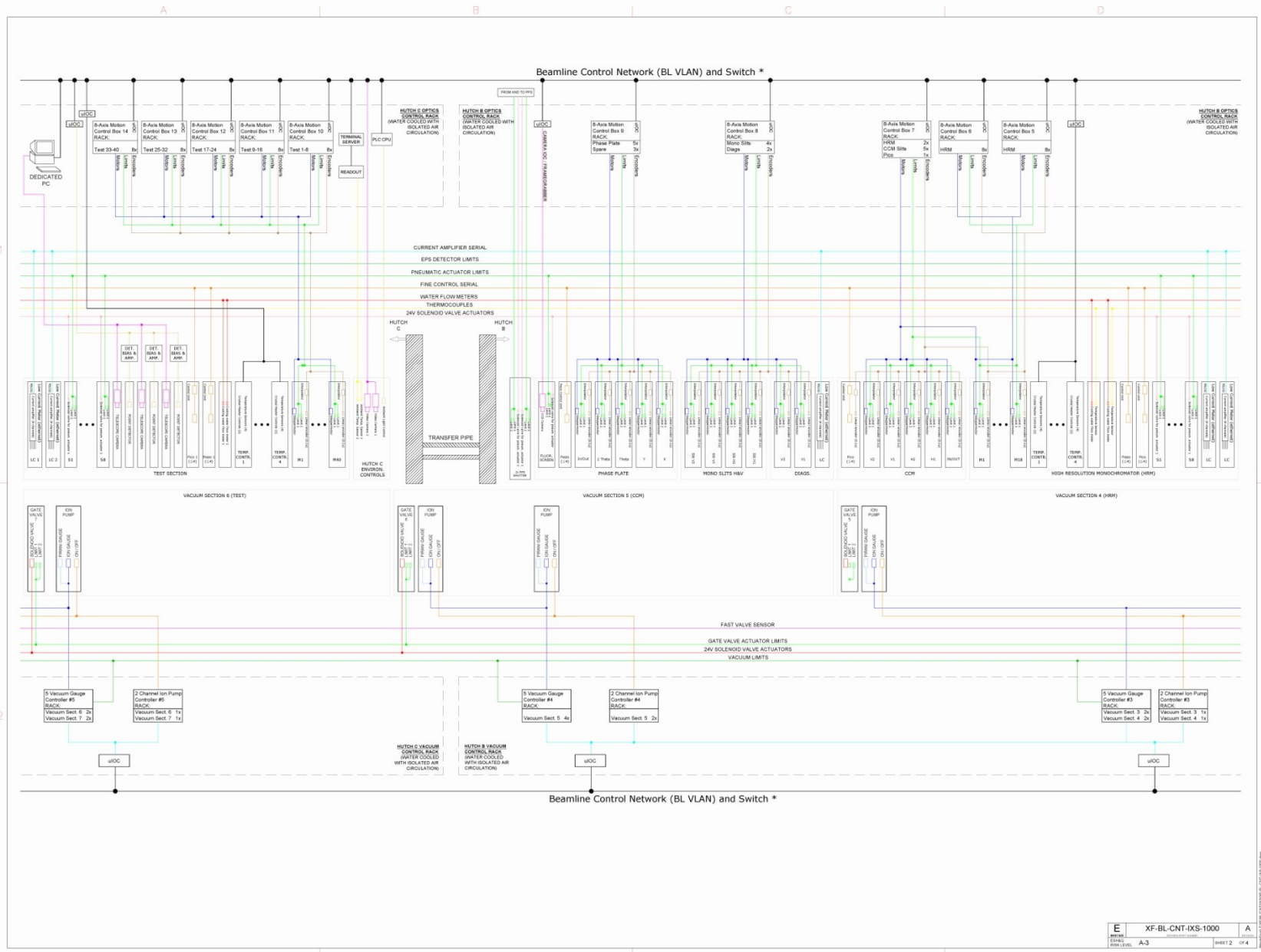
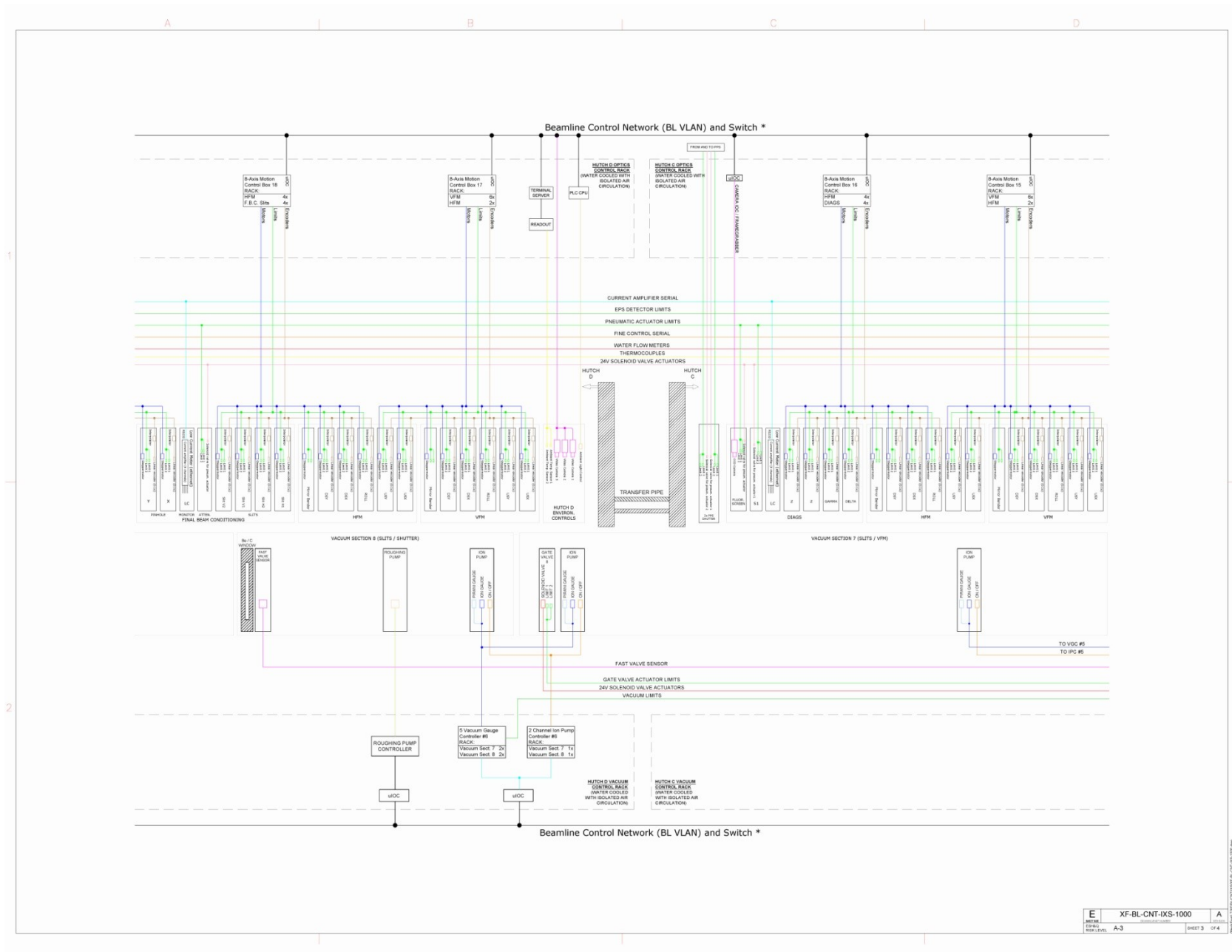


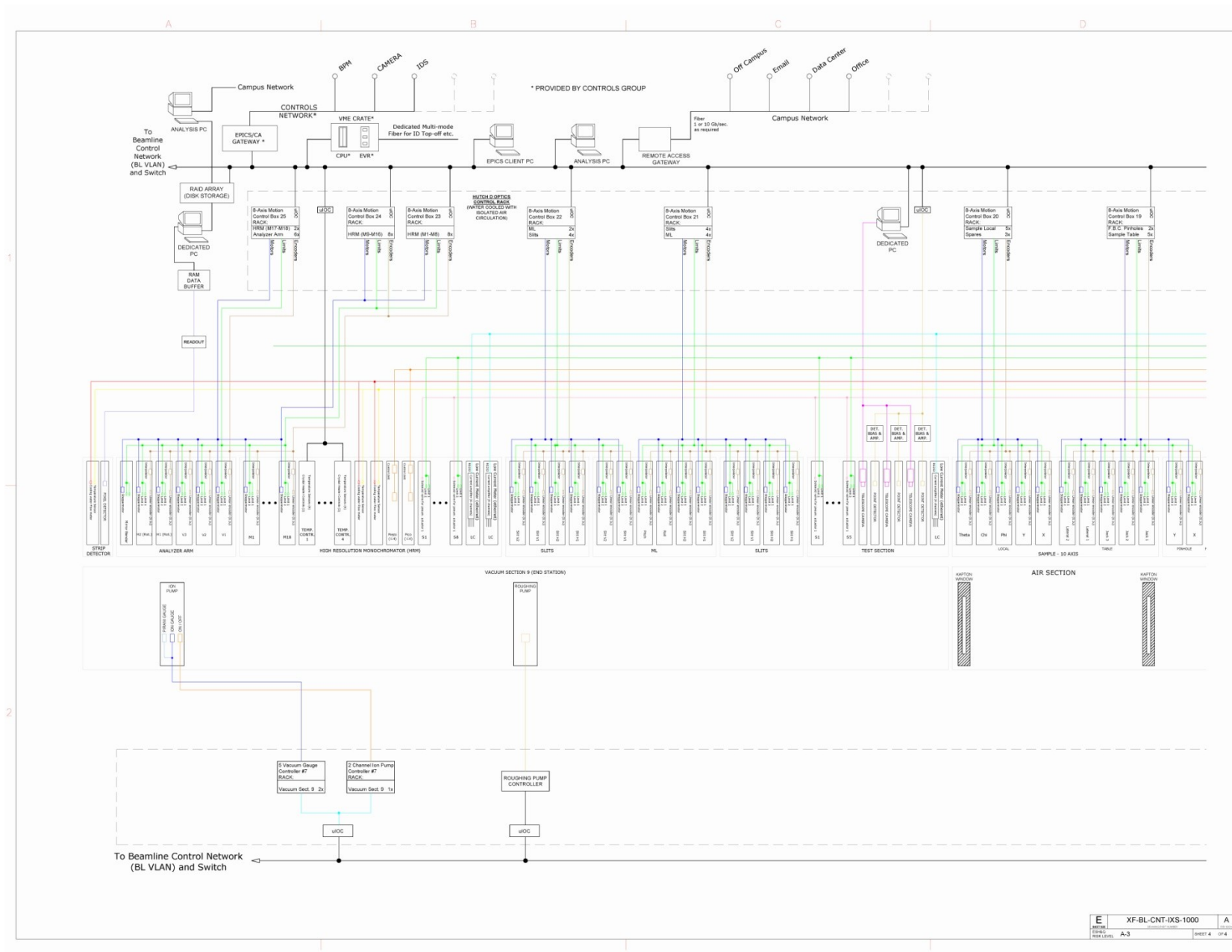
Figure A2-15: IXS Beamline Controls Layout





E	XF-BL-CNT-IXS-1000	A
REV:	A-3	SHEET 2 OF 4





E XF-BL-CNT-IXS-1000 A
 REV 1001
 DATE 10/10/08
 FILE LEVEL A-3 SHEET 4 OF 4

APPENDIX 3: LIST OF MAJOR COMPONENTS

The major beamline components, along with their distance from the source are listed in Table A3-1 through Table A3-4.

Table A3-1. Major components in Hutch A (FOE, starts at 26.7 m, and ends at Z = 34.7 m)

Description	Start Position (m)	Length (mm)	Notes
Beamline isolation valve	26.787	85	Vacuum isolation for beamline
Diagnostics Cross and Ion pump	26.987	295	Upstream end of Differential Pump
Fixed Mask	27.434	381	Protects Bremsstrahlung Collimator
Bremsstrahlung Collimator	27.816	395	Beamline safety component
Diagnostics Cross and Ion pump	28.325	270	Downstream end of Differential Pump
Diagnostics Cross	28.594	270	White beam diagnostics
Gate valve	28.865	70	Vacuum isolation for DCM
DCM	29.050	750	Beamline optics
Gate valve	29.913	70	Vacuum isolation for DCM
White Beam Stop	29.983	381	Beamline safety component
Bremsstrahlung Stop	30.364	395	Beamline safety component
Diagnostics Cross and Ion pump	30.912	270	Downstream end of Differential Pump
Quadrant BPM	31.321	35	Beamline diagnostic
Monochromatic Slits & Fluorescent Screen	31.356	550	Beamline diagnostic and aperture
Monochromatic Beam Shutter	34.285	245	Beamline safety component

Table A3-2. Major components in Hutch B (starts at 34.7 m, and ends at 39.7 m)

Description	Start Position (m)	Length (mm)	Notes
Diagnostics Cross and Ion Pump	34.894	254	Diagnostics and beam transport pumping
Gate valve	35.148	70	Vacuum isolation
Diagnostics Cross	36.230	270	Diagnostics
HRM (CDDW)	36.500	1000	High-resolution Monochromator
Gate valve	37.614	70	Vacuum isolation
Channel-Cut (CC) & Phase Plate (PP)	37.798	1000	Channel-Cut Monochromator
Diagnostics Cross	38.798	270	Diagnostics
Monochromatic Beam Shutter	39.240	245	BL Safety component

Table A3-3. Major components in Hutch C (starts at 47.24 m, and ends at 53.50 m)

Description	Start Position (m)	Length (mm)	Notes
Diagnostics Cross and Ion Pump	47.529	254	Diagnostics and beam transport pumping
Gate valve	47.783	70	Vacuum isolation
VFM-1 & HFM-1 (Mature scope)	47.853	2175	Beamline optics
Diagnostics Cross and Ion Pump	49.773	254	Diagnostics and beam transport pumping
Diagnostics Cross	50.027	254	Diagnostics
Gate valve with Be window	50.297	70	Vacuum isolation
Removable beam pipe	50.367	2140	Remove for optics testing
Optical Table	50.437	2000	For beamline optics development/testing.
Diagnostics Cross and Ion Pump	52.621	254	Diagnostics and beam transport pumping
Gate valve with Be window	52.875	70	Vacuum isolation

Table A3-4. Major components in Hutch D (starts at 53.5 m, and ends at 69.5 m)

Description	Start Position (m)	Length (mm)	Notes
Diagnostics Cross and Ion Pump	54.468	333	Diagnostics and beam transport pumping
Gate valve	54.801	70	Vacuum isolation
VFM-2 & HFM-2	55.085	2455	Beamline optics
Gate valve	57.540	70	Vacuum isolation
Be window	57.610	25	Beam exit port
Beam conditioning and monitor unit	57.635	365	Beam conditioning and clean-up
Sample motion stage	58.000	0	Spectrometer center
Sample entrance slit and Be window	58.145	25	Sample slit/pinhole with Be window
Multilayer collimating mirror x 2	58.170	150	Analyzer system
Spectrometer arm-1 (5 m)	58.320	4516	Spectrometer arm
Analyzer-1 (CDDW)	62.836	965	Crystal analyzer for 1 meV
Spectrometer arm-2 (10m)	58.170	9516	Spectrometer arm
Analyzer-2 (CDDW)	67.836	965	Crystal analyzer for 0.1 meV

APPENDIX 4: HUTCH SPECIFICATIONS

Enclosure designation		10-ID-A
Enclosure type		FOE, White Beam
Enclosure description		White Beam Optics enclosure
Shielding material		Lead
Dimensions (m)	Height max Width max Length max	3.5 2.5 8.0
Shielding	Side (lateral) panels Roof panels Downstream wall panels Additional downstream wall panel Guillotine Beam pipe penetration door (alignment window)	18 mm lead 6 mm lead 50 mm lead 50 mm lead (1×1 m) Downstream wall N/A
Entry 1	Position Size (m) Type Floor groove PSS Interfaces	Outboard side 2.4 H x 2.0 W Sliding double Yes Mounting plates for magnetic lock and dual position switches.
Hoist		Manual 1000 kg (double sliding rail)
Labyrinths	Positions to be as specified on drawing, to be sealed with anti-tamper screws except where locks or interlocks are specified. Fluids labyrinth (on roof) Electrical labyrinth (on roof) Air inlet labyrinth, with fan and filter (on roof) Air outlet labyrinth (at base of sidewall) User access labyrinth (on sidewall) Liquid nitrogen labyrinth (on roof)	1 1 1 2 0 (with interlock switches) 1
Other	Attachment points for adjacent enclosures	Downstream wall
Drawings	Number of full sized prints required of all drawings	3
Manuals	Number of copies required of all manuals	3

Enclosure designation		10-ID-B
Enclosure type		Experimental, Monochromatic
Enclosure description		High Resolution Monochromator Optics enclosure
Shielding material		Steel
Dimensions (m)	Height max Width max Length max	3.5 2.8 5.0
Shielding	Side (lateral) panels Roof panels Downstream wall panels Additional downstream wall panel Guillotine Beam pipe penetration door (alignment window)	6 mm steel 3 mm steel 6 mm steel N/A N/A 2 (upstream and downstream)
Entry 1	Position Size (m) Type Floor groove PSS Interfaces	Outboard side 2.4 H x 2.0 W Sliding double Yes Mounting plates for magnetic lock and dual position switches.
Hoist		Manual 1000 kg (double sliding rail)
Labyrinths	Positions to be as specified on drawing, to be sealed with anti-tamper screws except where locks or interlocks are specified. Fluids labyrinth (on roof) Electrical labyrinth (on roof) Air inlet labyrinth, with fan and filter (on roof) Air outlet labyrinth (at base of sidewall) User access labyrinth (on sidewall) Liquid nitrogen labyrinth (on roof)	1 1 1 2 1 (with interlock switches) 0
Other	Attachment points for adjacent enclosures	N/A
Drawings	Number of full sized prints required of all drawings	3
Manuals	Number of copies required of all manuals	3

Enclosure designation		10-ID-C
Enclosure type		Experimental, Monochromatic
Enclosure description		Secondary Optics enclosure
Shielding material		Steel
Dimensions (m)	Height max Width max Length max	3.5 2.7 6.25
Shielding	Side (lateral) panels Roof panels Downstream wall panels Additional downstream wall panel Guillotine Beam pipe penetration door (alignment window)	6 mm steel 3 mm steel 6 mm steel N/A N/A 2 (upstream and downstream)
Entry 1	Position Size (m) Type Floor groove PSS Interfaces	Outboard side 2.4 H x 2.0 W Sliding double Yes Mounting plates for magnetic lock and dual position switches.
Entry 2	Position Size (m) Type Floor groove PSS Interfaces	Inboard side 2.4 H x 1.0 W Sliding Single Yes Mounting plates for magnetic lock and dual position switches.
Hoist		Manual 1000 kg (double sliding rail)
Labyrinths	Positions to be as specified on drawing, to be sealed with anti-tamper screws except where locks or interlocks are specified. Fluids labyrinth (on roof) Electrical labyrinth (on roof) Air inlet labyrinth, with fan and filter (on roof) Air outlet labyrinth (at base of sidewall) User access labyrinth (on sidewall) Liquid nitrogen labyrinth (on roof)	1 1 1 2 1 (with interlock switches) 0
Other	Attachment points for adjacent enclosures	N/A
Drawings	Number of full sized prints required of all drawings	3
Manuals	Number of copies required of all manuals	3

Enclosure designation		10-ID-D
Enclosure type		Experimental, Monochromatic
Enclosure description		Endstation enclosure
Shielding material		Steel
Dimensions (m)	Height max Width max Length max	3.5 8.0 16.0
Shielding	Side (lateral) panels Roof panels Downstream wall panels Additional downstream wall panel Guillotine Beam pipe penetration door (alignment window)	6 mm steel 3 mm steel 6 mm steel N/A N/A 1 (upstream)
Entry 1	Position Size (m) Type Floor groove PSS Interfaces	Outboard side 2.4 H x 2.0 W Sliding double Yes Mounting plates for magnetic lock and dual position switches.
Entry 2	Position Size (m) Type Floor groove PSS Interfaces	Inboard side 2.4 H x 1.0 W Sliding Single Yes Mounting plates for magnetic lock and dual position switches.
Entry 3	Position Size (m) Type Floor groove PSS Interfaces	Upstream side 2.4 H x 1.0 W Sliding Single Yes Mounting plates for magnetic lock and dual position switches.
Hoist		Manual 1000 kg (double sliding rail)
Labyrinths	Positions to be as specified on drawing, to be sealed with anti-tamper screws except where locks or interlocks are specified. Fluids labyrinth (on roof) Electrical labyrinth (on roof) Air inlet labyrinth, with fan and filter (on roof) Air outlet labyrinth (at base of sidewall) User access labyrinth (on sidewall) Liquid nitrogen labyrinth (on roof)	1 3 2 4 2 (with interlock switches) 0
Other	Attachment points for adjacent enclosures	N/A
Drawings	Number of full sized prints required of all drawings	3
Manuals	Number of copies required of all manuals	3

APPENDIX 5: ADDITIONAL PERFORMANCE EVALUATIONS OF BE CRL

A4.1 Effects of Misalignments

If we assume the aperture of the parabolic lens is simply equal to $2R^{33}$, an analytic expression for the transmission from a single lens can be obtained (see Ref. [14]):

$$T(x_0) = \frac{\exp\left(\frac{-Rd}{2\Sigma^2}\right)}{\sqrt{1+(\sigma/\Sigma)^2}} \times \frac{1}{2} \left[\operatorname{erf}\left(\frac{R-y_0}{\sigma} \sqrt{\frac{1+(\sigma/\Sigma)^2}{2}}\right) + \operatorname{erf}\left(\frac{R+y_0}{\sigma} \sqrt{\frac{1+(\sigma/\Sigma)^2}{2}}\right) \right] \quad (\text{A-1})$$

where $\operatorname{erf}(x) = \frac{2}{\sqrt{\pi}} \int_0^x \exp(-y^2) dy$ is the so-called error function, y_0 the distance between the axis of incident beam

and that of the CRL, d the apex thickness, σ the RMS incident beam size, and Σ is the RMS aperture of the lens and is given by:

$$\Sigma^2 = \delta_l F = \frac{\delta}{4\pi\beta + \lambda/l_s} \lambda F, \quad (\text{A-2})$$

where l_s , β and λ are the total attenuation length (absorption + scattering), the absorption coefficient and the wavelength of incident beam. In Figure A4-1 we report the calculated transmission of the Be CRL as evaluated using Equation (A-1) with $N = 4$, $R = 0.3$ mm and $d = 0.1$ mm for an incident beam with $\sigma = 0.146$ mm (or 0.345 mm FWHM) at 9.13 keV. The maximum transmission with zero beam offset is $\sim 85\%$.

In order to estimate the effect of relative misalignment between the lens axes, we start by evaluating the overall phase distortion that such misalignment provides to the transmitted wave. For this purpose, we introduce an average CRL axis defined as the average position of the various axes of the lenses in the compound (see Figure A4-2). If d_i is the offset of the i -th lens axis with respect to the average position, we can write the equation of the parabolic lens surface as:

$$x = d + \frac{(y - d_i)^2}{2NF\delta} \quad (\text{A-3})$$

The phase shift introduced by the relative misalignment of the i -th lens axis can be then easily written as:

$$-i\Phi = \left(iq\delta - \frac{1}{3l_i} \right) \sum_{i=1}^N \left[d + \frac{(y - d_i)^2}{2NF\delta} \right], \quad (\text{A-4})$$

where q is the momentum transfer at the lens interface, given by the modulus of the difference between incident and transmitted beam wavevectors. Developing the squared term and taking into account that $\sum_{i=1}^N d_i = 0$, we can

introduce the variance of the d_i -distribution: $\sigma_A^2 = \frac{1}{N} \sum_{i=1}^N d_i^2$. One can immediately see that the phase distortion induced by the misalignment is basically a constant $q\sigma_A^2/2F$. A constant phase shift doesn't change the focal properties of the system; however it yields an intensity attenuation which is basically equivalent to an increase of the base thickness to $d + \sigma_A^2/2F\delta$ which obviously introduces more absorption. The transmission as a function of σ_A is presented in Figure A4-3.

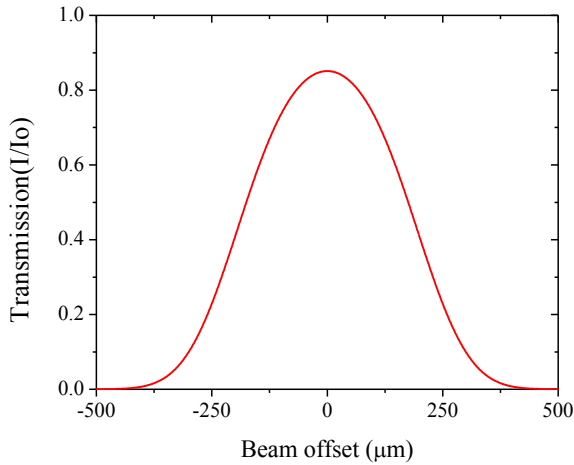


Figure A4-1. The transmission profile obtained for $N = 4$, $R = 0.3$ mm, $F = 9.2$ m as a function of the offset between the beam and the CRL optical axis.

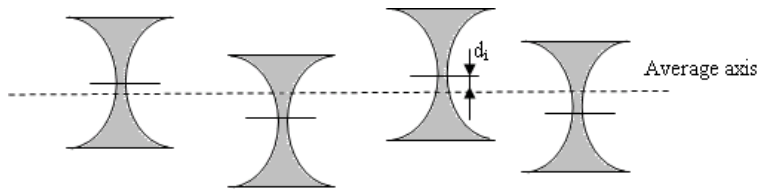


Figure A4-2. Schematic representation of the misalignment of the CRL lenses.

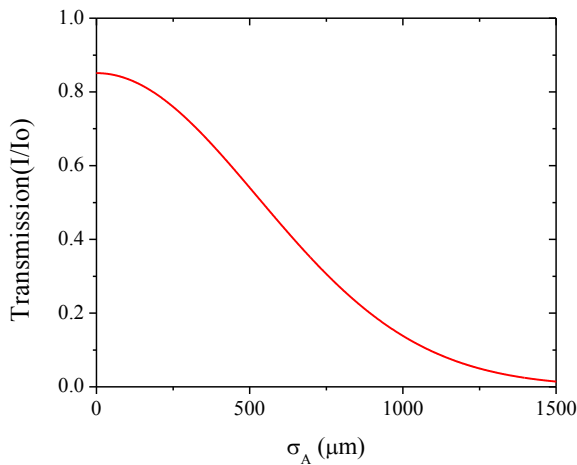


Figure A4-3. The transmission profile obtained for $N = 4$, $R = 0.3$ mm, $F = 9.2$ m as a function of the standard deviation of the variance of the distribution defining the mutual offset between the lens axes.

A4.2 Effects of Imperfections

The calculations presented in Figures A4-1 and A4-3 did not consider loss due to the roughness and the figure error of the lens surface. In the Rayleigh model of roughness, the lens surface is described assuming that the optical path of the beam through the lenses oscillates around the value determined by the perfect parabolic surface. Equivalently we can assume that the lens surface is a stochastic variable following a Gaussian distribution centered around the perfect parabolic profile. An explicit derivation of the contribution of roughness to the transmission is performed averaging over such Gaussian distribution, which leads to:

$$T_{rough} = \exp\left(-\frac{Nq_0^2\sigma_r^2}{2}\right)\exp\left(-\frac{Nq_0^2\sigma_r^2 y^2}{2R^2}\right), \quad (\text{A-5})$$

where $q_0 = 2\pi\delta / \lambda$, and σ_r is the variance of the Gaussian distribution, i.e. the RMS roughness of the surface. One may notice that this factor depends on the transverse coordinate "y". In order to evaluate the contribution of the transmission we have to consider a Gaussian beam transverse profile and integrate over the coordinate. The result is presented in Figure A4-4.

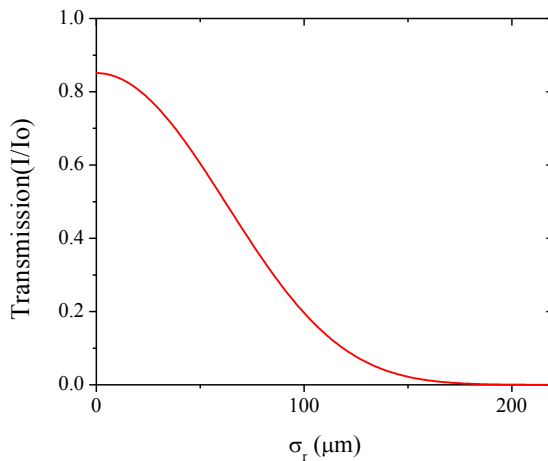


Figure A4-4. The transmission profile obtained for $N = 4$, $R = 0.3$ mm, $F = 9.2$ m as a function of the lens roughness.

As can be seen from Figures A4-1, A4-3 and A4-4, the contributions due to misalignments and surface roughness of the lenses do not dramatically affect the transmission as long as the respective deviations from the perfect configuration are of the order of 10 μm or less.

Effects of internal defects on the performance of the Be CRL have also been studied using partially-coherent wavefront propagation. These defects are simulated by the presence of air bubbles in the materials in certain density and various randomly varied sizes ranging from 1 to 20 μm. Two densities of 400 and 2000 bubbles/mm³ have been considered and the results are presented in Figure A4-5. As expected, these defects lead to the loss of transmission and contribute to the tails of the beam profile, and should be avoided as much as possible.

Finally, optical aberrations due to thermal deformation (thickness increase) of the Be CRL under heatload conditions for the FEA analysis have been investigated. For Be, the optical path variation due to thermal deformation is given by $\delta \cdot \Delta s < 10^{-2} \cdot \lambda$, which is the order of a few thousandth Angstrom. The results are presented in Figure A4-6. Based on these results, optical aberration due to thermal deformation of the Be CRL is expected to be small.

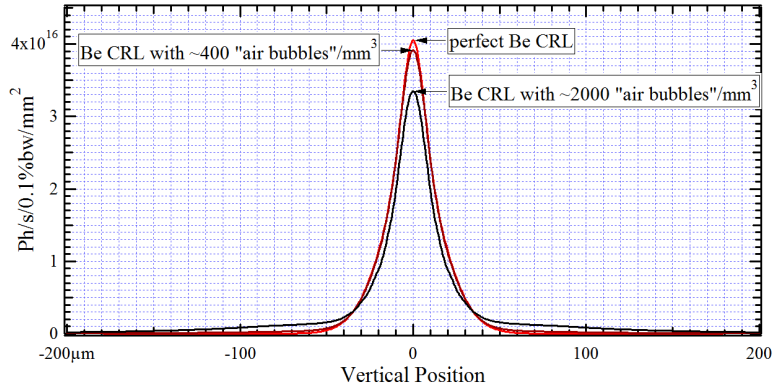


Figure A4-5. The simulated intensity profile as obtained with a CRL with an increasing density of air bubbles.

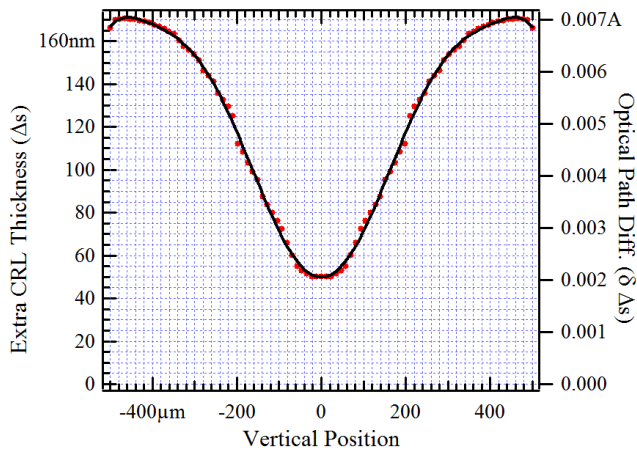


Figure A4-6. Optical path variation as a result of thermal deformation of the Be CRL.

REFERENCES

- [1] Yong Cai, *Conceptual Design Report for the Inelastic X-ray Scattering Beamline at NSLS-II*, Final Draft, September 2009 (http://www.bnl.gov/nsls2/docs/PDF/cdr/4_IXS%20CDRfinal_10_10%20BAT.pdf, LT-XFD_CDR_IXS-00123).
- [2] Yu. V. Shvyd'ko. *Advanced Designs of Angular Dispersive X-ray Monochromators*, to be published. See also *Conceptual Design Report for NSLS-II* (<http://www.bnl.gov/nsls2/project/CDR>) Section 11.5.2: *Conceptual Design for the Inelastic X-Ray Scattering Beamline*.
- [3] Yu. V. Shvyd'ko, *X-Ray Optics, High-Energy-Resolution Applications* (Springer, Berlin, 2004)
- [4] Yu. V. Shvyd'ko et al, AIP Conf. Proceedings Series, CP 879 (2006)
- [5] Jeff Keister, Yuriy Stetsko, Marcelo Honnicke, Xianrong Huang, Nalaka Kodituwakku, Scott Coburn, and Yong Cai, (*in preparation*).
- [6] T.S. Toellner et al, NIM A557, 670 (2006); and NSLS-II presentation
- [7] T. Tanabe, private communication. See also *Conceptual Design Report for NSLS-II* (<http://www.bnl.gov/nsls2/project/CDR>) Section 12.7: *Insertion Devices*.
- [8] O. Chubar, J. Bengtsson, A. Broadbent, Y.Q. Cai, Q. Shen, and T. Tanabe, AIP Conference Proceedings for SRI2009.
- [9] See, for example, G. Monaco, C.R. Physique **9**, 608 (2008).
- [10] O. Chubar, private communication.
- [11] L. Doom, B. Gash, S. Sharma et al, see <http://groups.nsls2.bnl.gov/acceleratorsystems/mech/frontends/default.aspx>.
- [12] P.K. Job and W.R. Casey, *Guidelines for NSLS-II Beamlines and Front End Radiation Shielding Design*, Document #LT-ESHDES-08-003-rev001.
- [13] A. Snigirev, V. Kohn, I. Snigireva, A. Souvorov, and B. Lengeler, *App. Optics*, **37**, 653 (1998).
- [14] P. Elleaume, *Nucl. Instrum. & Methods A*, **412**, 483 (1998).
- [15] For a Gaussian beam, an aperture size of $(4\sigma) 6\sigma$ corresponds to (95.4%) 99.7% of the beam. With a vertical beam size of 0.345mm FWHM, $6\sigma = 6*0.345/2.355 = 0.879$ mm, which is still within the RMS acceptance of the Be CRL.
- [16] O. Chubar, unpublished.
- [17] Prof. Dr. B. Lengeler, RWTH Aachen, email: lengeler@physik.rwth-aachen.de; web: www.physik.rwth-aachen.de/en/institutes/institute-iib/group-lengeler.
- [18] L. Zhang, private communication.
- [19] V. Ravindranath and O. Chubar, unpublished (include web link to SharePoint).
- [20] J. Savino, Q. Shen, G. Strieter, E. Fontes, AK. Pauling, AIP Conf. Proc. 8th Conf. on SRI, 506-509 (2004).
- [21] Kohzu Precision Co. Ltd. <http://www.kohzu.com/>.
- [22] X.R. Huang, unpublished.
- [23] Yu. V. Shvyd'ko, *Advanced in X-ray Optics for IXS Spectroscopies*, Workshop on Inelastic X-ray Scattering at NSLS-II, February 7-8, 2008, http://www.bnl.gov/nsls2/workshops/docs/IXS/IXS_15_Shvydko.pdf.
- [24] T. Ishikawa *et al.*, Rev. Sci. Instrum. **63**, 1015 (2004)
- [25] M. Yabashi, K. Tamasaku, S. Kikuta, and T. Ishikawa, Rev. Sci. Instr. **72**, 4080 (2001)
- [26] T.S. Toellner et al, Nucl. Instr. Method A **557**, 670 (2006); and NSLS-II Presentation, Oct. 9, 2009.
- [27] ACCEL Instruments GmbH, Gladbach. Email: accel@accel.de.
- [28] M.G. Honnicke, X. Huang, J.W. Keister, C.N. Kodituwakku and Y.Q. Cai, J. Synchrotron Rad. **17**, (2010).
- [29] R. Dietsch and T. Holz, United States Patent 7298822 – X-ray optical element
- [30] F. Hertlein *et al.*, Part. Part. Syst. Character. **22**, 378 (2005)
- [31] U. Shymanovich *et al.*, Appl. Phys. B **92**, 493 (2008)
- [32] INCOATEC – innovative coating technologies GmbH. <http://www.incoatec.de>.
- [33] We are currently evaluating the transmission for a more realistic $1 \times 1 \text{ mm}^2$ CRL aperture, we obviously expect to observe an increase in the estimated transmission.